Robust Design and Tolerancing of Compressor Blades

by

Eric Alexander Dow
B.S., Massachusetts Institute of Technology (2009)
M.S., Massachusetts Institute of Technology (2011)

Submitted to the Department of Aeronautics and Astronautics
in partial fulfillment of the requirements for the degree of
Doctor of Philosophy
at the
MASSACHUSETTS INSTITUTE OF TECHNOLOGY
February 2015

Signature redacted

Author .....
Department of Aeronautics and Astronautics
October 17, 2014

Signature redacted

Certified by .....
Qiqi Wang
Assistant Professor of Aeronautics and Astronautics
Thesis Supervisor

Signature redacted

Certified by .....
David Darmofal
Professor of Aeronautics and Astronautics
Committee Member

Signature redacted

Certified by .....
Edward Greitzer
H. N. Slater Professor of Aeronautics and Astronautics
Committee Member

Signature redacted

Accepted by .....
Paulo Lozano
Chair, Department Committee on Graduate Students

Robust Design and Tolerancing of Compressor Blades

by

Eric Alexander Dow

Submitted to the Department of Aeronautics and Astronautics
on October 17, 2014, in partial fulfillment of the
requirements for the degree of
Doctor of Philosophy

Abstract

Variations in the geometry of compressor blades can be introduced by variability in the manufacturing process or by in-service erosion. Recent research efforts have focused on characterizing the impacts of this geometric variability on turbomachinery performance and designing blade geometries whose performance is robust to this variability. Relatively little work has been done to specify the appropriate level of variability by designing the manufacturing tolerances. This thesis presents new approaches for optimizing tolerances that can be applied to compliment existing geometry optimization techniques.

Building upon previous research, a Gaussian random field model of manufacturing variability is developed and used to estimate the statistical performance impacts of geometric variability on compressor blade performance. Flow mechanisms that deteriorate the mean performance in the presence of geometric variability are analyzed for design and off-design conditions. A probabilistic, gradient-based optimization framework is presented and applied to optimize the tolerances of compressor blades, as well as to optimize the tolerances and blade geometry simultaneously.

The effectiveness of simultaneous optimization of the geometry and manufacturing tolerances is compared to a sequential procedure where the nominal blade geometry is optimized first, followed by the tolerances. Single-point optimization, where the performance at a single flow incidence is optimized, is found to produce geometries that are not robust to manufacturing variations. Adopting a multi-point design strategy results in blades that are robust to both variations in the geometry and incidence, allowing a sequential design strategy to be used.

Thesis Supervisor: Qiqi Wang
Title: Assistant Professor of Aeronautics and Astronautics

Committee Member: David Darmofal
Title: Professor of Aeronautics and Astronautics

Committee Member: Edward Greitzer
Title: H. N. Slater Professor of Aeronautics and Astronautics

Acknowledgments

I would like to thank my advisor, Professor Qiqi Wang, for five great years of collaboration, support and guidance. Professor Wang has been an invaluable sounding board for research ideas, providing deeper insight and suggestions on how they might be improved.

I extend my gratitude to my committee members Professor David Darmofal and Professor Edward Greitzer. Their advice and suggestions were immensely helpful in shaping this thesis. I also appreciate the comments and suggestions from my thesis readers, Professor Rob Miller and Professor Karen Willcox. I would also like to thank Professor Mark Drela for developing the MISES code used extensively in this thesis, and for answering many questions about its usage.

I would like to thank Pratt & Whitney both for funding the first year of my Ph.D., and for the many fruitful discussions about the research. I also gratefully acknowledge the financial support provided by the Boeing Fellowship, which allowed me to continue my research through the last year of my graduate studies.

I couldn't have asked for a better group of coworkers in both ACDL and GTL. Thanks for the friendship, advice, and intellectual stimulation.

Finally, I would like to thank my family for all of their support during my nine years at MIT. To my parents, Bob and Martha, and sister, Laura, thank you for providing perspective and encouragement during my journey through MIT.

Contents

List of Figures

List of Tables

Chapter 1

Introduction

1.1 Motivation

Engineering systems are often optimized using a deterministic approach where the optimal design describes the system's geometry, material properties and operating conditions in the absence of variability. We refer to this as the nominal design. When the system is produced and operated in the real world, deviations from the nominal design may occur due to noise in the manufacturing process, variations in material properties, variations in the operating environment, or due to component wear. These deviations are often undesirable because they can adversely affect the actual system performance. For example, deviations from the nominal design can degrade the mean performance of the system or result in an increased probability of system failure. It may be possible to reduce the impact of these variations by changing the nominal design of the system. This idea has motivated the use of robust design methodologies, where the design is selected according to its performance in the presence of variability.

Alternatively, the detrimental effects of variability can be reduced by imposing tolerances. For example, manufacturing variability may be reduced by specifying stricter tolerances on the geometry. Variability in material properties can be reduced by using materials with less part-to-part variation. Such reductions in variability, however, are typically associated with increased cost. The cost associated with reducing variability

competes with the benefits of improving performance, implying an optimal balance between the level of variability and the performance of the system.

The motivating applications for this thesis are turbomachinery compressor blades. The manufacturing processes used to create compressor blades and in-service erosion introduce geometric variability resulting in manufactured blade geometries that deviate from the nominal, or design intent, geometry. A representative deviation between the design intent geometry and a set of manufactured blades is illustrated in Figure 1-1. Introducing geometric variability tends to negatively impact the mean performance of compressor blades, leading to increased costs over the life of the compressor blade. For example, Garzon estimated that manufacturing variations decrease the mean polytropic efficiency of a six stage axial compressor by 1% [27].

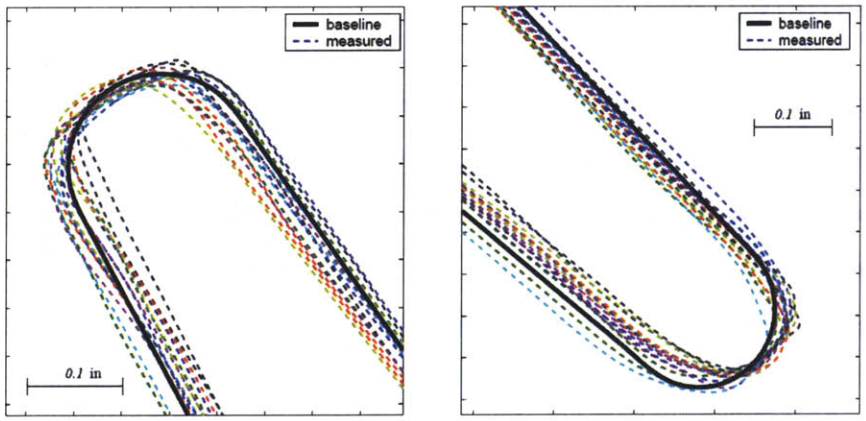

Figure 1-1: Illustration of manufacturing variability observed in leading and trailing edges of measured compressor blades (from [27]). The nominal design is represented by the solid line, and the measured blades by dashed lines.

Tolerancing is not the only way to reduce the impact of geometric variations on compressor performance. Blade wear can be reduced by using erosion resistant coatings [14]. A recent survey of high pressure compressor blades found that over the first 4,000 cycles of operation, the magnitude of geometric variations introduced by the manufacturing process are more significant than those introduced by erosion [32]. This thesis therefore focuses on mitigating the detrimental impacts of geometric variations introduced by the manufacturing process as opposed to those introduced by

erosion.

1.2 Literature Review

This section presents an overview of relevant research, with a focus on work related to robust design and tolerancing of turbomachinery components. Previous investigations of methods for modeling variability and its performance impacts are discussed and robust design methodology and tolerance optimization are reviewed.

1.2.1 Modeling Geometric Variability

Determining the effects of manufacturing variability on compressor blade performance requires a model of the geometric variability introduced by the manufacturing process. One approach is to describe the geometric variability using a parametric approach [36, 41, 46, 51]. In the parametric approach a set of geometric parameters, such as stagger angle, chord length, leading edge thickness, and maximum camber are measured for a collection of manufactured blades. A probability distribution for each geometric parameter is constructed using the measurement data. The advantage of the parameter based approach is that the geometric variability is described in terms of design parameters. However, there is no guarantee that the set of parameters selected to describe geometric variability are sufficient for describing all relevant geometric variations. Geometric parameters that have an impact on the performance of the blade may be omitted.

High fidelity probabilistic models of geometric variability have been developed using principal component analysis (PCA) [27, 35, 48, 71, 75]. The covariance matrix of surface deviations is constructed using measurement data of manufactured blades, and a reduced order model of compressor blade manufacturing variability is formed

from the principal components of the covariance matrix:

$$\tilde{\mathbf{x}} = \mathbf{x}_0 + \bar{\mathbf{x}} + \sum_{i=1}^{K} \sqrt{\lambda_i}\mathbf{v}_i\xi_i, \tag{1.1}$$

where $\mathbf{x}_0$ represents the design intent blade coordinates, $\bar{\mathbf{x}}$ represents the mean deviation of the measured blades, λ_i and $\mathbf{v}_i$ are the eigenvalues and eigenvectors (or modes) of the covariance matrix of measured blade coordinates, and ξ_i are uncorrelated random variables with unit variance. The joint distribution of $\boldsymbol{\xi} = \{\xi_i\}_{i=1}^{K}$ can be estimated from measurement data. Some studies have found that the ξ_i are distributed as independent, identically distributed (i.i.d.) Gaussian random variables with zero mean and unit variance, i.e. $\boldsymbol{\xi} \sim \mathcal{N}(0, \mathbf{I})$ [3, 20, 27, 71]. Other studies have found that the distribution of $\boldsymbol{\xi}$ deviates substantially from an i.i.d. Gaussian distribution. Lamb discovered a PCA mode that was bimodally distributed, and two pairs of modes with dependent distributions [47]. Lange et al. found several modes that were not normally distributed [48]. Although the distributions of some PCA modes have been found to deviate from i.i.d. Gaussians, this deviation does not invalidate the PCA model. Equation (1.1) can still be used to generate sample geometries regardless of the distribution of $\boldsymbol{\xi}$.

The dominant PCA modes constructed in [27] using a set of measurement data for an integrally bladed rotor (IBR) are shown in Figure 1-2. The first mode represents solid body translation and the second mode represents thickening of the blade. The ensemble of realizations produced by this model has the same mean and variance as the set of measured blades [43]. When $\boldsymbol{\xi} \sim \mathcal{N}(0, \mathbf{I})$, the PCA model given in Equation (1.1) is an example of a Gaussian random field, where the mean and covariance are constructed empirically. A related approach is to specify the mean and covariance functions of the Gaussian random field analytically. Schillings et al. and Chen et al. have modeled geometric uncertainty in airfoil geometries using this approach [7, 12, 69]. Random fields have also been used to model geometric variability by the mechanical design community [57, 79]. By modeling variations for the entire geometry, random

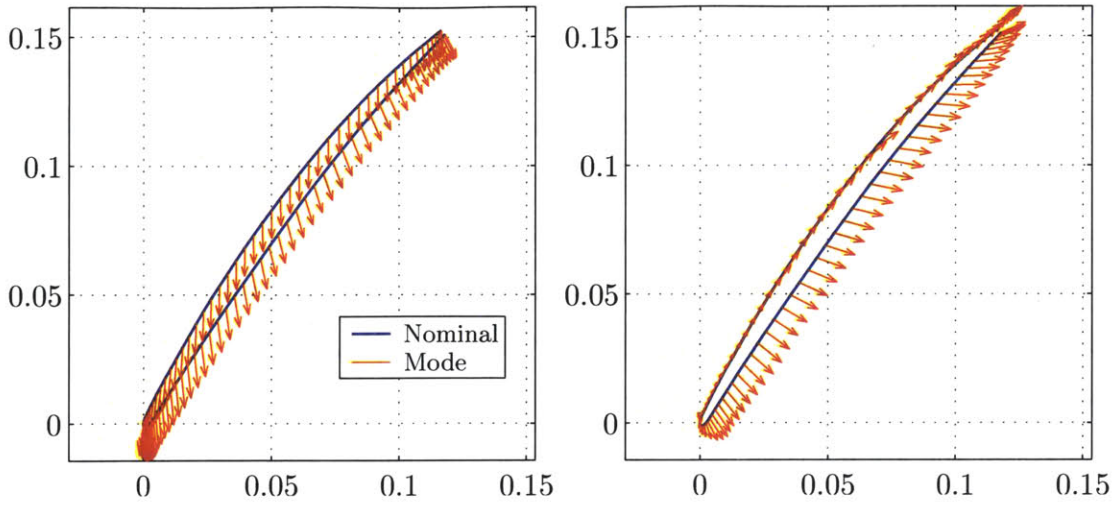

(a) Mode 1 (b) Mode 2

Figure 1-2: First two PCA modes computed from IBR measurement data (from [27]).

field models of geometric variability avoid the limitations imposed by the parametric approach and are therefore used in this thesis.

1.2.2 Performance Impacts of Geometric Variability

The detrimental effects of compressor blade geometric variability have been demonstrated both experimentally and through numerical simulations. Experiments performed by Reid et al. showed a decrease in adiabatic efficiency when the leading edges of transonic rotor blades are made blunter as a result of geometric variations [64]. Suder et al. experimentally investigated the effects of surface roughness and thickness variations on transonic compressor stage performance [73]. They observed up to a 6% reduction in the adiabatic efficiency at the design pressure ratio and attributed most of the reduction in efficiency to increased roughness and thickness near the leading edge of the blade.

Numerical simulation can also be used to assess the performance of many different geometric variations. To simulate the effect of geometric variability on compressor performance, a model of geometric variability is constructed using one of the techniques described previously, an ensemble of blade geometries is generated using this model,

and the performance quantities of interest are computed for each sample within the ensemble. The ensemble can be used to estimate the distribution or statistics, e.g. the mean or variance, of the performance quantities of interest. Geometric variability is propagated to the engineering quantities of interest using either the Monte Carlo method [27, 49] or the polynomial chaos method [55, 76].

Simulations have shown that manufacturing variations increase compressor performance variability and degrade mean performance. Lange et al. found that the isentropic efficiency is negatively correlated with compressor blade thickness, especially near the leading edge [49]. Variability in the leading edge thickness therefore leads to variability in the efficiency. Garzon demonstrated that the mean total pressure loss coefficient of a flank-milled IBR was increased by 23% due to manufacturing variability [28]. The histogram in Figure 1-3 illustrates both the loss variability and mean shift in loss coefficient resulting from geometric variability for the IBR considered by Garzon.

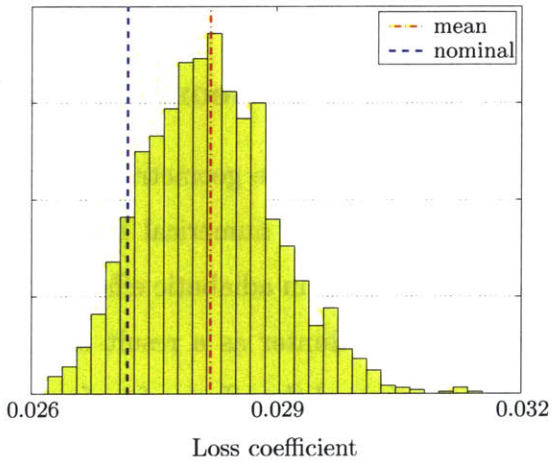

Figure 1-3: Mean shift in loss coefficient due to geometric variability (from [27]).

Goodhand et al. quantified the impact of leading edge manufacturing variations on compressor blade incidence range, defined as the difference between the positive and negative flow angles for which the loss is equal to a specified value [32]. When the leading edge radius of curvature of the nominal blade is reduced, introducing manufacturing variations reduces the mean incidence range. Flow separation occurs on

some manufactured blades at positive incidence, reducing the mean positive incidence range. They point out that nonlinear mechanisms, such as leading edge separation, are responsible for changing the mean loss. If the loss $\bar{\omega}$ is a linear function of the geometry $\mathbf{x}$, i.e. $\bar{\omega}(\mathbf{x}) = \mathbf{c}^\intercal \mathbf{x}$, and the manufacturing variations have mean zero, then $\mathbb{E}[\bar{\omega}(\mathbf{x})] = \mathbf{c}^\intercal \mathbb{E}[\mathbf{x}] = \mathbf{c}^\intercal \mathbf{x} = \bar{\omega}(\mathbf{x})$, and no mean shift occurs. We therefore conclude that a mean shift in loss can only occur when the loss is a nonlinear function of the geometry.

1.2.3 Robust Design Optimization

For systems whose performance is sensitive to variability, introducing variability can degrade the statistical performance of the deterministic optimal design. Lack of robustness has been demonstrated in deterministically optimized compressor blades: introducing geometric variability to deterministically optimized blades was found to increase the mean loss by as much as 20% [27]. Goodhand et al. found that deterministic design optimization produces a suboptimal design when a "switch" in the flow mechanism that limits performance occurs on some manufactured blades [33]. They provide a concrete example by reducing the suction surface curvature near the leading edge of a rotor blade. When geometric variations are introduced to the nominal geometry, flow separation occurs at positive incidence for many of the blades, reducing the mean incidence range.

Robust optimization finds designs whose statistical performance remains unchanged when the state of the system is perturbed as a result of variability [5]. Common measures of robustness used in robust design include the mean and variance of performance quantities of interest. The probability of a quantity of interest exceeding a critical value, or failure probability, may also be of interest. Robust design optimization principles have been applied to design airfoils under uncertain operating conditions. Huyse et al. consider minimizing the mean drag coefficient of a transonic airfoil subject to uncertainty in the Mach number with a fixed lift coefficient [39]. The resulting design produced lower drag than a single-point design at almost all input Mach numbers.

By adding a term proportional to the variance of the drag to the objective function, it is possible to construct "risk averse" designs that result in less deviation from the nominal performance.

Robust design methodology has also been applied to optimize both airfoils and turbomachinery blades in the presence of geometric variability. Robust optimization has been applied to the probabilistic design of airfoil sections subject to variability in the geometric parameters that define the airfoil shape [16, 30, 34, 59]. Garzon employed a gradient-based technique to minimize the mean and standard deviation of the loss coefficient in subsonic and transonic compressor blades [29]. Goodhand et al. redesigned the leading edge of a high pressure compressor rotor by altering only the pressure surface of the blade. This redesign avoids the region of the design space where manufacturing variations result in flow separation [33].

1.2.4 Tolerance Synthesis

Tolerance synthesis, or tolerance optimization, is the process of allocating the component tolerances that result in a desired performance of the overall system [37]. Most work in tolerance synthesis is heavily influenced by the pioneering work of Taguchi, who recognized the need to balance the competing objectives of minimizing production costs and maximizing product quality [74]. Taguchi defined the quality loss function which measures the squared deviation of a product feature from its nominal value. The tolerances can be optimized by minimizing the sum of the manufacturing costs and the expected quality loss [38, 53, 77].

Taguchi's principles have been extended to perform simultaneous robust and tolerance design. For example, Chan et al. consider the design of an RL circuit where the nominal values of the resistance R and inductance L can be varied continuously and the tolerances on these component values can take two discrete values [11]. The nominal values and tolerances are optimized by performing alternating sequential optimizations, first optimizing the nominal values of R and L, then optimizing their tolerances. This process is repeated until the nominal values and tolerances don't

change.

Little work has been published on compressor blade tolerance optimization. Garzon considered the effects of increasing the amplitude of the manufacturing noise by altering the contribution of the PCA modes in Equation (1.1) through the noise amplitude a:

$$\tilde{\mathbf{x}} = \mathbf{x}_0 + \bar{\mathbf{x}} + a \sum_{i=1}^{K} \sqrt{\lambda_i} \mathbf{v}_i \xi_i. \tag{1.2}$$

The effect of increasing the manufacturing variability, which is equivalent to relaxing the manufacturing tolerances, on the mean loss is shown in Figure 1-4, where the red line represents the loss computed for the mean blade geometry with $a = 0$, and the blue line shows the mean loss computed by increasing the noise amplitude. The trend illustrates that the detrimental impact of manufacturing variability grows nonlinearly as the amplitude of these manufacturing variations increases. Garzon did not consider

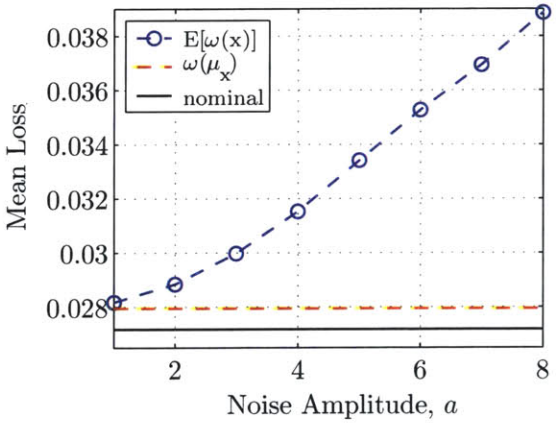

Figure 1-4: Dependence of mean loss on manufacturing noise amplitude (from [27]).

the impact of scaling the manufacturing variability by different amounts in different regions of the blade. We use this approach to perform tolerance optimization in Chapters 2 and 3.

Lamb developed a tolerance design approach based on classifying manufactured compressor blades according to their performance [47]. Blades were characterized as adequately performing if their incidence range was above a certain value. Tolerances on a set of geometric parameters, such as leading edge profile and chord length, were

then chosen to minimize the probability of incorrect classification, i.e. the sum of the number of inadequately performing blades that are accepted and the number of adequately performing blades that are rejected divided by the total number of blades. Lamb found that tolerances that were optimized assuming a given blade geometry were ineffective when the blade geometry was changed, which suggests that the optimal tolerances depend on the blade geometry. One limitation of this approach to tolerancing is that tolerances are imposed on geometric parameters, rather than specific locations on the blade surface, which limits the resolution of the tolerancing scheme.

Duffner used linear sensitivity analysis to specify manufacturing tolerances for the entire surface of a turbine blade [20]. By specifying a maximum allowable performance deviation, the sensitivity of the performance to geometric perturbations in a particular region was used to compute a maximum allowable geometric perturbation. This approach was used to specify a distribution of tolerances to ensure variations in the exit flow angle and loss coefficient did not exceed a critical value. The main limitation of this approach is that linear sensitivity analysis cannot capture the mean shift in performance resulting from nonlinear flow mechanisms such as transition and separation. The tolerance bands constructed by Duffner therefore cannot be optimized to control the mean performance. Moreover, these tolerance bands do not incorporate the known patterns of manufacturing variability. The tolerance optimization method developed in this thesis addresses these shortcomings by incorporating typical manufacturing variations when optimizing the mean performance.

1.3 Thesis Objectives

The objectives of this thesis are to:

- Develop and apply a framework for tolerance optimization of compressor blades. This framework should optimize the mean performance of manufactured blades, and should specify tolerances at every point on the blade surface.

- Determine the circumstances under which deterministic design practices are appropriate as opposed to more computationally expensive robust design practices, and recommend when manufacturing tolerances should be optimized simultaneously with the geometry.

1.4 Contributions

The primary contributions of this thesis are:

- The development of a gradient-based tolerance optimization framework. This framework can be incorporated into a robust geometry optimization framework to optimize both the design intent geometry and manufacturing tolerances. For two subsonic blades where flow separation was the dominant mechanism that increased the mean loss, application of this framework resulted in novel "double bow-tie" tolerance schemes.

- Assessment of the impact of manufacturing variability on the optimal blade geometry. The optimal multi-point design is found to be insensitive to manufacturing variations, provided the design variables modify the geometry on length scales larger than the length scale of the manufacturing variations. In this case, a deterministic geometry optimization approach is appropriate.

1.5 Outline

This thesis is organized into four chapters. Chapter 2 presents a Gaussian random field model of manufacturing variability that is used to determine the impact of manufacturing variability on mean compressor performance. A tolerance design framework is presented and applied to two blade geometries. In Chapter 3, optimization of the blade geometry and tolerances is performed, and the impact of manufacturing variability on the optimal design is determined. Chapter 4 presents a summary of the thesis and offers suggestions for future work.

Chapter 2

Compressor Blade Manufacturing Tolerance Design

This chapter presents a framework for designing compressor blade manufacturing tolerances. Tolerance design is cast as an optimization problem with the objective of improving the mean performance of the manufactured compressor blades. A diagrammatic representation of the tolerance optimization procedure is shown in Figure 2-1. The proposed framework is probabilistic: the mean performance of compressor blades that are statistically similar to measured blades is used to define the performance objectives. The mean performance is controlled by specifying the distribution of manufacturing tolerances on the blade surface, and a gradient-based optimizer is used to design the distribution of manufacturing tolerances.

The manufacturing tolerances are optimized for two subsonic compressor blades. The optimal tolerance scheme for both geometries is found to follow a "double bow-tie" pattern that reduces tolerances on both the pressure and suction side of the leading edge. This tolerance scheme reduces the extent of flow separation at positive and negative incidence angles, and shifts the mean transition location on both sides of the blade towards the trailing edge at the design incidence.

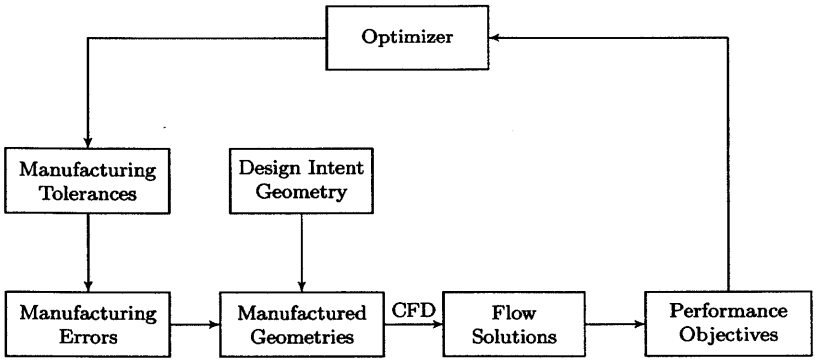

Figure 2-1: Block diagram illustrating the tolerance optimization framework.

2.1 Random Field Model of Manufacturing Variability

Compressor blade manufacturing variability is an example of spatially distributed uncertainty, and is therefore modeled as a random field. Given a probability space $(\Theta, \mathcal{F}, \mathbb{P})$ and a metric space S, a random field is a measurable mapping $e : \Theta \to \mathbb{R}^S$ [2]. The manufacturing error, defined as the distance between the manufactured surface and the nominal surface in the direction normal to the nominal surface, is modeled as a random field $e(s, \theta)$. The coordinates of the manufactured surface x are given by

$$x(s, \theta) = x_d(s) + e(s, \theta)\hat{n}(s), \tag{2.1}$$

where $\hat{n}$ is the surface normal. The surface of the nominal blade is parameterized by an approximate arc length coordinate $-1 \leq s \leq 1$, with negative values along the pressure side and positive values along the suction side, as illustrated in Figure 2-2. The leading edge falls directly on $s = 0$. Although the pressure and suction sides of the blade may have different lengths, this difference is small relative to the total arclength for thin blades, and the difference in length between the two sides is ignored when parameterizing the blade surface.

The use of Gaussian random fields to model compressor blade manufacturing vari-

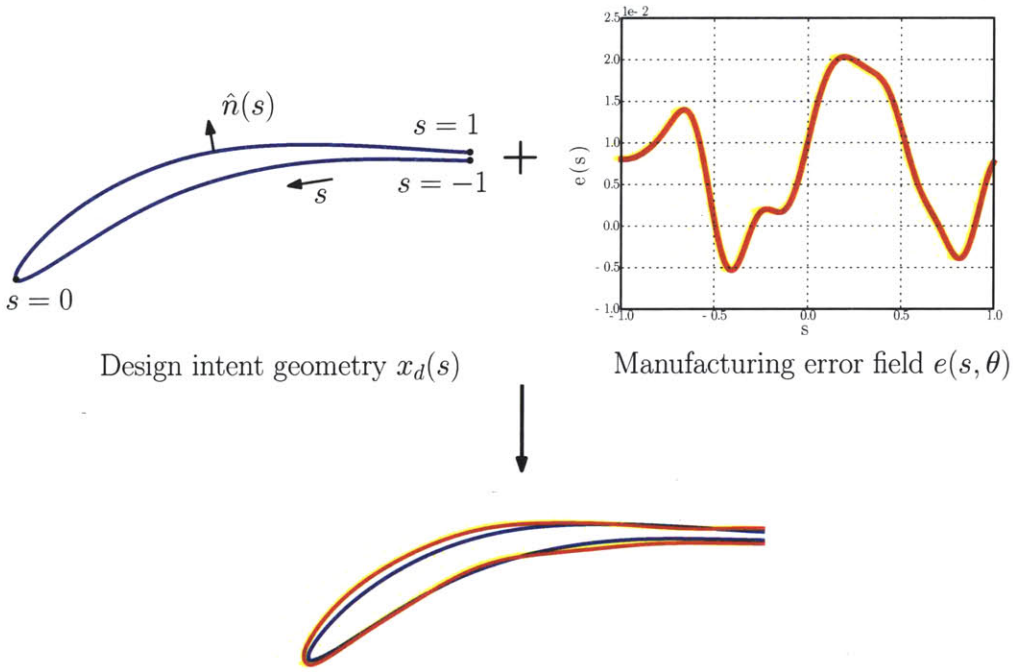

Figure 2-2: Arc length coordinate convention and mapping of manufacturing error field.

ability is motivated by the measurement data from the works cited in Chapter 1, which show that manufacturing variations in blade geometries are often normally distributed. The defining characteristic of Gaussian random fields is that for any $s_1, ..., s_n$, the vector $\{e(s_1, \theta), ..., e(s_n, \theta)\}$ is distributed as a multivariate Gaussian. Gaussian random fields are uniquely defined by their mean $\bar{e}(s)$ and covariance function $C(s_1, s_2)$:

$$\bar{e}(s) = \mathbb{E}[e(s, \theta)],$$

$$C(s_1, s_2) = \mathbb{E}[(e(s_1, \theta) - \bar{e}(s_1))(e(s_2, \theta) - \bar{e}(s_2))],$$

where the expectations are taken over θ. The covariance function describes the smoothness and correlation length, i.e. the characteristic length scale over which the correlation function decays, of the random field.

The covariance function used to model compressor blade manufacturing variations captures both the smoothness and non-stationarity of measured manufacturing variations. The smoothness of a random field is determined by the smoothness of its sample paths. A random field e has k-times continuously differentiable sample paths with probability one if

$$\mathbb{P}\left(\{\theta : e(s, \theta) \in C^k\}\right) = 1,$$

where C^k is the class of k-times continuously differentiable functions on S [1]. The surfaces of manufactured compressor blades do not change discontinuously or have any sharp edges [32]. We therefore expect that the sample paths of the random field $e(s, \theta)$ are at least C^1 continuous with probability one.

The continuity of a Gaussian random field is determined by the choice of mean and covariance function. The mean $\bar{e}(s)$ must be k-times continuously differentiable for the sample paths of the random field $e(s, \theta)$ to be k-times continuously differentiable. If the covariance function $C(s_1, s_2)$ is also k-times continuously differentiable at $s_1 = s_2$, then the random field $e(s, \theta)$ is k-times continuously differentiable with probability one [1].

Another characteristic of compressor blade manufacturing variability is that it is non-stationary. A random field is stationary if its joint probability distribution does not change when shifted in space, i.e. for any shift t,

$$\bar{e}(s+t) = \bar{e}(s),$$

$$C(s_1+t, s_2+t) = C(s_1, s_2).$$

Previous PCA models of compressor blade variability show that the correlation length of the manufacturing variations is non-stationary. Near the leading and trailing edges, the correlation length is smaller than on the rest of the blade. This results in different bluntness and radius of curvature at the leading and trailing edges for different manufactured blades. This is observed in the dominant PCA modes computed in [27] and [48], where these modes are more oscillatory near the leading and trailing edges.

To produce compressor blades with these features, the squared exponential covariance function with a non-stationary correlation length is used. The form of the correlation function (the covariance function divided by the variance) is

$$\rho(s_1, s_2) = \exp\left[-\frac{(s_1 - s_2)^2}{2L^2}\right], \tag{2.2}$$

where the correlation length is given by $L = \sqrt{L'(s_1)L'(s_2)}$, and

$$L'(s) = L_0 + (L_{LE} - L_0)\exp[-(s/w)^2]. \tag{2.3}$$

At the leading edge, the correlation length is L_{LE}, and the correlation length smoothly increases to L_0 away from the leading edge. The parameter w describes the extent of the leading edge and is chosen to be equal to the radius of curvature of the leading edge. The distribution of the correlation length is shown in Figure 2-3. The covariance function given by Equation (2.2) can be shown to produces sample paths that are C^∞ continuous with probability one by using Theorem 2.3 in [1] and noting that the correlation function (2.2) is infinitely differentiable at $s_1 = s_2$. Figure 2-4 shows

realizations of a random field produced with parameters $L_{LE} = 0.01$, $L_0 = 0.4$ and $w = 0.04$. When these realizations are mapped to the compressor blade surface, the leading edge of some blades is made blunter, and others made sharper, a feature observed in manufactured blades.

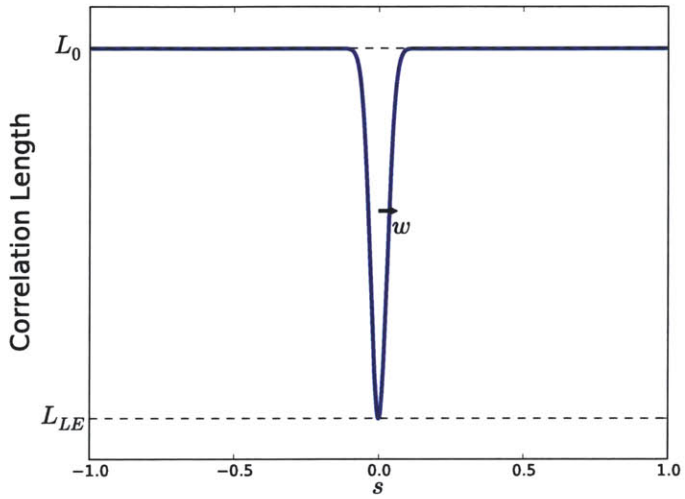

Figure 2-3: Correlation length distribution for a compressor blade.

To select an appropriate noise level, we use the results from Appendix B of [27], where measurement data from both point-milled and flank-milled production compressor blades is presented. Point milling uses a ball-nose cutter to follow a path defined by the interpolating surface of blade design curves. In flank milling, the entire blade surface is shaped in a single pass of the cutting tool, which produces smaller manufacturing deviations than point milling [78]. This is consistent with the data presented in [27], which is reproduced in Figure 2-5.

The random deviation in the leading edge thickness δt_{LE} is the sum of two deviations on the suction side and pressure side, i.e. $\delta t_{LE} = \delta_{SS} + \delta_{PS}$. Assuming the deviations are normally distributed with zero mean, variance σ^2, and correlation ρ, the deviation in the leading edge thickness will be normally distributed as well. Specifically, $\delta t_{LE} \sim \mathcal{N}(0, \sigma^2_{t_{LE}})$, where $\sigma_{t_{LE}} = \sqrt{2(1-\rho)}\sigma$. From the point-milled data provided in Appendix B of [27], the standard deviation of the leading edge thickness

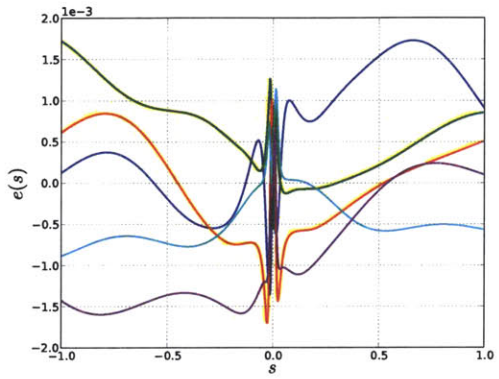

(a) Realizations of the random field

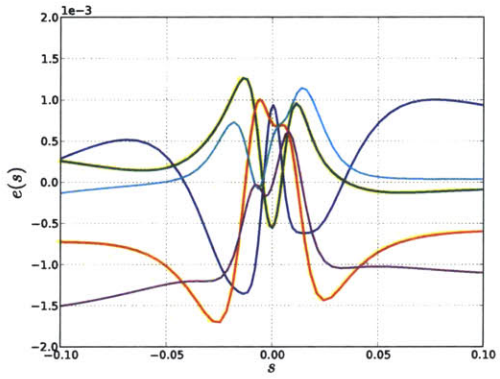

(b) Detail of realizations near $s = 0$

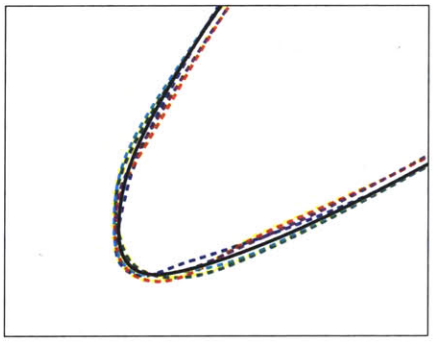

(c) Leading edge corresponding to realizations

Figure 2-4: Realizations of a random process with non-stationary correlation length. The resulting leading edge shape corresponding to each realization is shown at the bottom, with the design intent geometry shown in black.

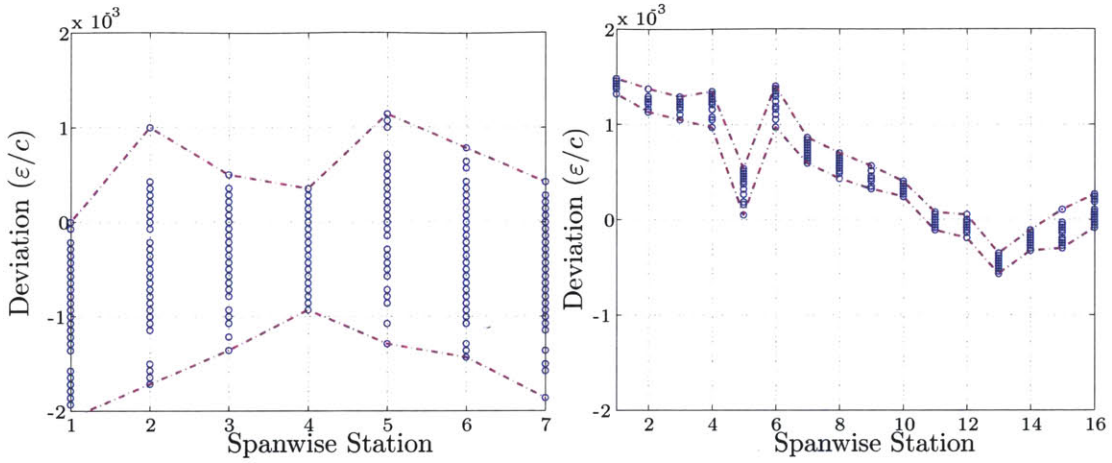

(a) Point-milled (b) Flank-milled

Figure 2-5: Measured deviations in leading edge thickness (from [27]).

is estimated to be $\sigma_{t_{LE}}/c = 10^{-3}$, where c is the chord length. Thus, an upper bound on the standard deviation of manufacturing variations produced by point milling is $\sigma_{PM}/c = 3.5 \times 10^{-4}$. Similar analysis gives an upper bound of $\sigma_{FM}/c = 6.0 \times 10^{-5}$ for flank-milled blades.

The scaling study performed by Garzon in [27] showed that for realistic levels of manufacturing variability, the mean shift in the loss coefficient resulting from changes in the mean geometry account for less than 15% of the total mean shift. Since the performance impact of changes in the mean geometry are small compared to the impact associated with increased variability, changes in the mean geometry are not modeled and the error field is assumed to have zero mean.

2.1.1 The Karhunen-Loève Expansion

There are a number of methods for simulating random fields, including methods based on the fast Fourier transform (FFT) [70] and the local average subdivision method [23]. We use the Karhunen-Loève (K-L) expansion since the sensitivity information required for performing tolerance optimization is readily computed from the K-L expansion.

The Karhunen-Loève expansion, also referred to as the proper orthogonal decomposition (POD), represents a random field as a spectral decomposition of its covariance

function:

$$e(s,\theta) = \bar{e}(s) + \sum_{i\geq 1} \sqrt{\lambda_i}\phi_i(s)\xi_i(\theta), \tag{2.4}$$

where λ_i and $\phi_i(s)$ are the eigenvalues and eigenfunctions of the covariance function, respectively, and the $\xi_i(\theta)$ are mutually uncorrelated random variables with zero mean and unit variance [54]. For a Gaussian random field, the $\xi_i(\theta)$ are i.i.d. standard normal random variables [52]. In Equation (2.4), the eigenvalues are arranged in descending order such that $\lambda_1 \geq \lambda_2 \geq ... \rightarrow 0$. A detailed derivation of the K-L expansion is provided in Appendix A.

The truncated K-L expansion results from truncating (2.4) at a finite number of terms N_{KL}:

$$\hat{e}(s,\theta) = \bar{e}(s) + \sum_{i=1}^{N_{KL}} \sqrt{\lambda_i}\phi_i(s)\xi_i(\theta). \tag{2.5}$$

The decay of the eigenvalues determines the rate of convergence of the truncated K-L expansion. Specifically, the mean squared error of the truncated expansion is given by

$$\mathbb{E}\left[\|e(s,\cdot) - \hat{e}(s,\cdot)\|_S^2\right] = \sum_{i>N_{KL}} \lambda_i.$$

The level of truncation N_{KL} is set equal to the smallest k such that the partial scatter S_k exceeds some threshold, where the partial scatter is defined as

$$S_k = \frac{\sum_{i=1}^{k} \lambda_i}{\sum_{i=1}^{N_s} \lambda_i}.$$

Samples of the random field $\hat{e}(s,\theta)$ are generated by sampling N_{KL} i.i.d. Gaussian random variables $\xi_i(\theta)$ and constructing the realization according to (2.5). In this thesis, we choose N_{KL} to ensure that $S_k > 99.9\%$.

2.2 Probabilistic Axial Compressor Performance Analysis

An axial compressor consists of alternating rows of rotating blades (rotors) and stationary blades (stators). A simplified, two-dimensional representation of a single stage is illustrated in Figure 2-6. The rotor row does work on the flow to increase its total

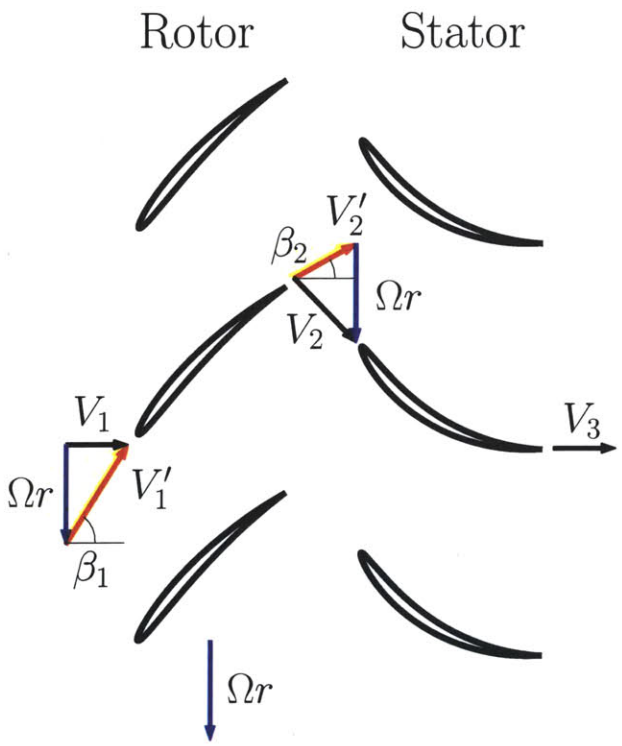

Figure 2-6: Two-dimensional representation of a typical axial compressor stage. Relative velocities are indicated in red, and absolute velocities are indicated in black.

pressure. Assuming the compression process is adiabatic, the rate of work done on a streamtube of flow is

$$\dot{w} = \dot{m}(h_{o2} - h_{o1}) = \dot{m}\Delta h_o,$$

where $\dot{m}$ is the mass flow through the streamtube, h is the enthalpy, and the subscript $()_o$ denotes a stagnation quantity. The change in total enthalpy across the rotor row

is computed using the Euler turbine equation:

$$\Delta h_o = \Omega(r_2 v_2 - r_1 v_1),$$

where r is the streamtube radius, Ω is the angular velocity of the rotor, and v is the tangential velocity. If the change in the streamtube radius is small relative to r_1, the Euler turbine equation simplifies to

$$\Delta h_o = \Omega r[u_2 \tan(\beta_1 + \Delta\beta) - u_1 \tan(\beta_1)],$$

Assuming that the change in axial velocity is small compared to the axial velocity u_1 and that the rotational speed of the rotor is fixed, the work done by the rotor is determined by the flow turning $\Delta\beta$.

The stator removes the flow swirl introduced by the rotor to align the flow for the rotor of the next stage. It is important for a stator row to produce the correct outflow angle since the performance of the following rotor row is sensitive to the flow incidence angle produced by the upstream stator. The outflow angle β_2 of the stator is therefore a relevant performance metric.

To quantify the losses across a rotor or stator row, we use the total pressure loss coefficient:

$$\bar{\omega} = \frac{p_{o2}^{isen} - p_{o2}}{p_{o1} - p_1}, \tag{2.6}$$

where p_{o2}^{isen} is the total pressure downstream of the blade assuming isentropic flow. The over-bar notation in $\bar{\omega}$ refers to a mixed-out flow state. The over-bar notation denotes the mean for all other quantities in this thesis.

2.2.1 MISES Flow Solver

The MISES (Multiple blade Interacting Streamtube Euler Solver) turbomachinery analysis code is used to compute the loss coefficient and flow turning for the manufactured blade geometries. MISES utilizes a zonal approach to compute the flow

solution. The boundary layer and wake are modeled by solving the integral boundary layer equations [18]. In the inviscid regions of the flow field, the steady state Euler equations are discretized over a streamline conforming grid. MISES can be used for both 2D and quasi-3D analysis, in which case the Euler equations are projected onto an axisymmetric stream-surface. The inviscid and viscous regions of the flow are coupled through the boundary layer displacement thickness. The Newton-Raphson method is used to solve the set of nonlinear equations describing the flow field and any user specified boundary conditions or airfoil shape modifications [80]. MISES was modified to include a user specified geometric mode describing the manufacturing error. As part of the flow solution, MISES applies the specified manufacturing error perturbation in the surface normal direction.

A convenient feature of MISES is its solution speed. A typical flow solution requires 10-20 Newton-Raphson iterations to converge, which are completed in a few seconds. MISES also offers the option to reconverge a flow solution after perturbing the blade shape. Since the perturbations in the geometry introduced by manufacturing variability are small relative to the blade chord, the flow field corresponding to manufactured blades can be reconverged from the flow field of the nominal geometry with an order of magnitude fewer Newton-Raphson iterations than were required to converge the original flow solution.

Another attractive feature of MISES is its ability to model laminar-turbulent transition in the boundary layer. This feature is important to accurately model the performance of blades where viscous loss is the dominant loss mechanism, since the viscous loss depends on whether the flow is laminar or turbulent. MISES includes both e^n and Abu-Ghannam-Shaw (AGS) bypass transition models [19]. MISES can also model shock-induced and trailing edge separation.

In MISES, the total pressure loss coefficient $\bar{\omega}$ is computed using the mixed-out state (density, velocity and pressure) downstream of the blade where the flow state is uniform in the annular direction. The mixed-out state is assumed to have the same total mass flow, momentum and total enthalpy as the flow at a user specified plane

downstream of the blade. MISES uses a blunt trailing edge model, which assumes a semi-circular trailing edge profile [19]. Thus, geometric variability in the trailing edge is not considered.

2.2.2 Monte Carlo Uncertainty Propagation

The performance impact of manufacturing variability is quantified in terms of the statistics of the outputs of interest. Given the distribution of the geometric variability, i.e. the distribution of $\boldsymbol{\xi}(\theta) = \{\xi_1(\theta), ..., \xi_{N_{KL}}(\theta)\}$ in the K-L expansion (2.5), the statistics of the loss coefficient and turning are computed using the Monte Carlo method [66]. These statistics include the mean

$$\mu_{\bar{\omega}} := \mathbb{E}[\bar{\omega}(\boldsymbol{\xi})] = \int_{\Theta} \bar{\omega}(\boldsymbol{\xi})\ \mathbb{P}(d\boldsymbol{\xi}),$$

$$\mu_{\Delta\beta} := \mathbb{E}[\Delta\beta(\boldsymbol{\xi})] = \int_{\Theta} \Delta\beta(\boldsymbol{\xi})\ \mathbb{P}(d\boldsymbol{\xi}),$$

and variance

$$\sigma^2_{\bar{\omega}} := \mathrm{Var}[\bar{\omega}(\boldsymbol{\xi})] = \int_{\Theta} [\bar{\omega}(\boldsymbol{\xi}) - \mu_{\bar{\omega}}]^2\ \mathbb{P}(d\boldsymbol{\xi}),$$

$$\sigma^2_{\Delta\beta} := \mathrm{Var}[\Delta\beta(\boldsymbol{\xi})] = \int_{\Theta} [\Delta\beta(\boldsymbol{\xi}) - \mu_{\Delta\beta}]^2\ \mathbb{P}(d\boldsymbol{\xi}).$$

The direct dependence of $\bar{\omega}$ and $\Delta\beta$ on $\boldsymbol{\xi}$ is not explicitly known, so these integrals cannot be computed analytically. The Monte Carlo method approximates these integrals by repeatedly drawing i.i.d. samples $\boldsymbol{\xi}^{(n)}$, $n = 1, ..., N$ from the joint distribution of $\boldsymbol{\xi}$ and computing the corresponding output quantities of interest $\bar{\omega}(\boldsymbol{\xi}^{(n)})$ for each sample. Unbiased estimates of the mean loss coefficient and mean turning are

$$\hat{\mu}_{\bar{\omega}} = \frac{1}{N}\sum_{n=1}^{N} \bar{\omega}(\boldsymbol{\xi}^{(n)}),$$

$$\hat{\mu}_{\Delta\beta} = \frac{1}{N}\sum_{n=1}^{N} \Delta\beta(\boldsymbol{\xi}^{(n)}).$$

Each Monte Carlo sample is processed using the following steps:

- Generate i.i.d. Gaussian vector $\boldsymbol{\xi}$
- Construct the random error field using the K-L expansion given by Equation (2.5)
- Construct the "manufactured" blade geometry using Equation (2.1)
- Compute the flow solution for the manufactured blade using MISES
- Evaluate the performance quantities of interest, i.e. the loss and flow turning, from the flow solution

The evaluation of the performance statistics is illustrated diagrammatically in Figure 2-7.

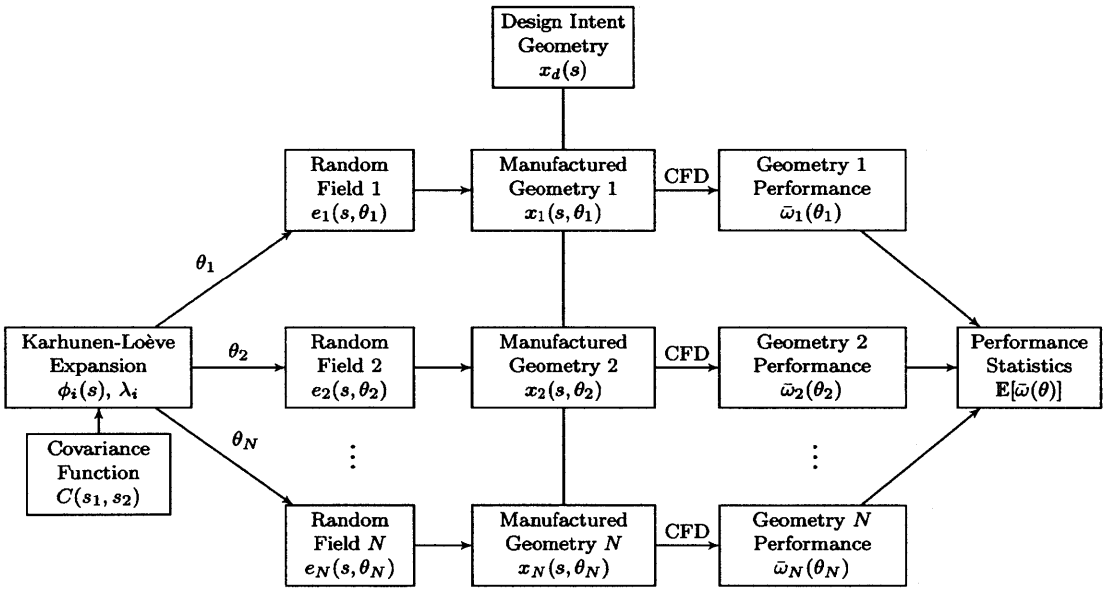

Figure 2-7: Block diagram illustrating the propagation of manufacturing variability to estimate performance statistics.

The Monte Carlo estimates $\hat{\mu}_{\bar{\omega}}$ and $\hat{\mu}_{\Delta\beta}$ are random variables, with mean $\mu_{\bar{\omega}}$ and

$\mu_{\Delta\beta}$, respectively. The standard error of these Monte Carlo estimates are

$$\varepsilon_{\hat{\mu}_{\bar{\omega}}} = \sqrt{\frac{1}{N}\mathrm{Var}(\bar{\omega})}$$

and

$$\varepsilon_{\hat{\mu}_{\Delta\beta}} = \sqrt{\frac{1}{N}\mathrm{Var}(\Delta\beta)}.$$

Thus, the error in the Monte Carlo estimates decreases like $N^{-1/2}$. Since the distributions of $\bar{\omega}$ and $\Delta\beta$ are not known, the variance term in the expression for the standard error is replaced by an unbiased estimate:

$$\hat{\sigma}^2_{\bar{\omega}} = \frac{1}{N-1}\sum_{n=1}^{N}[\bar{\omega}(\boldsymbol{\xi}^{(n)}) - \hat{\mu}_{\bar{\omega}}]^2,$$

$$\hat{\sigma}^2_{\Delta\beta} = \frac{1}{N-1}\sum_{n=1}^{N}[\Delta\beta(\boldsymbol{\xi}^{(n)}) - \hat{\mu}_{\bar{\omega}}]^2.$$

Estimates for higher moments can be constructed, but in robust optimization, the mean and variance are used most commonly. It is also possible to estimate the probability density function of the outputs of interest from the Monte Carlo samples using techniques such as kernel density estimation [60].

2.2.3 Impact of Manufacturing Variability on an Exit Guide Vane and Rotor Blade

2.2.3.1 UTRC Fan Exit Guide Vane

The first geometry we consider is a two-dimensional fan exit guide vane developed by UTRC. Following reference [72], the design inlet Mach number is $M_1 = 0.73$, and the design inflow angle is $\beta_1 = 43.2°$. The Reynolds number based on the blade chord is 1.0×10^6, and a turbulence intensity of 4% was selected to reflect conditions in a typical compressor stage [9]. To replicate the streamtube contraction measured in [72], an axial velocity density ratio (AVDR) of 1.12 is specified. At the design intent

conditions, the loss coefficient computed by MISES is $\bar{\omega} = 2.24 \times 10^{-2}$, which is in good agreement with the experimental results reported in [72]. The Mach contours and pressure coefficient over the blade are plotted for three different incidence angles in Figures 2-8 and 2-9, respectively. At the design incidence, a weak shock forms on the suction surface of the blade at 18% of the chord. At negative incidence the shock increases in strength and moves towards the trailing edge. The shock strength also increases at positive incidence, but the shock location moves towards the leading edge.

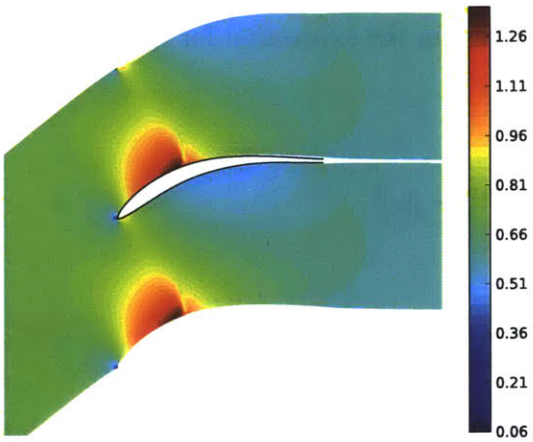

(a) Mach contours at $\beta_1 = 38.7°$

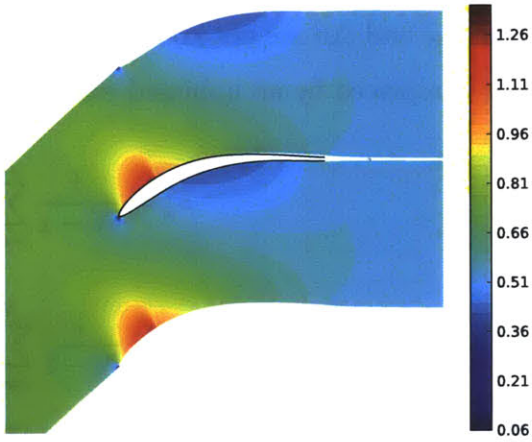

(b) Mach contours at $\beta_1 = 43.2°$

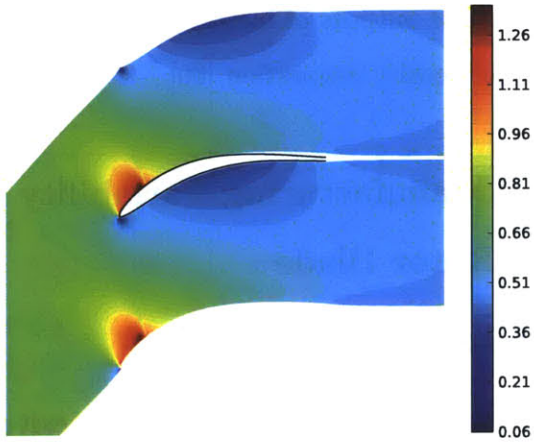

(c) Mach contours at $\beta_1 = 47.7°$

Figure 2-8: Mach contours from MISES simulations of the UTRC exit guide vane, $M_1 = 0.73$, AVDR $= 1.12$, $Re = 1.0 \times 10^6$.

The manufacturing noise model was applied to determine the impacts of man-

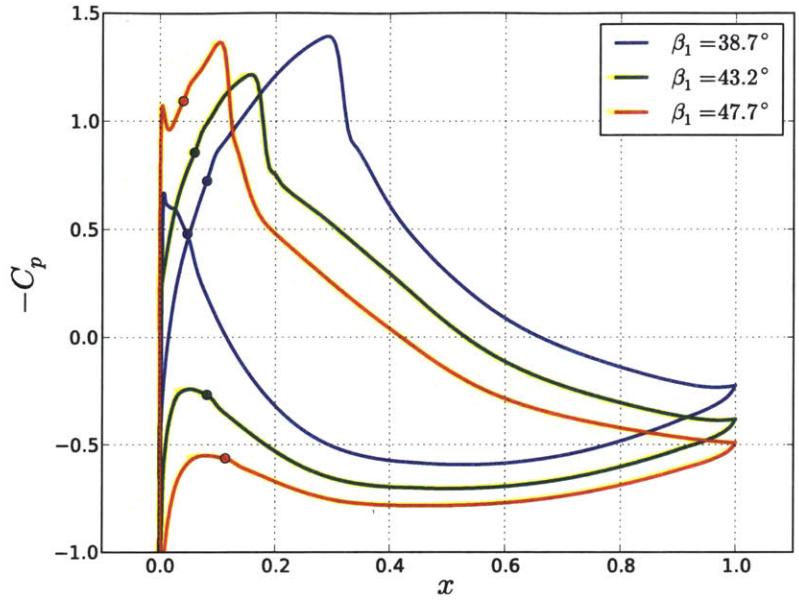

Figure 2-9: Pressure coefficient from MISES simulations of the UTRC exit guide vane, $M_1 = 0.73$, AVDR $= 1.12$, $Re = 1.0 \times 10^6$. The dots indicate the transition location.

ufacturing variability on the UTRC blade. The level of noise was specified to be $\sigma/c = 8.0 \times 10^{-4}$, roughly twice the level of noise found for point-milled blades in [27]. Choosing a level of noise larger than that produced by a known, high noise manufacturing process is motivated by the tolerance optimization framework. The proposed framework, described in the next section, starts from a set of loose manufacturing tolerances and restricts the tolerances in the regions where geometric variations have the largest impact.

At the leading edge, the correlation length is four times smaller than the leading edge radius of curvature to give $L_{LE} = 0.01$ in Equation (2.3), ensuring realizations with varying bluntness are produced. The other correlation parameters were $w = 0.04$ (equal to the leading edge radius of curvature) and $L_0 = 0.4$ (ten times the leading edge radius of curvature). All lengths are nondimensionalized by the blade arclength. The number of Monte Carlo samples was chosen such that the standard error of the mean loss coefficient is less than 5.0×10^{-5}, so that the Monte Carlo estimates of the

loss coefficient are accurate to within 1.0×10^{-4} with 95% confidence. For the UTRC blade, $N = 5,000$ samples were found to be sufficient.

Figure 2-10 shows the relation between the loss coefficient and incidence angle $\alpha = \beta_1 - \beta_1^{des}$ for the UTRC blade, referred to as the loss bucket. The blue line shows the loss coefficient for the nominal blade, and the red line shows the mean loss coefficient of the manufactured blades. The shaded red region spans the 2.5% - 97.5% quantiles, illustrating both the amount of variability in the loss coefficient and any asymmetry in the distribution of the loss coefficient. At the design incidence, the shift in the mean loss coefficient is 1% of the nominal loss coefficient. Both the shift in mean loss and the amount of loss variability grow on either side of the design incidence, which agrees qualitatively with the loss bucket of a transonic compressor subject to manufacturing variations reported by Goodhand et al. [32]. For the incidence angles considered, the largest increase in the mean loss is 16%, which occurs at $\alpha = -4.8°$, and the average increase in mean loss is 3%.

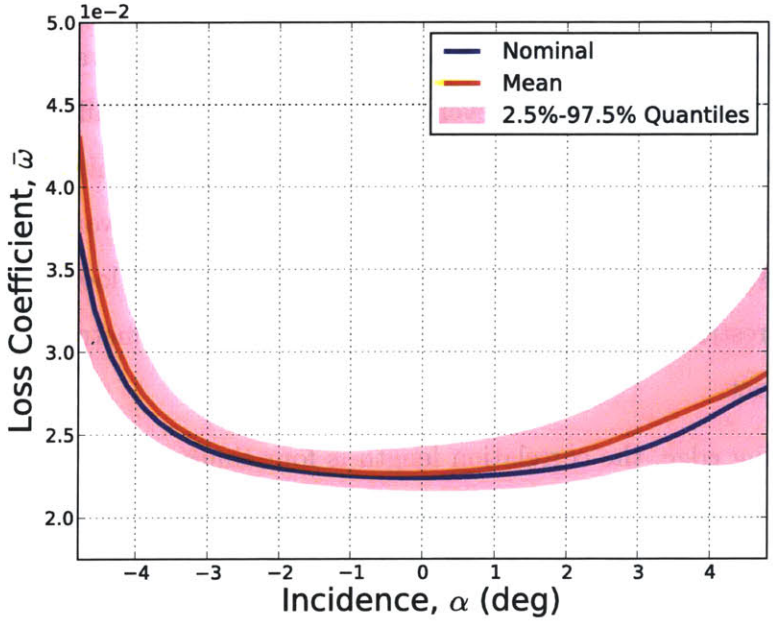

Figure 2-10: Loss coefficient versus incidence angle for the UTRC exit guide vane.

Histograms of the loss coefficient for three different inflow angles, $\beta_1 = 38.7°$,

β_1	38.7°	43.2°	47.7°
$\bar{\omega}_0$	3.16×10^{-2}	2.24×10^{-2}	2.76×10^{-2}
$\mathbb{E}[\bar{\omega}]$	3.35×10^{-2}	2.27×10^{-2}	2.84×10^{-2}
β_2	$-0.76°$	$-0.63°$	$-0.27°$
$\mathbb{E}[\beta_2]$	$-0.72°$	$-0.63°$	$-0.26°$

Table 2.1: Nominal and mean performance of the UTRC blade for three incidence angles.

$\beta_1 = 43.2°$, and $\beta_1 = 47.7°$ are shown in Figure 2-11. The distribution of loss is positively skewed at each incidence angle, which leads to a mean shift in the loss coefficient. Table 2.1 summarizes the nominal and mean performance of the UTRC blade. At each incidence angle, the mean shift in the outflow angle β_2 is negligible. This is unsurprising since variability in blade stagger angle is not modeled.

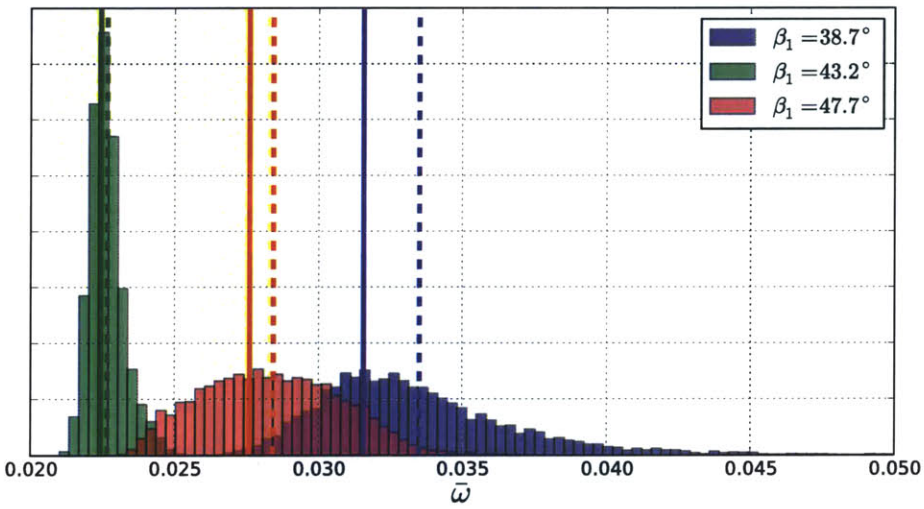

Figure 2-11: Histograms of loss coefficient at three different incidence angles for the UTRC blade. The solid lines indicate the nominal loss, and the dashed lines indicate the mean loss.

2.2.3.2 SC10 Rotor

The second geometry is the two-dimensional Standard Configuration 10 (SC10) rotor blade, which is a modified NACA0006 airfoil with a circular camber line [26]. The

design inlet Mach number is $M_1 = 0.7$ and the design inflow angle is $\beta_1 = 53.5°$. Following reference [61], the Reynolds number based on the blade chord is 1.26×10^6. No streamtube contraction was assumed, so the AVDR was set to 1.0. At the design conditions, the loss coefficient is $\bar{\omega} = 1.52 \times 10^{-2}$. The Mach contours and pressure coefficient profiles are plotted for three different incidence angles in Figures 2-12 and 2-13, respectively. At the design inlet Mach and inflow angle, the flow is free of any shocks. At positive incidence, a shock is present on the suction surface near the leading edge.

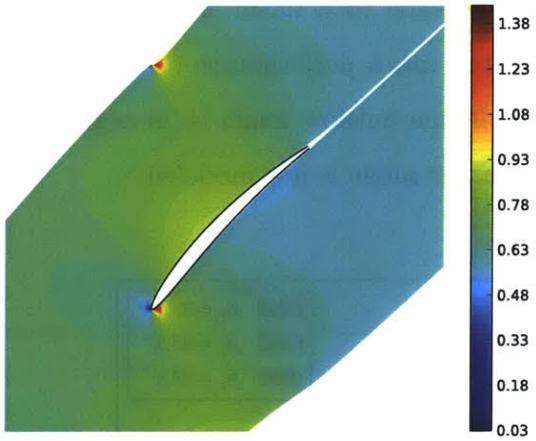

(a) Mach contours at $\beta_1 = 48.5°$

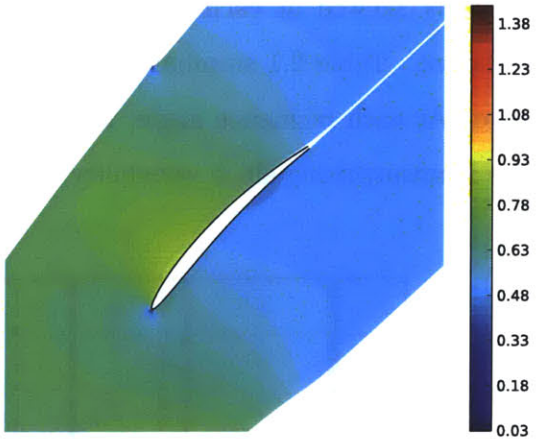

(b) Mach contours at $\beta_1 = 53.5°$

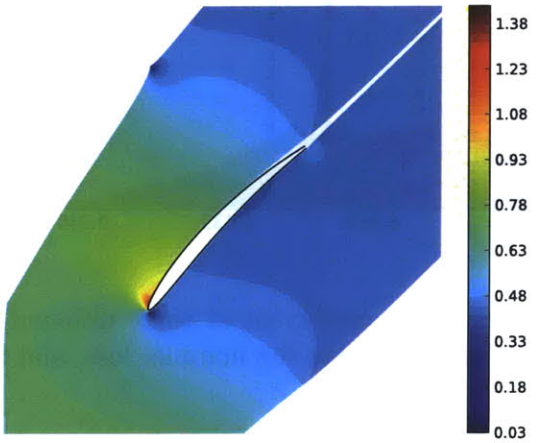

(c) Mach contours at $\beta_1 = 58.5°$

Figure 2-12: Mach contours from MISES simulations of the SC10 rotor blade, $M_1 = 0.7$, AVDR $= 1.00$, $Re = 1.26 \times 10^6$.

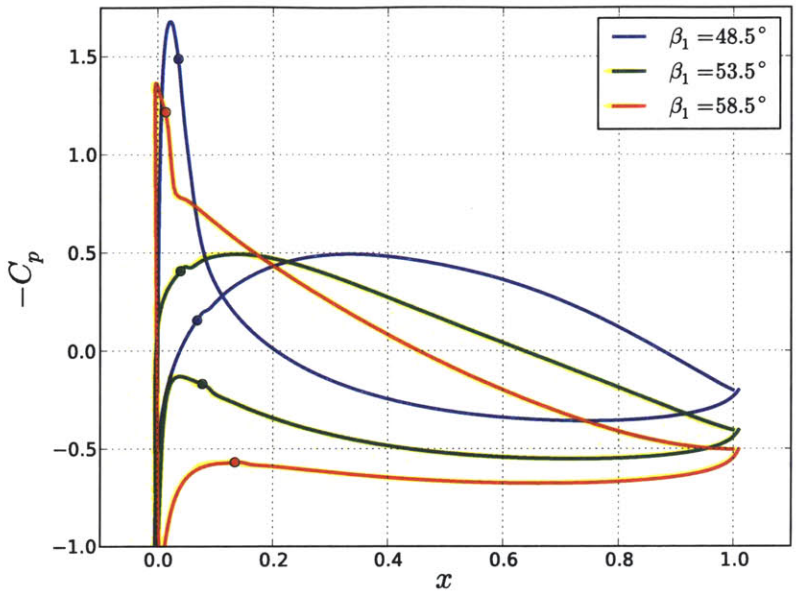

Figure 2-13: Pressure coefficient from MISES simulations of the SC10 rotor blade, $M_1 = 0.7$, AVDR = 1.00, $Re = 1.26 \times 10^6$. The dots indicate the transition location.

For the SC10 geometry, the level of variability was specified to be $\sigma/c = 6.0 \times 10^{-4}$. The level of variability is lower than the level applied to the UTRC blade since the SC10 blade is thinner, and larger levels of variability resulted in realizations with invalid leading edge shapes. The correlation length was four times smaller than the leading edge radius of curvature to give $L_{LE} = 0.0095$. The other correlation parameters were $w = 0.038$ (equal to the leading edge radius of curvature) and $L_0 = 0.4$. For the SC10 blade, $N = 5,000$ Monte Carlo samples were again found to be sufficient to estimate the mean loss to an accuracy of 1.0×10^{-4} with 95% confidence. The loss bucket for the SC10 blade is plotted in Figure 2-14. Qualitatively, the loss bucket of the SC10 rotor is similar to that of the UTRC exit guide vane: the mean shift in loss is 1% of the nominal loss at the design incidence, and increases as the incidence is either increased or decreased. For the incidence angles considered, the largest increase in the mean loss is 16%, which occurs at $\alpha = 5.6°$, and the average increase in mean loss is 6%.

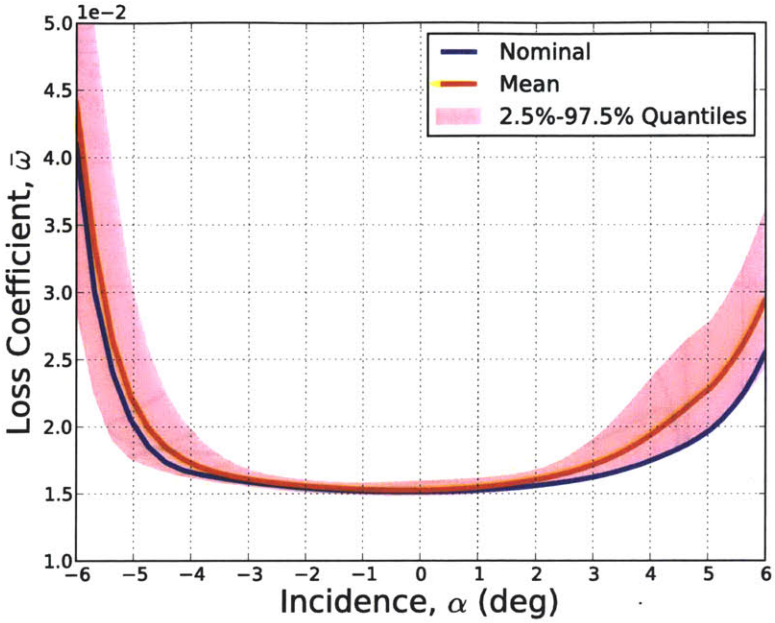

Figure 2-14: Loss coefficient versus incidence angle for the SC10 rotor blade.

β_1	48.5°	53.5°	58.5°
$\bar{\omega}_0$	2.02×10^{-2}	1.52×10^{-2}	1.96×10^{-2}
$\mathbb{E}[\bar{\omega}]$	2.19×10^{-2}	1.53×10^{-2}	2.25×10^{-2}
β_2	42.46°	42.63°	43.91°
$\mathbb{E}[\beta_2]$	42.54°	42.64°	44.10°

Table 2.2: Nominal and mean performance of the SC10 rotor for three incidence angles.

Histograms of the loss coefficient for three different incidence angles, $\beta_1 = 48.5°$, $\beta_1 = 53.5°$, and $\beta_1 = 58.5°$ are shown in Figure 2-15. As was the case for the UTRC blade, the distribution of loss is positively skewed at each incidence angle. The nominal and mean performance of the SC10 blade is summarized in Table 2.2. At each incidence angle, the mean shift in the outflow angle β_2 is small, meaning the changes in the mean rotor work can be ignored.

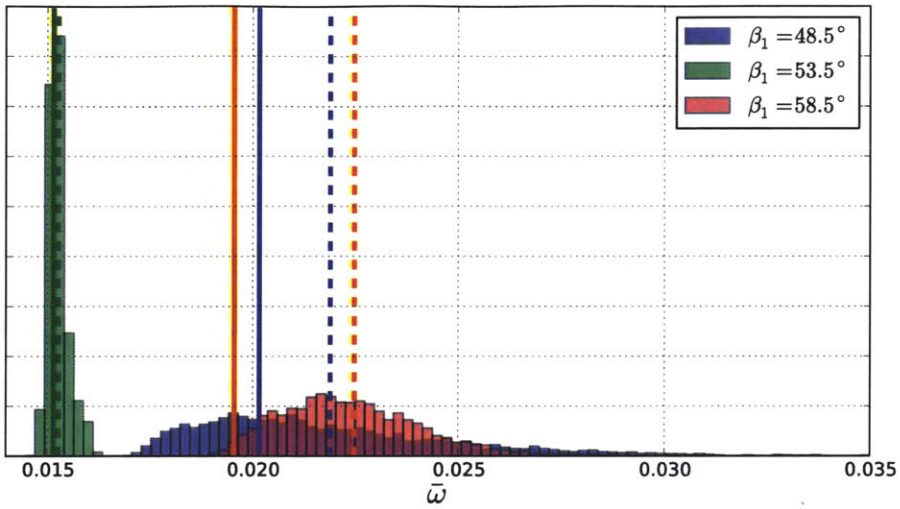

Figure 2-15: Histograms of loss coefficient at three different incidence angles for the SC10 blade. The solid lines indicate the nominal loss, and the dashed lines indicate the mean loss.

2.3 Manufacturing Tolerance Optimization Framework

2.3.1 Variance Based Tolerance Specification

The precision of a manufacturing process is specified in terms of its spread, defined as some multiple of the standard deviation of the dimension of interest, where a dimension refers to the size of a particular feature [44]. To specify manufacturing tolerances around a compressor blade surface, we specify the process spread, equal to the standard deviation $\sigma(s)$, at every point on the blade surface. The relation between tolerances and variance is illustrated in figure 2-16. The leading edge of the nominal blade geometry is shown in black. The $2\sigma(s)$ bounds on the geometric variability are shown in dashed red lines, and sample realizations of manufactured blade geometries are plotted in color. The left figure demonstrates loose tolerances, where larger variations are allowed as compared to the case where strict tolerances are imposed, shown on the right. The variance is also non-stationary, decreasing near the

leading edge in both cases.

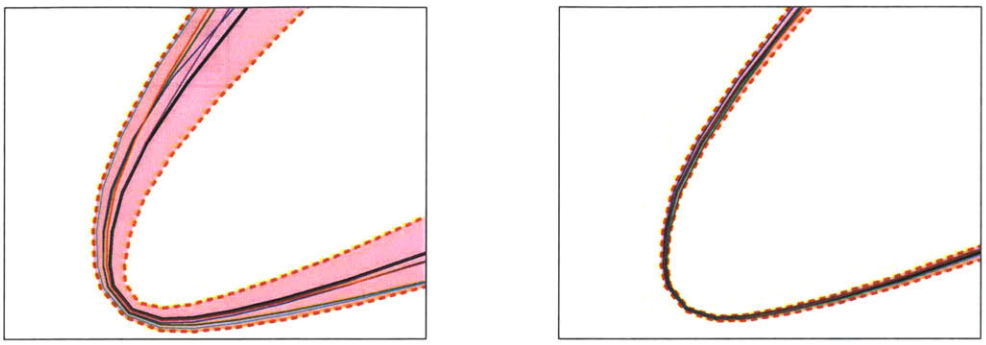

(a) (b)

Figure 2-16: Illustration of loose (a) and strict (b) tolerances in the leading edge of a compressor blade.

To represent the standard deviation field, we introduce a basis $\{B_{i,n}(s)\}_{i=1}^{N_\sigma}$ and represent $\sigma(s)$ as a linear combination of the basis functions. The basis functions are chosen to be B-spline basis functions of degree $n = 3$. The B-spline basis is constructed from a knot vector $\mathbf{k} \in \mathbb{R}^{N_k}$, with $k_i \leq k_{i+1}$, dividing the interval $[-1, 1]$ into knot spans. Each of the B-spline basis functions is a piecewise polynomial function of degree n, and are non-zero on $n + 1$ knot spans. The B-spline basis functions are $(n - m - 1)$ times continuously differentiable at a knot with multiplicity m $(\leq n)$ [62]. The standard deviation field $\sigma(s)$ is expressed in terms of the B-spline basis as:

$$\sigma(s) = \sum_{i=1}^{N_\sigma} \sigma_i B_{i,n}(s).$$

Figure 2-17 illustrates a cubic B-spline basis and the knots used to construct them. For clarity, the knot spacing is chosen to be equal in Figure 2-17.

Although any real valued function $\sigma(s)$ results in a valid random field, the standard deviation is constrained to be positive everywhere. If $\sigma(s)$ goes to zero at some location s_0, this implies that there is no geometric variability at s_0, i.e. that the manufacturing process has infinite precision. It is assumed that no manufacturing process can achieve

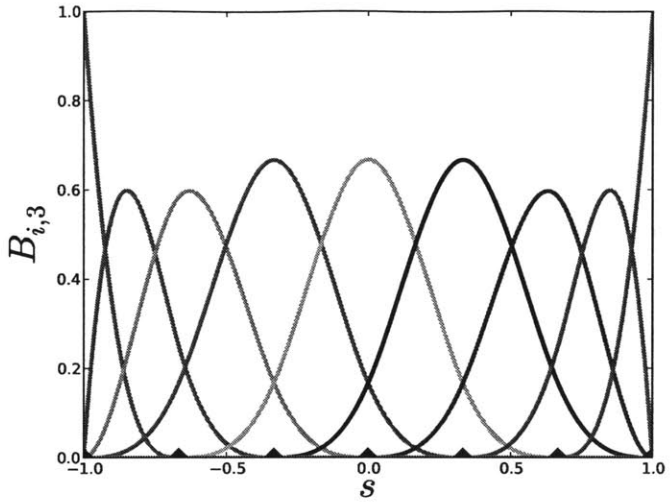

Figure 2-17: Collection of cubic B-spline basis functions, with knot locations shown on the abscissa.

infinite precision, and thus $\sigma(s)$ is constrained to be greater than zero everywhere.

The proposed tolerance model is related to the scaling study performed by Garzon as described in Chapter 1. The parameter a multiplying the PCA modes in Equation (1.2) scales the standard deviation of the manufacturing variations everywhere on the blade surface. In the proposed model, the scaling is allowed to vary in different regions of the blade, allowing the impact of manufacturing variations in different regions of the blade to be compared.

2.3.2 Objectives and Constraints for Tolerance Optimization

In the proposed tolerance optimization framework, the mean compressor performance is controlled by specifying $\sigma(s)$. We focus on optimizing the mean performance, as opposed to other statistics such as the variance, since evidence from previous robust optimizations of compressor blades found that optimizing the mean performance tends to also reduce the performance variability relative to the baseline design [4, 27]. As the results of the last section illustrated, the change in the mean turning due to manufacturing variations is small relative to the baseline turning. We therefore do

not constrain the mean turning when optimizing the manufacturing tolerances.

Since the mean shift in loss coefficient is sensitive to the flow incidence, we design the manufacturing tolerances to minimize the mean loss coefficient over a range of incidence angles by adopting a multi-point design strategy similar to that used in [6] and [45]. A set of N_p design points is chosen, each corresponding to an incidence angle. A weighted objective function is defined as the weighted sum of the loss coefficient at each incidence angle, i.e.

$$J = \sum_{i=1}^{N_p} w_i \bar{\omega}(\beta_i),$$

where the weight vector $\mathbf{w} = \{w_1, ..., w_{N_p}\}$ weights the relative importance of different incidence angles. The weight vector is chosen so that the multi-point objective function J approximates a weighted integral of the loss coefficient:

$$\sum_{i=1}^{N_p} w_i \bar{\omega}(\beta_i) \approx \int_{\mathcal{B}} W(\beta)\bar{\omega}(\beta)\, d\beta,$$

where $W(\beta)$ is a weighting function and $\mathcal{B} = [\beta_1^l, \beta_1^u]$ is the incidence range of interest. Choosing $N_p = 3$ equispaced points and a loss weight vector $\mathbf{w} = \{1/4, 1/2, 1/4\}$ approximates the average loss computed using a trapezoidal integration rule.

The tolerance design process determines where on the blade surface the tolerances should be reduced to have the most benefit, i.e. to provide the greatest reduction in the mean loss coefficient. This is achieved by constraining the level of manufacturing variability, and minimizing the weighted mean loss $\mathbb{E}[J]$. To quantify the level of variability, we introduce the function $V(\boldsymbol{\sigma})$, equal to the integral of the standard deviation of the random field that models the manufacturing variations over the blade surface:

$$V(\boldsymbol{\sigma}) = \int_S \sigma(s; \boldsymbol{\sigma})\, ds. \tag{2.7}$$

Reducing V implies stricter tolerances and therefore increased manufacturing cost. In the optimization, the standard deviation is also bounded from above by a specified value σ_{max} to ensure that the optimizer does not trade increases in the variability in

regions of low mean loss sensitivity for decreases in high sensitivity regions and drive $\sigma(s)$ to zero.

The optimization problem for designing the tolerances is summarized below:

$$\begin{aligned} \boldsymbol{\sigma}^* = \quad & \arg\min_{\boldsymbol{\sigma}} \quad \mathbb{E}[J(\theta, \boldsymbol{\sigma})] \\ & \text{s.t.} \quad V(\boldsymbol{\sigma}) = V_b \\ & \qquad 0 \leq \sigma(s) \leq \sigma_{max}. \end{aligned} \tag{2.8}$$

This optimization problem is solved using the sample average approximation method, which is described subsequently.

2.3.3 Sample Average Approximation

The sample average approximation (SAA) method, also referred to as sample path optimization, is used to compute an approximate solution of (2.8). The SAA method replaces the objective function $\mathbb{E}[J(\theta, \boldsymbol{\sigma})]$ with a Monte Carlo estimate $\hat{\mu}_J^{(N)}(\boldsymbol{\sigma})$ computed using a fixed set of random inputs, i.e. a fixed set of realizations $\{\boldsymbol{\xi}^{(n)}\}_{n=1}^N$ of the random input vector used to generate realizations of the error field $e(s, \theta)$. Fixing the random inputs transforms the stochastic optimization problem (2.8) into a deterministic optimization problem. The solution of the deterministic optimization problem, denoted $\hat{\boldsymbol{\sigma}}_N^*$, is an estimator of the true solution $\boldsymbol{\sigma}^*$, converges to the true solution at an asymptotic rate of $O(N^{-1/2})$, and can be shown to be asymptotically normally distributed [67].

We use the sequential quadratic programming (SQP) method to solve the deterministic optimization problem that approximates the stochastic problem (2.8). The SQP method updates the approximate solution by solving a quadratic subproblem [63]. At each SQP iteration, the quadratic subproblem is formed by constructing the Lagrangian function from the objective and constraint functions. The Lagrangian is approximated by its second-order Taylor series expansion, where the Hessian is estimated using a quasi-Newton update formula, such as the Broyden-Fletcher-Goldfarb-

Shanno (BFGS) formula [8]. The solution of the quadratic subproblem produces a search direction, and a linesearch is applied to determine the step length.

2.3.4 Pathwise Sensitivity Estimates

To apply the SAA method, we need to compute gradients of the approximate objective function, i.e. $\nabla_{\boldsymbol{\sigma}} \hat{\mu}_J^{(N)}$. To do this, we use the pathwise sensitivity method. The pathwise sensitivity method relies upon interchanging the differentiation and expectation operators, thereby constructing an unbiased estimator of the gradient by taking the gradient of an unbiased estimator. To compute an unbiased estimator of the gradient of the objective function $\mathbb{E}[J(\theta, \boldsymbol{\sigma})]$ with respect to the design vector $\boldsymbol{\sigma}$, we interchange differentiation and integration:

$$\frac{\partial}{\partial \boldsymbol{\sigma}} \mathbb{E}[J(\theta, \boldsymbol{\sigma})] = \mathbb{E}\left[\frac{\partial}{\partial \boldsymbol{\sigma}} J(\theta, \boldsymbol{\sigma})\right].$$

Sufficient conditions that allow for this interchange are given in Appendix B.

Replacing the objective function with its Monte Carlo estimate, and exchanging summation and differentiation gives

$$\frac{\partial}{\partial \boldsymbol{\sigma}} \mathbb{E}[J(\theta, \boldsymbol{\sigma})] \approx \frac{\partial \hat{\mu}_J^{(N)}}{\partial \boldsymbol{\sigma}} = \frac{1}{N} \sum_{n=1}^{N} \frac{\partial J_n}{\partial \boldsymbol{\sigma}}.$$

Since we are using the SAA method, the derivatives $\partial J_n / \partial \boldsymbol{\sigma}$ represent the sensitivity of the random functional $J(\theta, \boldsymbol{\sigma})$ for a particular realization of the random field $e_n \equiv e(s, \boldsymbol{\xi}^{(n)})$ where all random inputs are held fixed. The sensitivity $\partial J_n / \partial \boldsymbol{\sigma}$ is computed using the chain rule:

$$\frac{\partial J_n}{\partial \sigma_i} = \frac{\delta J_n}{\delta e_n} \frac{\partial e_n}{\partial \sigma_i}, \qquad i = 1, ..., N_\sigma$$

To compute the sample path sensitivity $\partial e_n / \partial \sigma_i$, we first define the random field $\tilde{e}(s, \theta) = e(s, \theta)/\sigma(s)$. The random field $\tilde{e}(s, \theta)$ has the same correlation function as $e(s, \theta)$, and the variance of $\tilde{e}(s, \theta)$ is equal to one everywhere. Realizations of the random field $e(s, \theta)$, which has variance $\sigma^2(s)$, can be produced by simulating the unit

variance random field $\tilde{e}(s,\theta)$ and scaling the realizations by $\sigma(s)$. The sample path sensitivity of a realization $e_n(s)$ with respect to the tolerance design variable σ_i is computed using the chain rule:

$$\frac{\partial e_n(s)}{\partial \sigma_i} = \frac{\partial e_n(s)}{\partial \sigma(s)} \frac{\partial \sigma(s)}{\partial \sigma_i} = \tilde{e}_n(s) B_{i,n}(s),$$

where $B_{i,n}(s)$ is the i^{th} B-spline basis function used to represent $\sigma(s)$.

The sensitivity of the objective function J_n (corresponding to the n^{th} Monte Carlo sample) to the tolerance design variable σ_i is computed using a second order accurate finite difference:

$$\frac{\partial J_n}{\partial \sigma_i} = \frac{J_n(\sigma_i + h) - J_n(\sigma_i - h)}{2h} + O(h^2),$$

where the step size h is small relative to σ_i. Computing the full gradient requires two additional flow solutions to be computed for each tolerance design variable. The computational cost of estimating the gradient with finite differences was reduced by perturbing each design variable and reconverging from the unperturbed flow solution.

An alternative approach to computing shape sensitivities is the direct sensitivity method [80]. In the direct sensitivity method, the Jacobian used in the Newton-Raphson iteration is factored, and the sensitivity of the quantities of interest with respect to geometric perturbations is computed using back substitution. In MISES, the linearization with respect to the variables describing the computational grid are inexact to prevent crossing of adjacent grid lines and ensure solution convergence. This inexact linearization introduces errors into the sensitivities computed using the direct sensitivity method. Relative errors of up to 20% compared to finite difference sensitivities were observed, which motivated the use of the finite difference method for computing all shape sensitivities.

2.3.5 Tolerance Optimization for a Model Problem

The methods described in this chapter are now applied to a model problem whose analytic solution is available. In this problem, the design variables control the variance

of a zero-mean Gaussian random field $e(s,\theta)$, defined on the domain $S = [0,1]$. The correlation function is chosen to be the squared exponential function:

$$\rho(s_1, s_2) = \exp\left[-\frac{(s_1 - s_2)^2}{2L^2}\right],$$

with correlation length $L = 0.1$. The variance $\sigma^2(s)$ of the random field is a spatially dependent function. We seek to minimize the sum of two competing cost functions that depend on $\sigma(s)$ as a (spatially varying) parameter. The first cost function penalizes variability:

$$f_1 = \mathbb{E}\left[\int_0^1 e^2(s,\theta)w(s)\, ds\right], \tag{2.9}$$

where $w(s)$ is a non-negative weighting function that is larger in regions that are more sensitive to variability. The second cost function is inversely proportional to the variability:

$$f_2 = \int_0^1 \frac{1}{\sigma(s)}\, ds$$

We determine the standard deviation field $\sigma^*(s)$ that minimizes the sum of the two cost functions:

$$\sigma^*(s) = \underset{\sigma(s)}{\arg\min} \quad f := f_1 + f_2 \tag{2.10}$$

This model problem is analogous to a tolerance optimization problem, where the improvements in the mean performance are balanced by the costs of reducing tolerances. Reducing tolerances (decreasing the variance $\sigma^2(s)$) improves the mean performance of the system, which is reflected in the cost function f_1. Introducing variability into certain regions of the domain has a larger impact on the mean performance, as expressed by the weight function $w(s)$. It is also costly to reduce tolerances, and the cost of reducing tolerances increases monotonically, as reflected in the form of f_2.

The optimal solution to (2.10) can be derived using the calculus of variations. The expectation and spatial integration can be interchanged in Equation (2.9) to give

$$f_1 = \int_0^1 \mathbb{E}[e^2(s,\theta)]w(s)\, ds = \int_0^1 \sigma^2(s)w(s)\, ds. \tag{2.11}$$

The first variation of f can then be computed directly:

$$\delta f = \int_0^1 \left(2\sigma(s)w(s) - \frac{1}{\sigma^2(s)} \right) \delta\sigma(s)\ ds.$$

Enforcing stationarity by setting $\delta f = 0$, the optimal standard deviation field is found to be

$$\sigma^*(s) = \left[\frac{1}{2w(s)} \right]^{1/3}.$$

This optimum is unique because both f_1 and f_2 are convex functionals of $\sigma(s)$.

The weight function is chosen to be positive and spatially varying. As an example, we choose the weight function to be $w(s) = 2 + \sin(2\pi s)$. The standard deviation field is discretized with $N_\sigma = 20$ cubic B-spline basis functions. The mean performance of engineering systems typically cannot be computed in closed form, and instead must be estimated. We therefore use the Monte Carlo method to compute an unbiased estimate of f_1, rather than computing it directly from Equation (2.11):

$$\hat{f}_1 = \frac{1}{N} \sum_{n=1}^{N} \int_0^1 e_n^2(s) w(s)\ ds.$$

For each Monte Carlo sample, the integral is evaluated using composite Gaussian quadrature with 20 intervals and a third order rule on each interval. The same quadrature rule is used to compute f_2. The SAA equivalent of (2.10) results from replacing the objective function f_1 with its unbiased estimate:

$$\hat{\sigma}^*(s) = \underset{\sigma(s)}{\arg\min} \quad \hat{f}_1 + f_2.$$

This optimization problem is solved using the SQP method with a BFGS update to approximate the Hessian as implemented in the NLopt package [42]. The pathwise estimate of the sensitivity $\delta f_1 / \delta\sigma(s)$, which is an unbiased estimate of the true gradient, is computed as

$$\frac{\delta \hat{f}_1}{\delta\sigma} = \frac{1}{N} \sum_{n=1}^{N} \int_0^1 2w(s) e_n(s) \frac{\partial e_n}{\partial \sigma}\ ds.$$

Figure 2-18 compares sample optimal solutions, shown in blue, with the true solution, shown in red. The shaded blue 95% confidence region is computed by estimating the Hessian matrix $\mathbf{B}$ and covariance $\mathbf{\Sigma}$ using the Monte Carlo samples used to compute the optimal solution:

$$\hat{\mathbf{B}} = \frac{1}{N}\sum_{n=1}^{N} \nabla^2 J(\hat{\sigma}^*),$$

$$\hat{\mathbf{\Sigma}} = \frac{1}{N}\sum_{n=1}^{N} \nabla J(\hat{\sigma}^*)\nabla J(\hat{\sigma}^*)^\intercal,$$

where

$$J = \int_0^1 \frac{1}{\sigma(s)} + e^2(s,\theta)w(s)\ ds.$$

The standard error of the optimal solution is then $\varepsilon_N = [\text{diag}(\hat{\mathbf{B}}^{-1}\hat{\mathbf{\Sigma}}\hat{\mathbf{B}}^{-1})/N]^{1/2}$ [67].

To illustrate the convergence rate of the SAA optimal solution to the true optimal solution, we conduct $M = 10^4$ independent optimization runs for different values of N. Figure 2-19 shows histograms of the error of the SAA optimal solution evaluated at the center of the domain. The histograms resemble Gaussian distributions with standard deviation proportional to $N^{-1/2}$. Figure 2-20 illustrates the convergence of the entire optimal solution and optimal value as N is increased. The standard deviation of the optimal solution error $\hat{\sigma}_N^*(s) - \sigma^*(s)$ is plotted on the left, and the standard deviation of the optimal objective function error $f(\hat{\sigma}_N^*) - f(\sigma^*)$ is plotted on the right. Both the optimal solution error and the error in the objective function converge like $N^{1/2}$: increasing the number of Monte Carlo samples by a factor of 100 gains a one decimal improvement in solution accuracy.

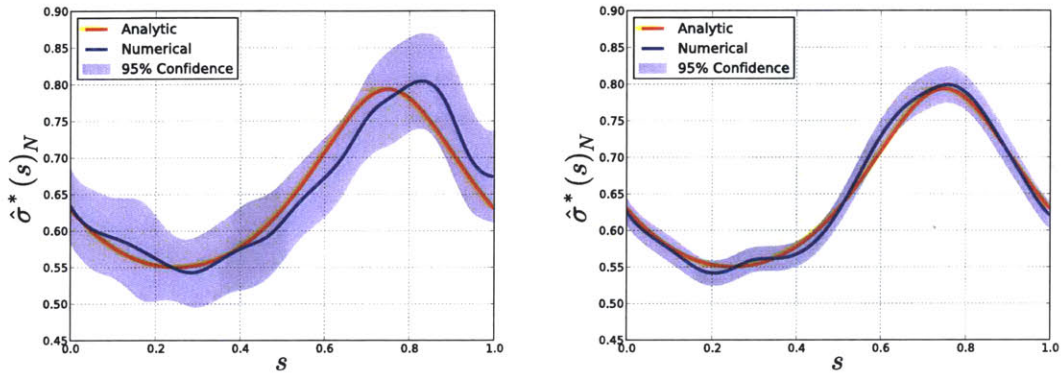

(a) $N = 10^2$

(b) $N = 10^3$

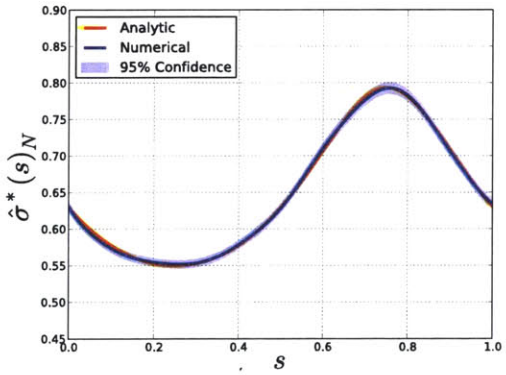

(c) $N = 10^4$

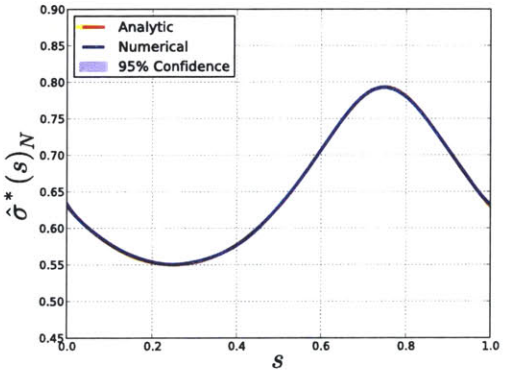

(d) $N = 10^5$

Figure 2-18: Optimal solutions for the model problem obtained with increasing number of Monte Carlo samples.

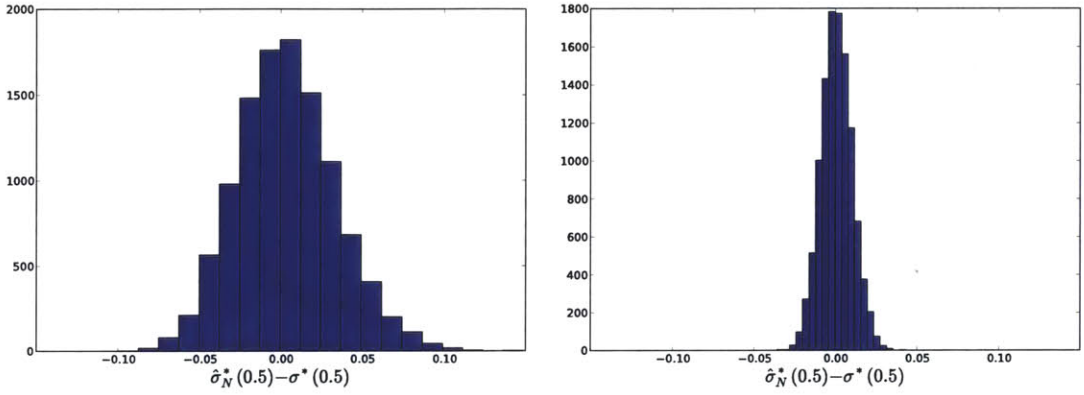

(a) $N = 10^2$

(b) $N = 10^3$

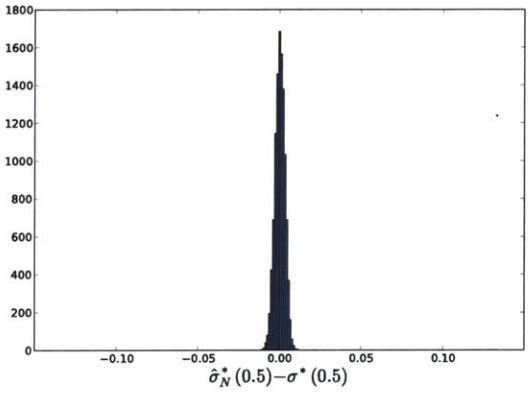

(c) $N = 10^4$

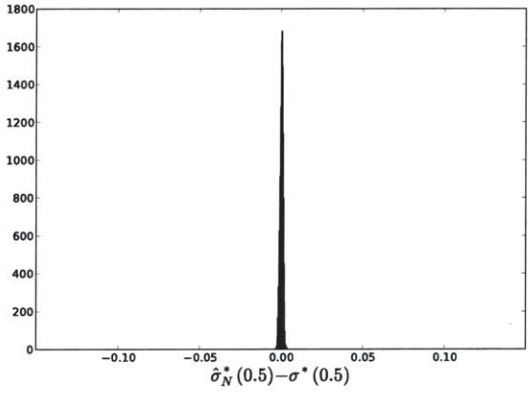

(d) $N = 10^5$

Figure 2-19: Histograms of the solution error at the center of the domain $\hat{\sigma}_N^*(0.5) - \sigma^*(0.5)$ for increasing number of Monte Carlo samples.

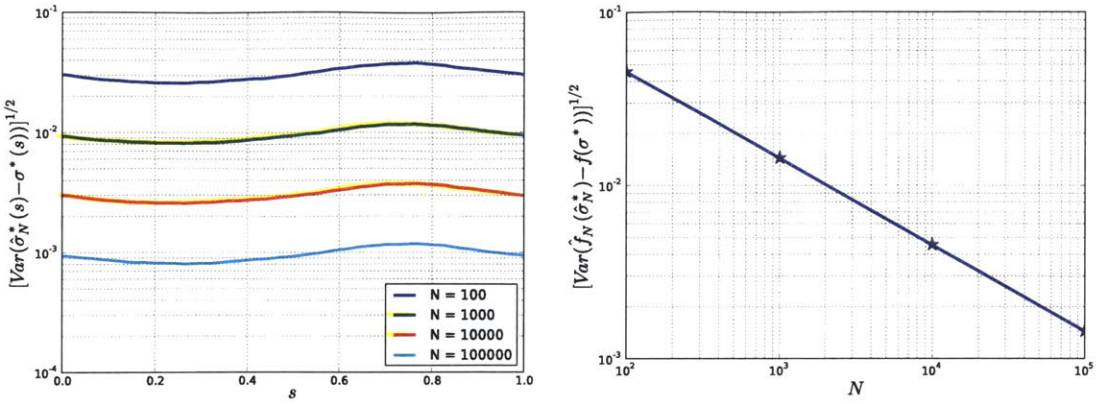

(a) (b)

Figure 2-20: Standard deviations of the optimal solution (a) and optimal objective function value (b).

2.4 Tolerance Optimization of an Exit Guide Vane and Rotor Blade

2.4.1 UTRC Fan Exit Guide Vane

We first optimize the manufacturing tolerances for the UTRC exit guide vane. We use $N_p = 3$ design points at $\beta_1 = 38.7°$, $43.2°$, and $47.7°$ and a loss weight vector $\mathbf{w} = \{1/4,\ 1/2,\ 1/4\}$. The total variability, as quantified by Equation (2.7), is constrained to be 98% of the baseline total variability, and the standard deviation is constrained to be below the baseline value of $\sigma/c = 8.0 \times 10^{-4}$ at all points on the blade surface. The standard deviation is represented using $N_\sigma = 41$ basis functions, and the knot spacing is reduced near the leading edge, since previous studies of the impact of geometric variability on compressor performance suggest that most of the increase in loss results from imperfections near the leading edge [28].

Since each evaluation of the objective function requires Monte Carlo simulation, the total computational cost of optimizing the tolerances grows with the number of Monte Carlo samples used to approximate the mean loss. To offset this cost, we follow the approach outlined by Garzon and use a small number of Monte Carlo samples to

construct "surrogates" of the performance statistics. $N = 500$ Monte Carlo samples are used to estimate the mean loss when optimizing the tolerances, 10% of the number of Monte Carlo samples to evaluate the mean performance in Section 2.2.3. This number was found adequate to successfully redesign blade tolerances in the presence of geometric variability. The optimization was terminated when the mean loss converged within an absolute tolerance of 10^{-5}. The performance statistics of the optimal design were then estimated using $N = 5,000$ Monte Carlo samples.

The convergence history of the mean loss is shown in Figure 2-21. The tolerance optimization converged after 31 SQP iterations, and the mean loss was evaluated 62 times, requiring a total of 31,000 MISES flow solutions. The optimal tolerance scheme is plotted in Figure 2-22. We only show the leading edge since the optimal standard deviation away from the leading edge is equal to the baseline value of $\sigma/c = 8.0 \times 10^{-4}$. The optimal tolerance scheme is found to have a "double bow-tie" pattern: the standard deviation decreases on the pressure side of the blade, increases towards the stagnation point, decreases again on the suction surface before increasing to the baseline value. The tolerances are reduced more on the pressure side than on the suction side. The improvement in the mean loss coefficient resulting from optimizing the tolerances is summarized in Table 2.3, and the loss bucket of the UTRC blade with optimized tolerances is plotted in Figure 2-23. Tolerance optimization reduces the mean shift in loss by an average of 49% over the range of incidence angles shown.

	Baseline	Optimized
$\mathbb{E}[\bar{\omega}(\beta_1^1)]$	3.35×10^{-2}	3.22×10^{-2}
$\mathbb{E}[\bar{\omega}(\beta_1^2)]$	2.27×10^{-2}	2.25×10^{-2}
$\mathbb{E}[\bar{\omega}(\beta_1^3)]$	2.84×10^{-2}	2.83×10^{-2}
$\sum w_i \mathbb{E}[\bar{\omega}(\beta_1^i)]$	2.68×10^{-2}	2.64×10^{-2}

Table 2.3: Comparison of the mean loss for the UTRC blade with baseline and optimized tolerances with 98% of the baseline variability.

At every incidence considered, the shock losses comprise less than 5% of the total loss. We therefore examine the viscous losses generated in the boundary layer to de-

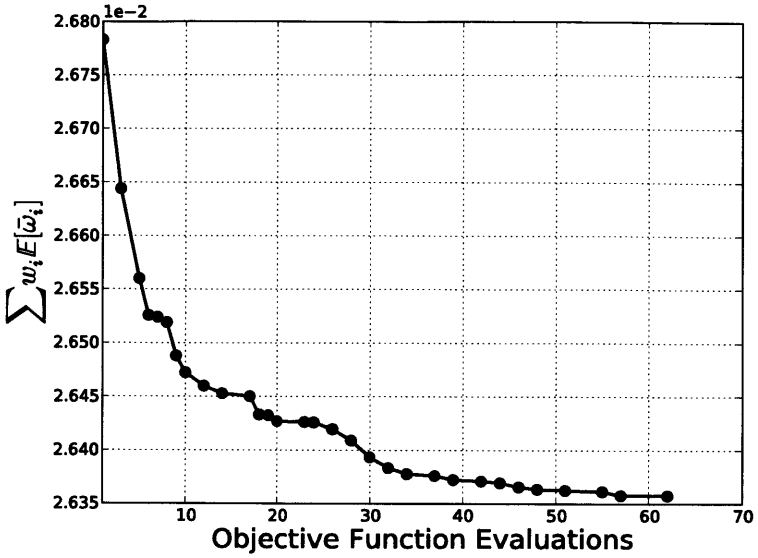

Figure 2-21: Convergence history for the tolerance optimization of the UTRC blade. The dots indicate SQP iterations.

termine the benefit of optimizing the manufacturing tolerances. To quantify the losses generated in the boundary layer, we use the boundary layer dissipation coefficient, defined as

$$C_{\mathcal{D}} = \frac{1}{\rho_e u_e^3} \int_0^\infty \tau \frac{\partial u}{\partial y} \, dy,$$

where ρ_e and u_e are the density and streamwise velocity at the edge of the boundary layer, respectively, τ is the shear stress, and y is the surface normal coordinate. The rate of entropy generation per unit span up to the point s is computed from the dissipation coefficient:

$$\dot{S}_s = \int_0^s \frac{\rho_e u_e^3 C_{\mathcal{D}}}{T_e} ds',$$

where T_e is the boundary layer edge temperature [15]. Since the streamwise variations in T_e are moderate, we examine the cumulative integral of $\rho_e u_e^3 C_{\mathcal{D}}$ to determine where the greatest losses are generated [27]. The cumulative integral of $\rho_e u_e^3 C_{\mathcal{D}}$ is plotted in Figure 2-24 for the UTRC blade with uniform and optimized tolerances. The percent change in the mean total entropy is within 15% of the percent change in the mean loss coefficient for each incidence angle considered.

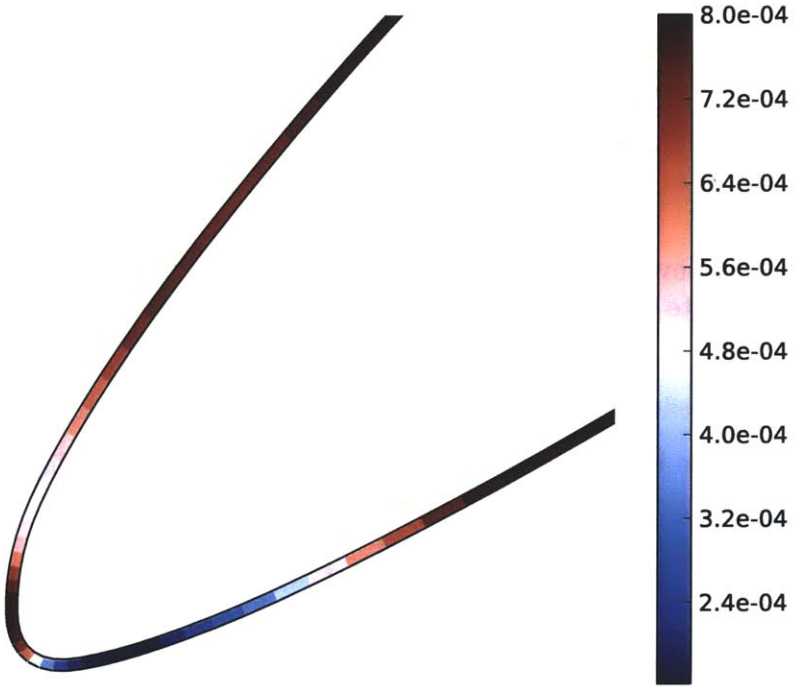

Figure 2-22: Optimal standard deviation for the UTRC blade with 98% of the baseline variability. The lower surface is the pressure side, and the upper surface is the suction side.

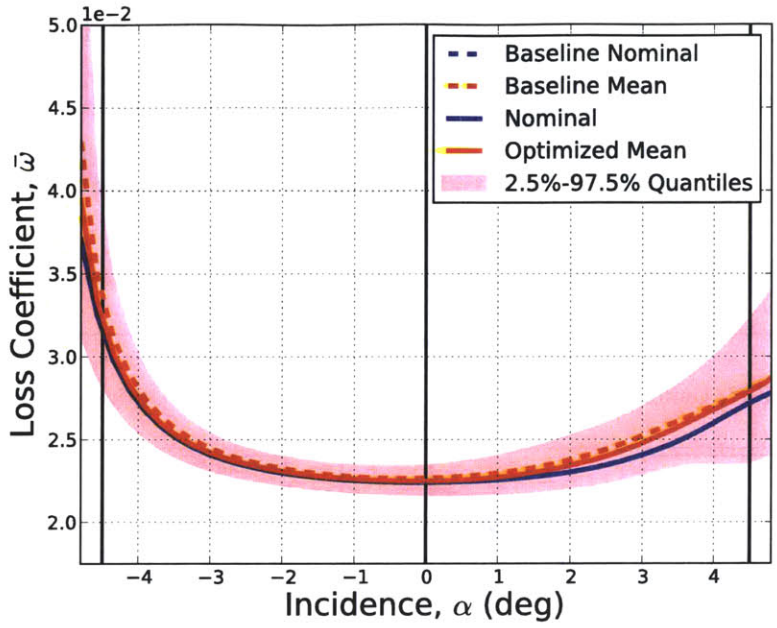

Figure 2-23: Loss coefficient versus incidence angle for the UTRC exit guide vane with optimized tolerances with 98% of the baseline variability.

At negative incidence, the reduced tolerances on the pressure side of the blade prevent pressure side flow separation from occurring for all but two of the 5,000 Monte Carlo samples, whereas pressure side flow separation occurs for 50% of the blades with uniform tolerances. Manufacturing variations that make the leading edge blunter create leading edge pressure spikes, as shown on the left of Figure 2-25. The adverse pressure gradient produced by these pressure spikes induces flow separation on the pressure side of the blade. The optimized tolerances reduce the manufacturing variability on the pressure side of the blade, eliminating the pressure spikes, as shown on the right of Figure 2-25. The effect of preventing pressure side separation is illustrated at the top of Figure 2-24: the mean shift and variability in the pressure side entropy generation is lower with optimized tolerances.

The plots at the top of Figure 2-24 show the effect of the suction side shock that forms at $s = 0.4$. The variability and mean shift in the suction side entropy is a result of variability in the strength of this shock. Figure 2-26 shows that higher shock

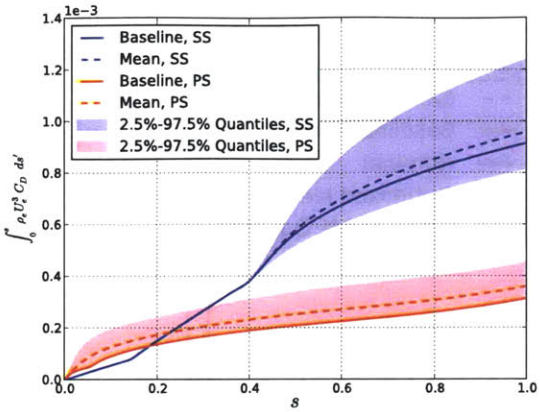

(a) $\beta_1 = 38.7°$, Uniform Tolerances

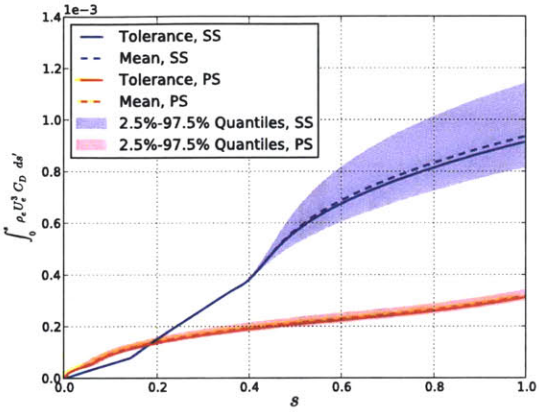

(b) $\beta_1 = 38.7°$, Optimized Tolerances

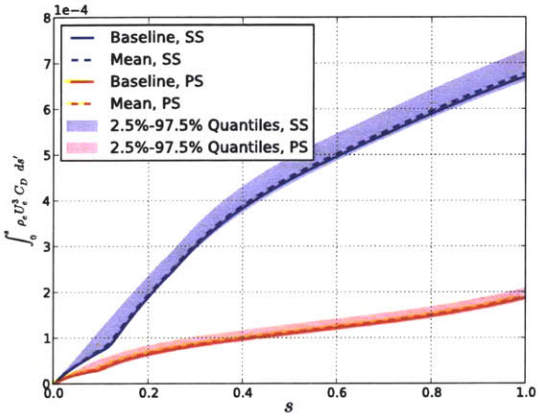

(c) $\beta_1 = 43.2°$, Uniform Tolerances

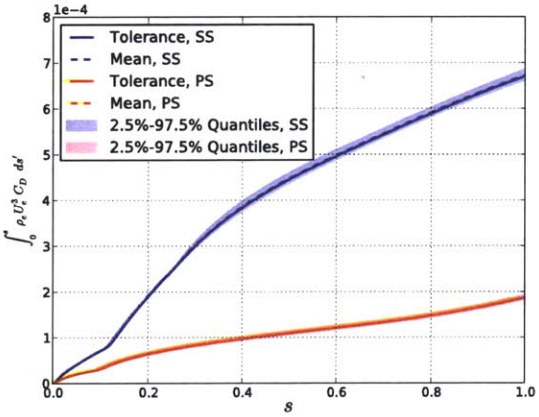

(d) $\beta_1 = 43.2°$, Optimized Tolerances

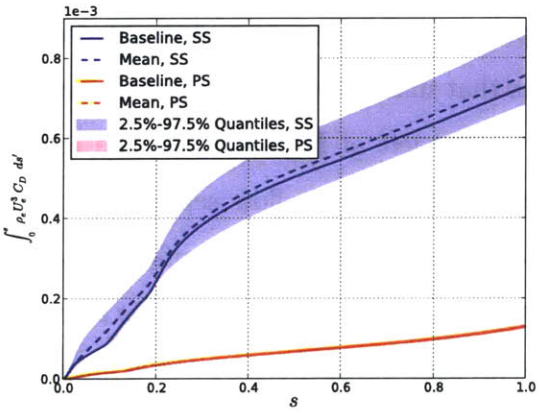

(e) $\beta_1 = 47.7°$, Uniform Tolerances

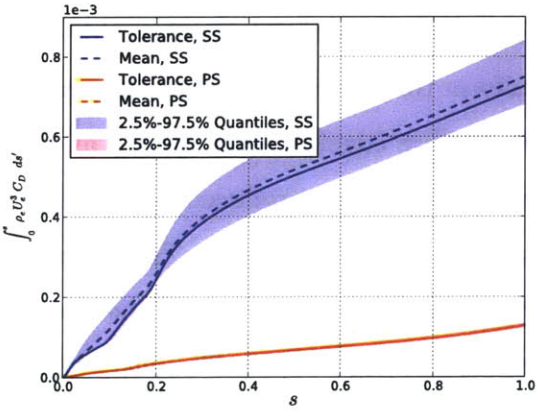

(f) $\beta_1 = 47.7°$, Optimized Tolerances

Figure 2-24: Boundary layer entropy generation rate for the UTRC blade with uniform and optimized tolerances with 98% of the baseline variability. Solid lines indicate the nominal, dashed lines indicate the mean. The pressure side (PS) is plotted in red and the suction side (SS) is plotted in blue.

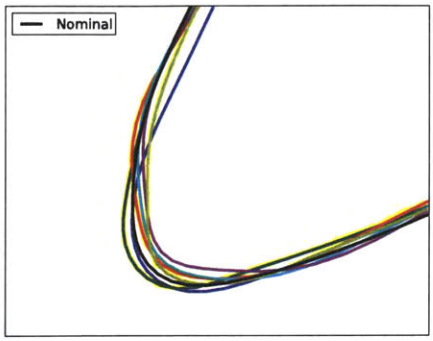

(a) Manufactured Blades, Uniform Tolerances

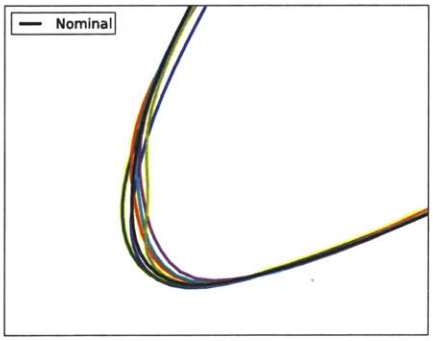

(b) Manufactured Blades, Optimized Tolerances

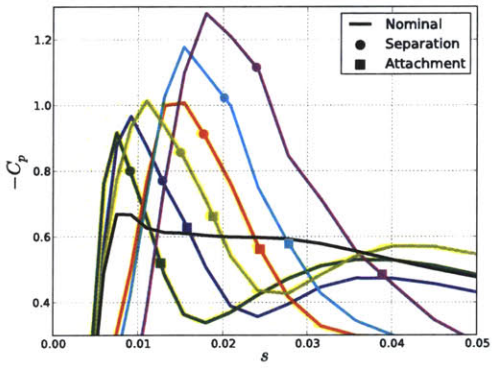

(c) Leading Edge C_p, Uniform Tolerances

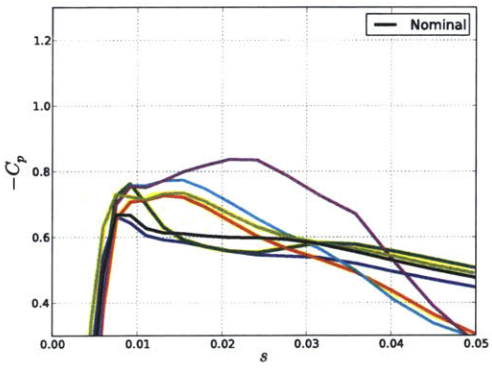

(d) Leading Edge C_p, Optimized Tolerances

Figure 2-25: Leading edges and pressure side pressure coefficient profiles for six manufactured UTRC blades at $\beta_1 = 38.7°$. The left plots correspond to blades with uniform manufacturing tolerances, and the right plots correspond to blades with optimized tolerances.

strength, as quantified by the peak Mach number, corresponds to higher entropy generation. This dependence is nonlinear, resulting in a mean shift in the suction side entropy generation. Before optimizing the tolerances, shock induced separation occurs for 35% of the manufactured blades, which are plotted with colored dots in Figure 2-26. The color indicates the location of separation, normalized by the arclength of the suction side of the blade. Optimizing the tolerances reduces the number of blades with flow separation by 5%, which reduces the mean shift in the suction side losses.

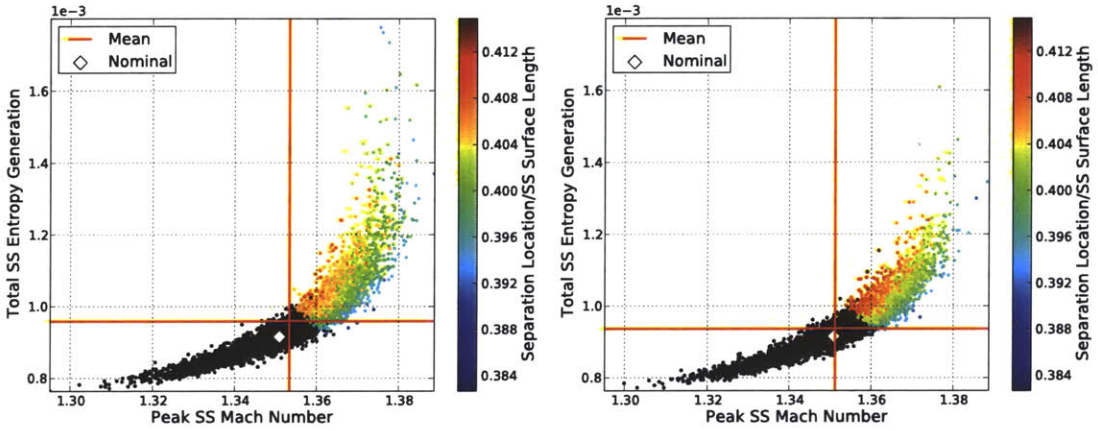

(a) Uniform Tolerances

(b) Optimized Tolerances

Figure 2-26: Entropy generation versus peak suction side Mach number for the manufactured UTRC blades at $\beta_1 = 38.7°$. The black dots correspond to blades with no separation, and the colored dots correspond to blades with separation. The colors indicate the location of separation.

For blades with uniform manufacturing tolerances, a leading edge pressure spike forms on some manufactured blades at the design incidence. Flow transition occurs after these leading edge spikes, as shown at the top left plot of Figure 2-27. The plot at the bottom left of Figure 2-27 shows that earlier transition corresponds to higher entropy generation, which is a result of increased turbulent wetted area. The optimized tolerances shift the mean transition location toward the trailing edge on both sides of the blade. This reduces the mean turbulent wetted area on both sides of the blade, which reduces the mean loss coefficient. The effect of optimizing the tolerances on the suction side transition location is illustrated on the right of Figure 2-27. The mean

transition location moves towards the trailing edge and the mean entropy generation is reduced. Similar shifts in the mean transition location and entropy generation are observed on the pressure side of the blade. The reductions in both the variability and mean shift in the entropy generation are shown in the center plots of Figure 2-24.

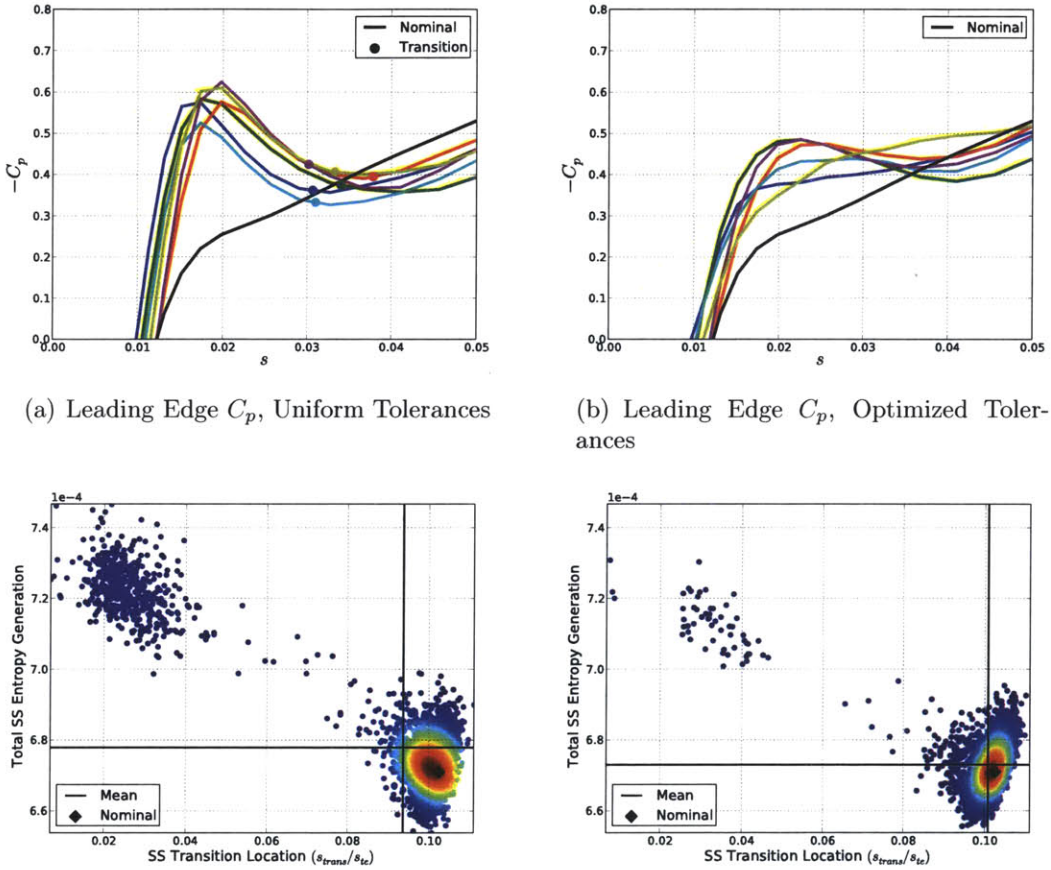

(a) Leading Edge C_p, Uniform Tolerances

(b) Leading Edge C_p, Optimized Tolerances

(c) Manufactured Blades, Uniform Tolerances

(d) Manufactured Blades, Optimized Tolerances

Figure 2-27: Top: suction side pressure coefficient profiles for six manufactured UTRC blades at $\beta_1 = 43.2°$. Bottom: suction side entropy generation versus transition location for all 5,000 manufactured blades. The color indicates probability density.

At positive incidence, optimizing the tolerances has a smaller impact on the mean loss than at negative incidence. The reduced tolerances on the suction side of the blade reduce the fraction of blades with separation from 31% to 29%. This results in a reduction in the mean loss coefficient of only 0.6% at $\beta_1 = 47.7°$ relative to the uniform

tolerances. Since the mean shift in loss at this incidence is smaller than the mean shift at the negative incidence design point ($\beta_1 = 38.7°$), the optimizer focuses on reducing the mean shift at negative incidence resulting from pressure side separation.

To examine the trend in the optimal tolerances as the level of allowed variability decreases, we perform another tolerance optimization where the total variability V_b is constrained to be 96% of the baseline total variability. A comparison between the performance of the UTRC blade with baseline and optimized tolerances is presented in Table 2.4. The mean loss at the positive incidence design point is decreased as a result of reducing the allowable variability. The optimized tolerances, shown in Figure 2-28, further reduce the variability on the suction side of the blade relative to the tolerance scheme shown in Figure 2-22. This reduces the number of blades with regions of separation at the positive incidence design point, lowering the loss.

	Baseline	Optimized
$\mathbb{E}[\bar{\omega}(\beta_1^1)]$	3.35×10^{-2}	3.22×10^{-2}
$\mathbb{E}[\bar{\omega}(\beta_1^2)]$	2.27×10^{-2}	2.25×10^{-2}
$\mathbb{E}[\bar{\omega}(\beta_1^3)]$	2.84×10^{-2}	2.80×10^{-2}
$\sum w_i \mathbb{E}[\bar{\omega}(\beta_1^i)]$	2.68×10^{-2}	2.63×10^{-2}

Table 2.4: Comparison of the mean loss for the UTRC blade with baseline and optimized tolerances with 96% of the baseline variability.

2.4.2 SC10 Rotor

For the SC10 rotor blade, $N_p = 3$ design points are selected to fall at $\beta_1 = 48.5°$, 53.5°, and 58.5° and the loss weight vector is again chosen to be $\mathbf{w} = \{1/4,\ 1/2,\ 1/4\}$. The total variability is constrained to be 98% of the baseline value, and the standard deviation is constrained to be below the baseline value of $\sigma/c = 6.0 \times 10^{-4}$ at all points on the blade surface. $N = 500$ Monte Carlo samples were used to estimate the mean loss during the optimization, and $N = 5,000$ samples were used to estimate the performance statistics for the optimized design.

The tolerance optimization converged after 23 SQP iterations and required 59

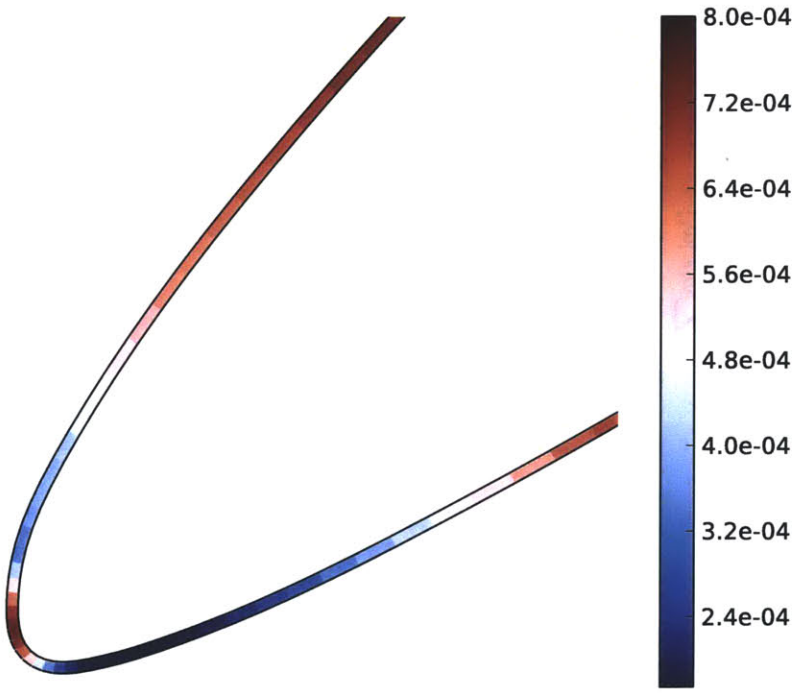

Figure 2-28: Optimal standard deviation for the UTRC blade with 96% of the baseline variability. The lower surface is the pressure side, and the upper surface is the suction side.

evaluations of the mean loss coefficient, for a total of 29,500 MISES flow solutions. The convergence history of the mean loss is shown in Figure 2-29. The optimal distribution of the standard deviation, plotted in Figure 2-30, follows a "double bow-tie" pattern. Table 2.5 summarizes the reduction in the mean loss at the design points as a result of optimizing the tolerances. The tolerance optimization process reduces the mean shift in the loss coefficient over the entire incidence range considered for the SC10 blade, as illustrated in Figure 2-31, with an average reduction of 78%.

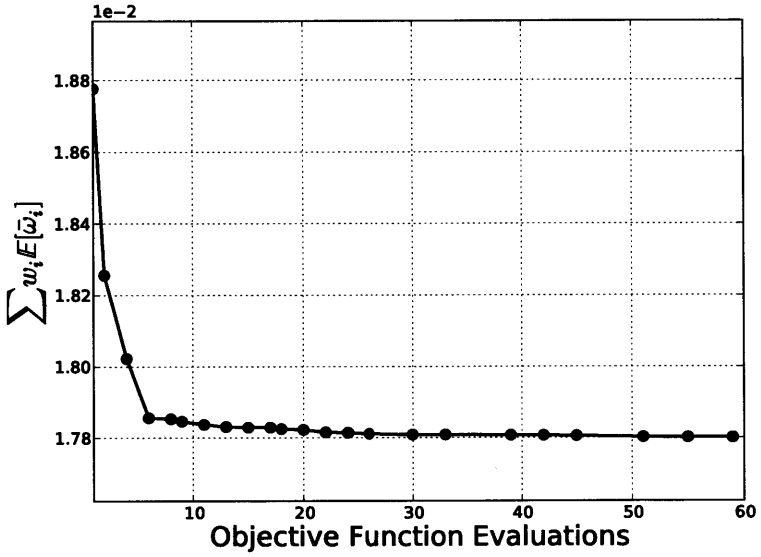

Figure 2-29: Convergence history for the tolerance optimization of the SC10 blade. The dots indicate SQP iterations.

	Baseline	Optimized
$\mathbb{E}[\bar{\omega}(\beta_1^1)]$	2.19×10^{-2}	2.04×10^{-2}
$\mathbb{E}[\bar{\omega}(\beta_1^2)]$	1.53×10^{-2}	1.52×10^{-2}
$\mathbb{E}[\bar{\omega}(\beta_1^3)]$	2.25×10^{-2}	2.04×10^{-2}
$\sum w_i \mathbb{E}[\bar{\omega}(\beta_1^i)]$	1.88×10^{-2}	1.78×10^{-2}

Table 2.5: Comparison of the mean loss for the SC10 blade with baseline and optimized tolerances with 98% of the baseline variability.

At the negative incidence design point, the flow separates on the pressure side of the nominal blade due to an adverse pressure gradient. Pressure side flow separation

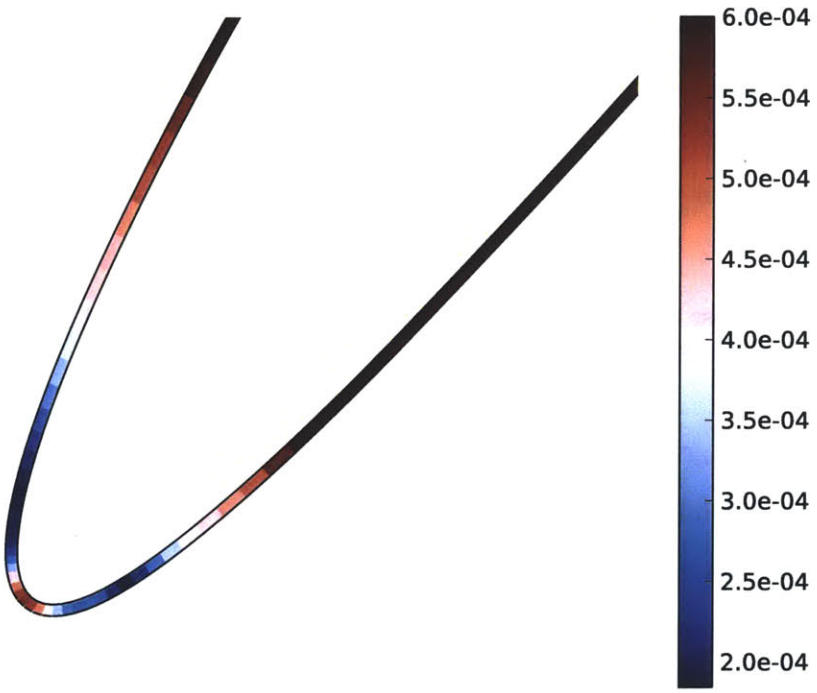

Figure 2-30: Optimal standard deviation for the SC10 blade with 98% of the baseline variability. The lower surface is the pressure side, and the upper surface is the suction side.

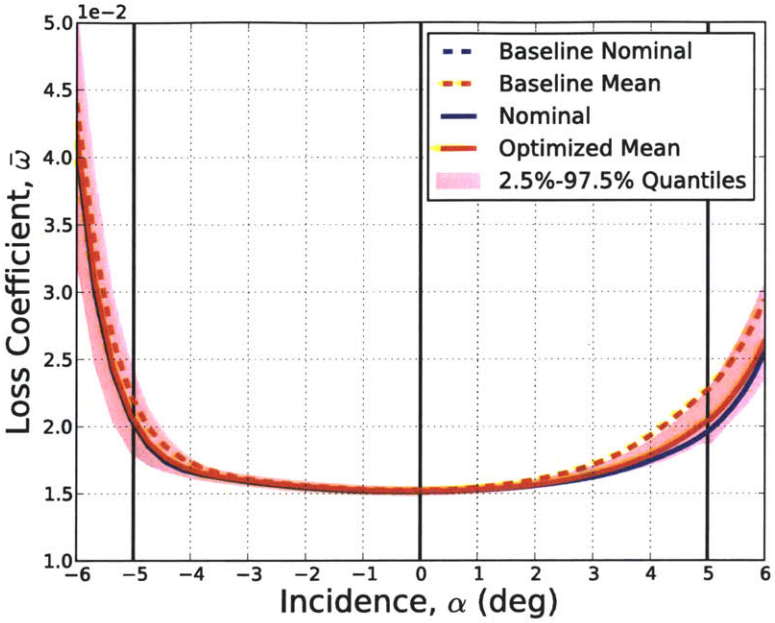

Figure 2-31: Loss coefficient versus incidence angle for the SC10 rotor with optimized tolerances with 98% of the baseline variability.

occurs on 93% of the manufactured blades with uniform manufacturing tolerances. The optimized tolerances result in pressure side flow separation for 2% more of the blades. However, the optimized tolerances reduce the length of the separation bubbles. The effect of reducing the pressure side manufacturing tolerances is illustrated in Figure 2-33. Reducing the mean separation bubble length reduces the mean entropy generation, as shown in Figure 2-34. The top plots in Figure 2-32 show that the optimized tolerances also reduce the variability in the pressure side entropy generation.

At the design incidence, optimizing the tolerances has the same effect on the SC10 blade as on the UTRC blade. The mean transition location moves towards the trailing edge on both sides of the blade, reducing the mean shift and variability in the entropy generation, as shown in the middle plots of Figure 2-32.

At the positive incidence design point, flow separation occurs on 50% of the manufactured blades with uniform tolerances. For 10% of the manufactured blades, separation occurs at a shock that forms on the suction side of the blade, while separation

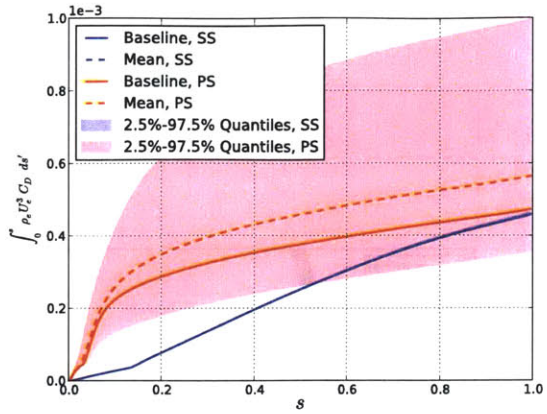

(a) $\beta_1 = 48.5°$, Uniform Tolerances

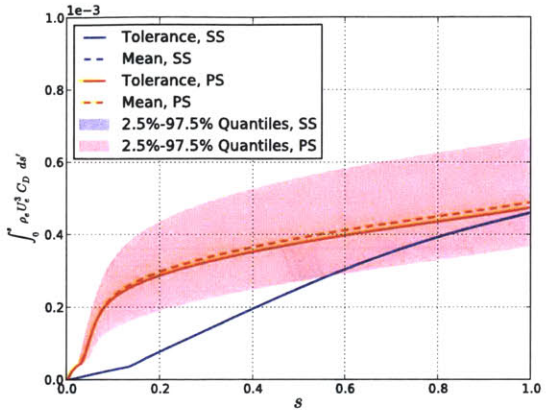

(b) $\beta_1 = 48.5°$, Optimized Tolerances

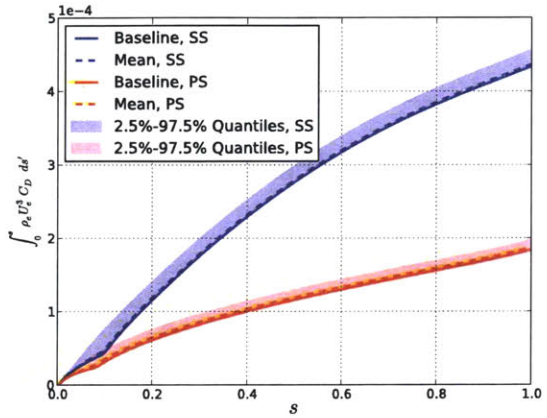

(c) $\beta_1 = 53.5°$, Uniform Tolerances

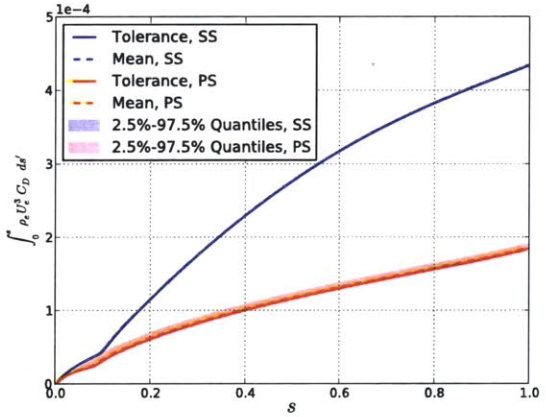

(d) $\beta_1 = 53.5°$, Optimized Tolerances

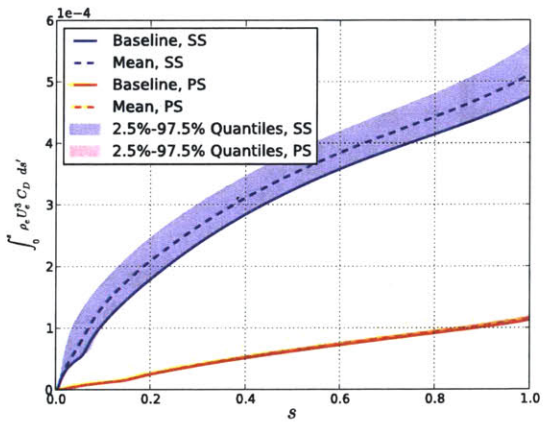

(e) $\beta_1 = 58.5°$, Uniform Tolerances

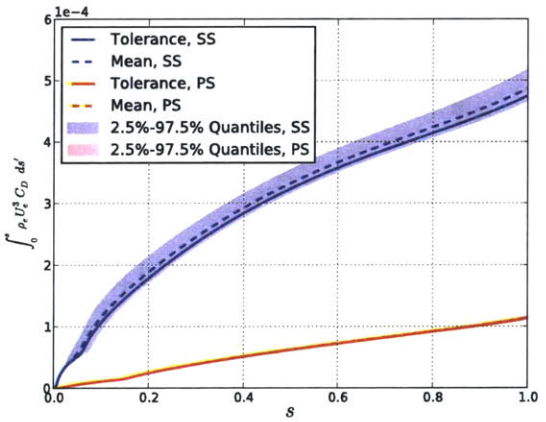

(f) $\beta_1 = 58.5°$, Optimized Tolerances

Figure 2-32: Boundary layer entropy generation rate for the SC10 blade with uniform and optimized tolerances with 98% of the baseline variability. Solid lines indicate the nominal, dashed lines indicate the mean. The pressure side (PS) is plotted in red and the suction side (SS) is plotted in blue.

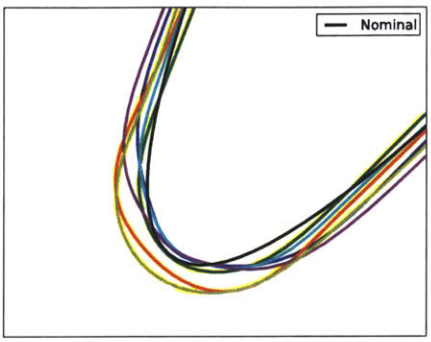

(a) Manufactured Blades, Uniform Tolerances

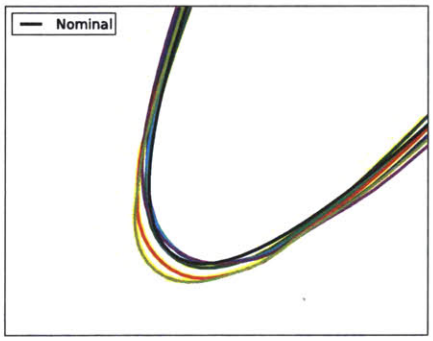

(b) Manufactured Blades, Optimized Tolerances

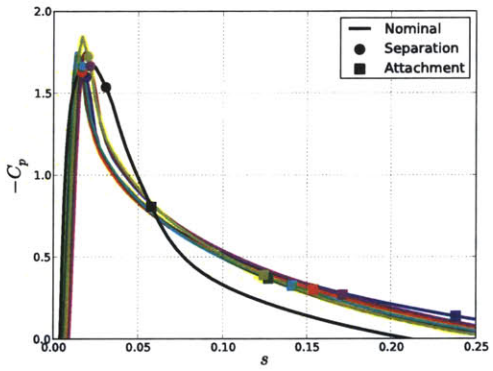

(c) Leading Edge C_p, Uniform Tolerances

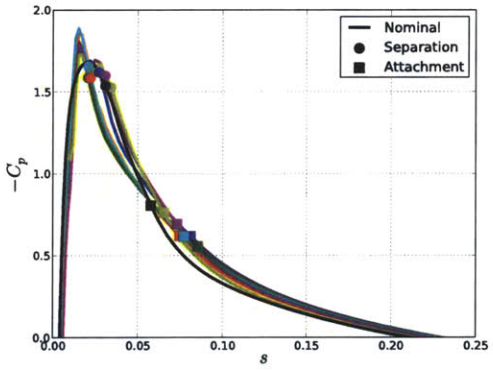

(d) Leading Edge C_p, Optimized Tolerances

Figure 2-33: Leading edges and pressure side pressure coefficient profiles for six manufactured SC10 blades at $\beta_1 = 48.5°$. The left plots correspond to blades with uniform manufacturing tolerances, and the right plots correspond to blades with optimized tolerances.

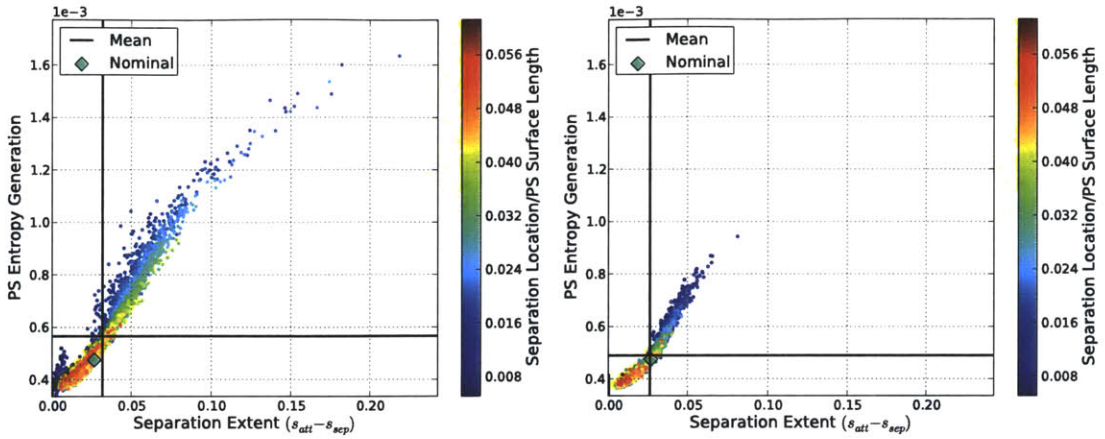

(a) Uniform Tolerances

(b) Optimized Tolerances

Figure 2-34: Comparison between separation bubble length and entropy generation on the pressure side of the SC10 blade at $\beta_1 = 48.5°$ with uniform and optimized tolerances with 98% of the baseline variability (colors indicate separation location).

occurs on the aft 10% of the blade for the other 40% of the blades. The left plot in Figure 2-35 shows that the entropy generation increases as the length of the separation bubble increases. With optimized tolerances, flow separation occurs on 10% of the blades. The reduction in flow separation, and the consequent reduction in entropy generation is illustrated in the right plot of Figure 2-35.

We also perform an optimization where the total variability V_b is constrained to be 96% of the baseline total variability. A comparison between the performance of the SC10 blade with uniform and optimized tolerances is presented in Table 2.6. The optimized tolerances, shown in Figure 2-36, further reduce the variability on the suction side of the blade from the tolerance scheme shown in Figure 2-30. Suction side flow separation does not occur at the positive incidence design point for any of the blades with these manufacturing tolerances.

2.5 Chapter Summary

In this chapter, we have presented a probabilistic, gradient-based optimization framework for designing compressor blade manufacturing tolerances. A novel "double bow-

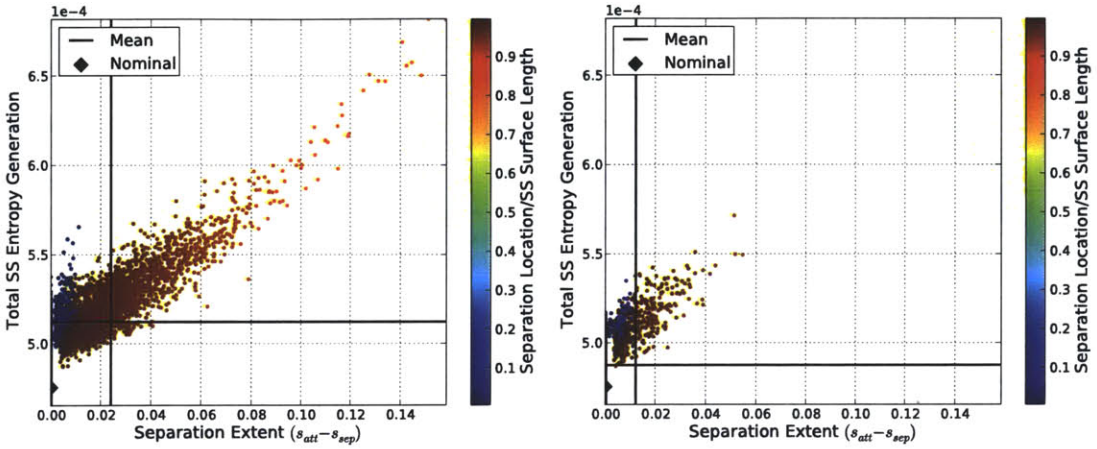

(a) Uniform Tolerances

(b) Optimized Tolerances

Figure 2-35: Comparison between separation bubble length and entropy generation on the pressure side of the SC10 blade at $\beta_1 = 58.5°$ with uniform and optimized tolerances with 98% of the baseline variability (colors indicate separation location).

	Baseline	Optimized
$\mathbb{E}[\bar{\omega}(\beta_1^1)]$	2.19×10^{-2}	2.02×10^{-2}
$\mathbb{E}[\bar{\omega}(\beta_1^2)]$	1.53×10^{-2}	1.52×10^{-2}
$\mathbb{E}[\bar{\omega}(\beta_1^3)]$	2.25×10^{-2}	1.98×10^{-2}
$\sum w_i \mathbb{E}[\bar{\omega}(\beta_1^i)]$	1.88×10^{-2}	1.76×10^{-2}

Table 2.6: Comparison of the mean loss for the SC10 blade with baseline and optimized tolerances with 96% of the baseline variability.

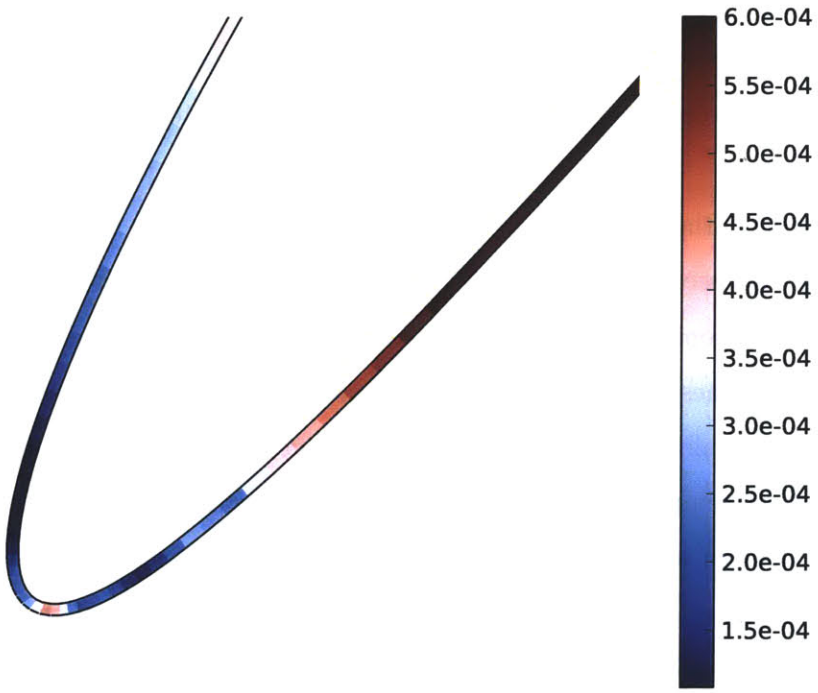

Figure 2-36: Optimal standard deviation for the SC10 blade with 96% of the baseline variability. The lower surface is the pressure side, and the upper surface is the suction side.

tie" tolerance scheme was found to be optimal for two subsonic blades. At the positive and negative incidence design points, flow separation was the dominant mechanism that led to an increase in the mean loss for manufactured compressor blades. Reducing variability near the leading edge reduced the extent of flow separation occurring at the leading edge, as well as at shocks and at the trailing edge. At the design incidence, the optimal tolerance scheme moves the mean transition location towards the trailing edge on both sides of the blade. By reducing the total variability by 2%, tolerance optimization reduced the average mean shift in loss by 49% for the UTRC exit guide vane and 78% for the SC10 rotor blade. The optimal distribution of $\sigma(s)$ differed for these two geometries, illustrating that the optimal tolerance scheme is geometry dependent.

In practice, the framework presented in this chapter can be used to select manufacturing processes that achieve the required process spread at every location on the blade, and to construct tolerance bands for rejecting or reworking blades. Our approach determines the optimal process spread $\sigma(s)$, which varies continuously around the blade. In reality, only finitely many manufacturing processes are available, so $\sigma(s)$ changes discontinuously at the point where one manufacturing process is replaced by another. Further work is required to determine how to translate the continuous process spread to a set of manufacturing processes in different regions of the blade.

Tolerance bands can also be constructed from the process spread by choosing constant factors k_i and k_o corresponding to inner and outer tolerance bands. Blades whose surface falls within the inner tolerance band $x_d(s) - k_i\sigma(s)\hat{n}(s)$ are rejected, and blades whose surface falls outside the outer tolerance band $x_d(s) + k_o\sigma(s)\hat{n}(s)$ are reworked. Rejecting and reworking blades that fall outside the tolerance bands truncates the distribution of the manufactured blade variability, as opposed to scaling the distribution according to the process spread. Future work should recommend how to select k_i and k_o, and compare the mean performance of blades toleranced according to bands constructed from $\sigma(s)$ to the mean performance of blades with scaled process spread.

Chapter 3

Compressor Blade Geometry and Tolerance Design

In this chapter, we integrate geometry optimization into the tolerance optimization process. We illustrate that the interdependence of the optimal blade geometry and optimal manufacturing tolerances determines whether the geometry and tolerances should optimized simultaneously. Section 3.1 describes the optimization problems that are solved to obtain the optimal blade geometry, and Section 3.2 formulates the simultaneous geometry and tolerance optimization problem. In Section 3.3, conditions are provided to determine whether the tolerances should be optimized simultaneously with the blade geometry. The geometry and tolerances of the blades considered in Chapter 2 are optimized in Section 3.4.

3.1 Formulations of Compressor Blade Geometry Optimization

3.1.1 Single-point Deterministic Design

Deterministic optimization minimizes the loss coefficient of the design intent geometry. The inflow angle is held fixed, and the flow turning is constrained to its baseline value,

denoted as $\Delta\beta_b$. The deterministic optimal blade geometry is determined by solving the following optimization problem:

$$\begin{aligned} \min_{\mathbf{d}\in\mathbf{D}} \quad & \bar{\omega}(\mathbf{d}) \\ \text{s.t.} \quad & \Delta\beta(\mathbf{d}) = \Delta\beta_b. \end{aligned}$$

Here $\mathbf{d} \in \mathbb{R}^{N_d}$ is a vector parameterizing the design intent geometry of the blade $x_d(s)$, and $\mathbf{D} \subset \mathbb{R}^{N_d}$ is the design space which takes into account any geometric constraints placed on the blade profile.

3.1.2 Single-point Robust Design

Robust design optimization minimizes the mean loss coefficient. Replacing the nominal values of the loss coefficient and flow turning with their mean values gives the single-point robust design optimization statement:

$$\begin{aligned} \min_{\mathbf{d}\in\mathbf{D}} \quad & \mathbb{E}[\bar{\omega}(\mathbf{d})] \\ \text{s.t.} \quad & \mathbb{E}[\Delta\beta(\mathbf{d})] = \Delta\beta_b. \end{aligned}$$

This optimization statement is identical to that used in [27] to perform robust optimization of rotor blade sections.

3.1.3 Multi-point Deterministic Design

For fixed inflow Mach number, a design point is defined by the incidence angle. Performing single-point optimization at the nominal incidence can produce geometries that reduce the loss near the nominal incidence angle, but increase the loss at other incidences. We therefore use the multi-point design strategy introduced in Chapter 2 to reduce the loss over a range of incidence angles. The weighted loss is minimized,

and the turning at the nominal incidence is constrained to its baseline value:

$$\begin{aligned} \min_{\mathbf{d}\in\mathbf{D}} \quad & \sum_{i=1}^{N_p} w_i \bar{\omega}(\mathbf{d}, \beta_1^i) \\ \text{s.t.} \quad & \Delta\beta(\mathbf{d}, \beta_1^{des}) = \Delta\beta_b. \end{aligned}$$

3.1.4 Multi-point Robust Design

For the blade geometries considered in Chapter 2, the mean shift in loss at the nominal incidence is small relative to the loss of the design intent blade, and grows as the incidence is either increased or decreased. This suggests that performing robust multi-point optimization will be beneficial, since the multi-point objective function incorporates design conditions where the shift in mean performance is an order of magnitude larger than the mean shift at the design incidence. This motivates the following robust multi-point formulation:

$$\begin{aligned} \min_{\mathbf{d}\in\mathbf{D}} \quad & \sum_{i=1}^{N_p} w_i \mathbb{E}[\bar{\omega}(\mathbf{d}, \beta_1^i; \theta)] \\ \text{s.t.} \quad & \mathbb{E}[\Delta\beta(\mathbf{d}, \beta_1^{des}; \theta)] = \Delta\beta_b \end{aligned}$$

Multi-point robust optimal designs are robust with respect to manufacturing variations and variations in the flow incidence.

3.2 Simultaneous Geometry and Tolerance Design

The proposed tolerance optimization framework can be incorporated to perform simultaneous optimization of both the nominal blade geometry and manufacturing tolerances using any of the formulations presented in the previous section. Reducing the level of geometric variability tends to improve the mean performance, but increases the cost of manufacturing the blades. Figure 3-1 illustrates the trade-off between geometric variability, quantified by $V(\boldsymbol{\sigma})$, and mean loss. The gray region represents

all feasible designs, and the solid black line shows the set of Pareto optimal designs. A design is Pareto optimal if the mean loss cannot be reduced without relaxing the manufacturing tolerances (increasing V) and the tolerances cannot be relaxed without increasing the mean loss. Both the deterministic and robust optimal designs fall on this Pareto front: in the absence of geometric variability ($V = 0$), optimizing the geometry produces the deterministic optimal design $\mathbf{d}^*_{det}$, and optimizing the geometry in the presence of manufacturing variations, e.g. with standard deviation σ_{max}, results in the robust optimal design $\mathbf{d}^*_{rob}$.

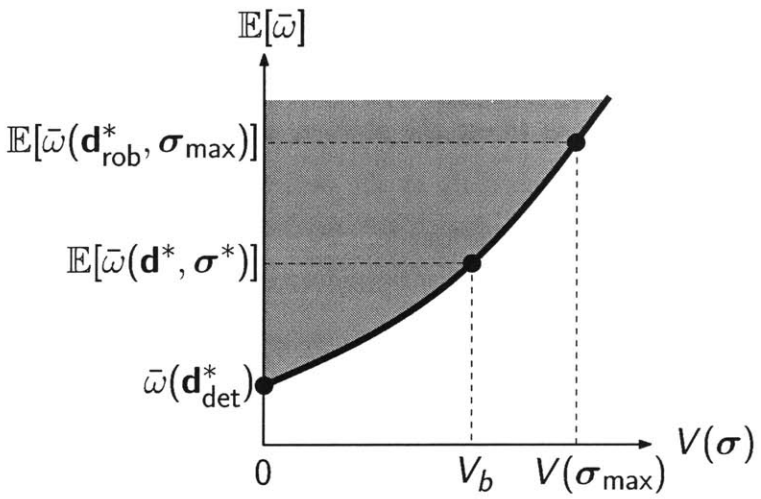

Figure 3-1: Pareto front illustrating the trade-off between performance and variability.

Additional points that lie on the Pareto front can be found by solving an optimization problem. For a given level of variability V_b, both the tolerances and design intent geometry are optimized to minimize the mean loss coefficient. The optimization problem used to simultaneously optimize the geometry and tolerances is summarized below:

$$
\begin{aligned}
(\mathbf{d}^*, \boldsymbol{\sigma}^*) = \quad & \underset{\mathbf{d},\boldsymbol{\sigma}}{\arg\min} \quad \mathbb{E}[\bar{\omega}(\mathbf{d}, \boldsymbol{\sigma})] \\
& \text{s.t.} \quad \mathbb{E}[\Delta\beta(\mathbf{d}; \theta)] = \Delta\beta_b \\
& \qquad\quad V(\boldsymbol{\sigma}) = V_b \\
& \qquad\quad \sigma(s) \leq \sigma_{max}.
\end{aligned}
$$

The multi-point design strategy replaces the objective and constraints with the weighted mean loss and mean turning.

The geometry optimization and geometry/tolerance optimization problems are solved using a gradient-based approach. For the robust optimizations, the SAA method is applied by replacing the mean loss and mean turning by their Monte Carlo estimates. The SQP method is used to solve the resulting nonlinear programs, and the gradients with respect to all design variables are computed using the finite difference method. The geometry/tolerance optimization process is represented diagrammatically in Figure 3-2.

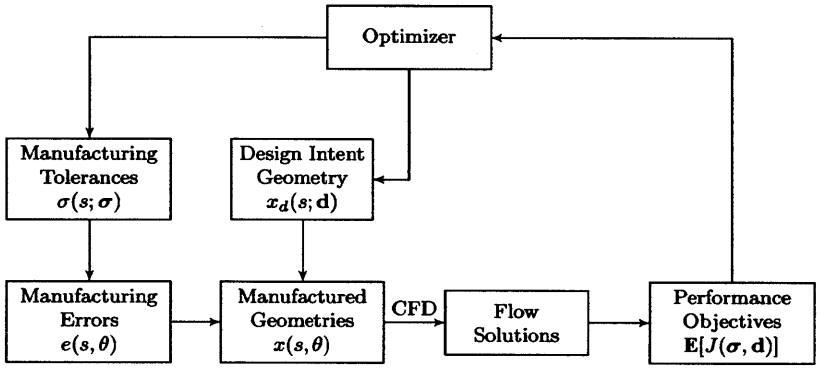

Figure 3-2: Block diagram illustrating the geometry and tolerance optimization framework.

3.3 Simultaneous vs. Sequential Geometry and Tolerance Design

There are two alternative approaches for optimizing compressor blade geometry and manufacturing tolerances: the simultaneous design approach, in which the nominal geometry and manufacturing tolerances are optimized together, or a sequential design approach, in which the nominal geometry is optimized with presumed tolerances, and the tolerances are then optimized with the geometry fixed.

The results of Chapter 2 show that the optimal manufacturing tolerances depend on the blade geometry. The optimal, minimum mean loss geometry may depend on the manufacturing tolerances, in which case the deterministic optimal geometry and robust optimal geometries differ. Simultaneous optimization is required in this case, since optimizing the nominal geometry first will result in a sub-optimal design when the level of variability is changed by the tolerance optimization step. If the optimal, minimum mean loss geometry does not depend on the manufacturing tolerances, the geometry can be first optimized deterministically.

The sensitivity of the optimal geometry to the level of noise depends on the properties of the objective function at the deterministic optimal solution. We analyze the case where the performance is determined by a single geometric design variable d, and assume the geometry is subject to additive Gaussian noise with zero mean and variance $v := \sigma^2$, so that the manufactured design is given by $d_m = d + e$, $e \sim \mathcal{N}(0, v)$. The loss coefficient is assumed to be a locally convex function of d, which is true for some region around the deterministic optimal geometry d^*, which corresponds $v = 0$. The sensitivity of the optimal geometry with respect to the variance can be derived using perturbation analysis [24]. Expanding the stationarity condition around the deterministic optimal solution $(d, v) = (d^*, 0)$, we have

$$0 = \cancelto{0}{\left.\frac{\partial F}{\partial d}\right|_0} + \left.\frac{\partial^2 F}{\partial d^2}\right|_0 \delta d + \left.\frac{\partial^2 F}{\partial d \partial v}\right|_0 \delta v,$$

where the objective function $F = \mathbb{E}[\bar{\omega}(d; v)]$ is the mean loss coefficient. This implies that

$$\frac{\partial d^*}{\partial v} = -\left[\frac{\partial^2 F}{\partial d^2}\right]^{-1} \frac{\partial^2 F}{\partial d \partial v}.$$

The second term can be expanded for small v by introducing the noise variable $\xi \sim$

$\mathcal{N}(0,1)$:

$$\begin{aligned}
\frac{\partial^2 F}{\partial d \partial v} &= \mathbb{E}\left[\frac{\partial}{\partial v}\left(\frac{\partial \bar{\omega}}{\partial d}(d^* + \xi\sqrt{v})\right)\right] \\
&= \mathbb{E}\left[\left(\frac{\partial^2 \bar{\omega}}{\partial d^2}(d^* + \xi\sqrt{v})\right)\frac{\xi}{2\sqrt{v}}\right] \\
&= \mathbb{E}\left[\left.\frac{\partial^2 \bar{\omega}}{\partial d^2}\right|_0 \frac{\xi}{2\sqrt{v}} + \left.\frac{\partial^3 \bar{\omega}}{\partial d^3}\right|_0 \frac{\xi^2}{2} + \left.\frac{\partial^4 \bar{\omega}}{\partial d^4}\right|_0 \frac{\xi^3\sqrt{v}}{4} + O(v)\right] \\
&= \frac{1}{2}\left.\frac{\partial^3 \bar{\omega}}{\partial d^3}\right|_0 + O(v).
\end{aligned}$$

A series expansion for the optimal geometry is

$$d^*(v) = d^*(0) + \left.\frac{\partial d^*}{\partial v}\right|_0 v + O(v^2).$$

Plugging in,

$$d^*(v) = d^*(0) - \frac{1}{2}\left[\left.\frac{\partial^2 \bar{\omega}}{\partial d^2}\right|_0\right]^{-1}\left.\frac{\partial^3 \bar{\omega}}{\partial d^3}\right|_0 v + O(v^2). \tag{3.1}$$

In multiple dimensions with uncorrelated noise factors, this generalizes to

$$\mathbf{d}^*(\mathbf{v}) = \mathbf{d}^*(0) - \frac{1}{2}H^{-1}T\mathbf{v} + O(\mathbf{v}^2),$$

where $\mathbf{v} = [\sigma_1^2 \ldots \sigma_{N_d}^2]^\intercal$, H is the Hessian matrix:

$$H_{ij} = \left.\frac{\partial^2 \bar{\omega}}{\partial d_i \partial d_j}\right|_0,$$

and the third derivative matrix T is given by

$$T_{ij} = \left.\frac{\partial^3 \bar{\omega}}{\partial d_i \partial d_j^2}\right|_0.$$

When the noise factors are correlated with correlation matrix R, the expansion for the

optimal design is

$$d_i^*(\mathbf{v}) = d_i^*(0) + \frac{1}{2}\sum_j \sum_k \frac{\partial^2 d_i^*}{\partial \sigma_j \partial \sigma_k}\sigma_j \sigma_k + O(\mathbf{v}^2),$$

where

$$\frac{\partial^2 d_i^*}{\partial \sigma_j \partial \sigma_k} = -\sum_m H_{im}^{-1} \left.\frac{\partial^3 \bar{\omega}}{\partial d_m \partial d_j \partial d_k}\right|_0 R_{jk}.$$

Thus, to first order, the change in the optimal design is proportional to the third derivative of the loss function multiplied by the variance of the noise factors, normalized by the Hessian matrix. The third derivative quantifies the asymmetry of the loss function. The above derivation shows that if the loss function is locally symmetric at the deterministic optimal design, the optimal geometry is not affected by symmetrically distributed variability. If the loss function increases more slowly in a particular design direction near the deterministic optimum, the robust optimum will move in the direction that the loss increases more slowly as the level of noise is increased.

Figure 3-3 shows two convex loss functions, one symmetric and one asymmetric. The blue curves show the loss function in the absence of variability, and the green and red curves show the mean loss function for increasing levels of normally distributed variability in the design variable d. The minimum loss geometry, indicated by the solid dot, does not change as the noise level is increased for the symmetric loss function on the left. For the asymmetric loss function on the right, the optimal geometry moves in the direction that the loss increases more slowly. The dependence of the optimal solution on the noise level for the asymmetric function is plotted in Figure 3-4, along with the linear extrapolation from the deterministic optimal computed using Equation (3.1).

To first order, the change in the optimal geometry is given by $\Delta d^* := d^*(\sigma) - d^*(0) = S_{d^*}\sigma$, where the non-dimensional sensitivity S_{d^*} is given by

$$S_{d^*} = -\frac{1}{2}\left[\left.\frac{\partial^2 \bar{\omega}}{\partial d^2}\right|_0\right]^{-1} \left.\frac{\partial^3 \bar{\omega}}{\partial d^3}\right|_0 \sigma.$$

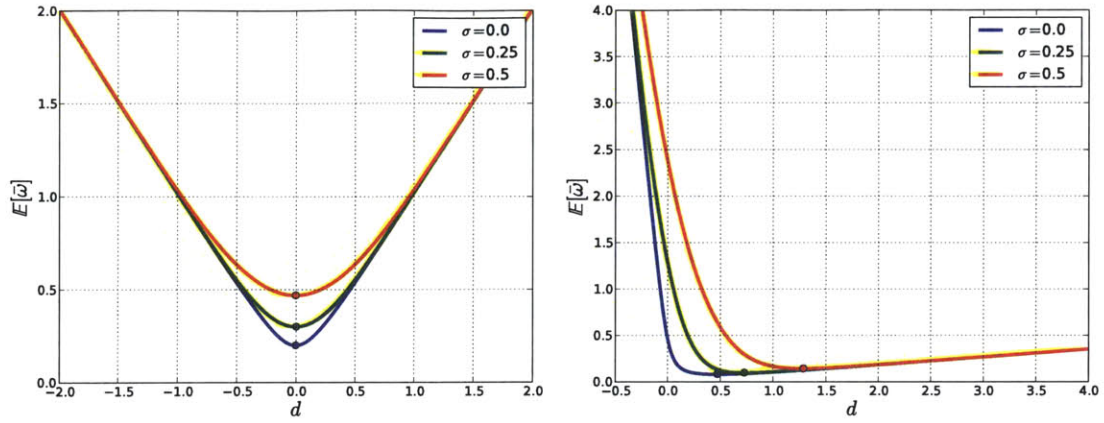

Figure 3-3: Symmetric (a) and asymmetric (b) loss functions with increasing levels of noise. The dot indicates the location of the optimum.

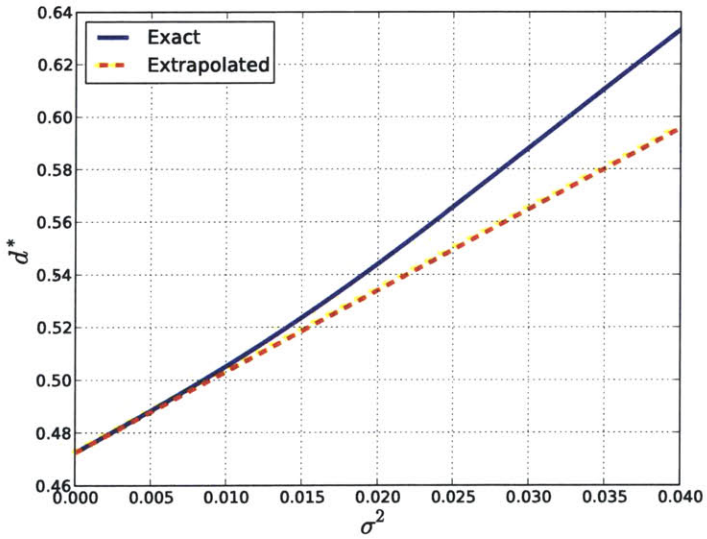

Figure 3-4: Variation of the optimal solution with noise level for the asymmetric loss function in the right of Figure 3-3.

If $|S_{d^*}| \gg 1$, then $|\Delta d^*| \gg \sigma$, and the robust optimal geometry differs from the deterministic optimal geometry by an amount larger than the standard deviation of the manufacturing error. Otherwise, the difference between the robust optimal and deterministic optimal geometries is on the order of the manufacturing error, obviating the need to perform robust design. For the function on the left of Figure 3-4, $S_{d^*} = 0$, indicating that the optimal design is insensitive to variability. For the function on the right, $S_{d^*} = 3.08\sigma$, indicating that the location of the optimal design moves to the right as the level of variability is increased, and that for $\sigma > 1/3.08 = 0.325$, the change in the design is of the same order of magnitude or larger than the standard deviation.

The primary limitation of this sensitivity index is that it is only accurate when higher order terms, i.e. terms that are $O(v^2)$ in Equation (3.1), can be ignored. The results presented in Chapter 2 show that manufacturing variations lead to increases in loss as a result of flow separation or changes in the transition location. When these flow features appear, the loss increases nearly discontinuously, and the higher order terms dominate in Equation (3.1). In this case, the sensitivity index does not provide an accurate estimate of the change in the optimal design when manufacturing noise is introduced. However, the conclusions regarding the asymmetry of the loss still apply: if the mean shift is uniform for geometries in a neighborhood of designs near the deterministic optimal geometry, then the optimal geometry is insensitive to the level of variability. Otherwise, the optimal geometry moves in a direction of the design space that decreases the mean loss. This asymmetry occurs when the dominant loss mechanism switches for some manufactured blades. For example, Goodhand et al. showed that manufacturing variations result in flow separation for some manufactured blades when the leading edge radius of curvature is reduced. The optimal design moved to avoid this switch in the dominant loss mechanism by increasing the leading edge radius of curvature, preventing flow separation from occurring on the manufactured blades [33]. If the switch in dominant loss mechanism occurs for all manufactured blades, we can conclude that the loss function is symmetric at the deterministic optimal

design, and the deterministic and robust designs will be the same.

3.4 Application to Compressor Blade Geometry and Tolerance Optimization

3.4.1 Design Intent Geometry Parameterization

The design intent surface geometry is constructed by adding a set of shape functions $T'_k(s)$, $k = 1, ..., N_g$ to the baseline geometry. Each shape function moves the baseline geometry $x_b(s)$ in the surface normal direction, so that the coordinates of the design intent geometry $x(s)$ are given by

$$x(s) = x_b(s) + \hat{n}(s) \sum_{k=1}^{N_g} d_k T'_k(s),$$

where the d_k are the amplitudes of the shape functions and $-1 \leq s \leq 1$ is the arc length coordinate defined in Chapter 2. To allow for changes in the blade stagger angle, a rotation angle design variable is included. The design vector $\mathbf{d} \in \mathbb{R}^{N_d}$ thus consists of the set of shape function amplitudes d_k, $k = 1, ..., N_g$ and the rotation angle.

The shape functions are chosen to be modified Chebyshev polynomials of the first type:

$$T'_k(s) = \frac{1}{k+1} \begin{cases} 1 - 2s - \cos[(k+1)\arccos(1-2s)], & k \text{ even} \\ 1 - \cos[(k+1)\arccos(1-2s)], & k \text{ odd} \end{cases}$$

The first five modified Chebyshev modes are plotted in Figure 3-5. Figure 3-5 shows that the modified Chebyshev polynomials become more oscillatory as k increases. To prevent the appearance of localized features in the geometry, it is important to use a small number of design modes. This prevents the optimizer from exploiting the flow at the smallest significant physical scales and producing geometries that perform poorly away from the given set of design points [17]. For all optimizations, $N_g = 5$

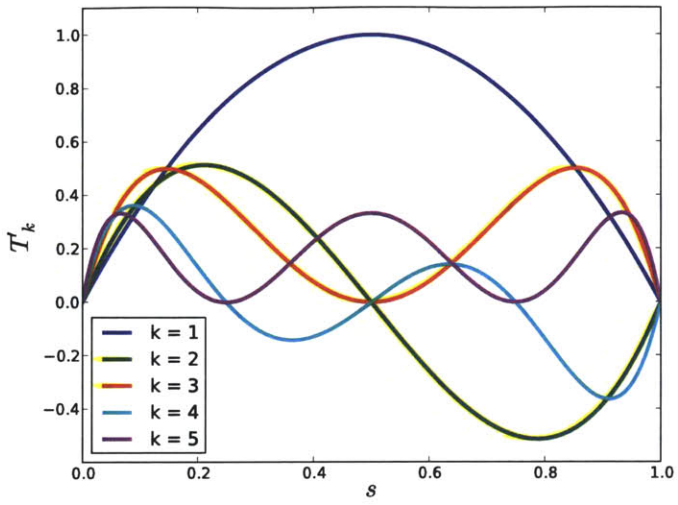

Figure 3-5: Modified Chebyshev polynomials $T'_k(s)$, $k = 1, ..., 5$.

Chebyshev modes are used to parameterize the surface geometry. The blade solidity is held constant to keep the blade loading constant. The cross-sectional area of the blade, which is proportional to its tensile stiffness, is also constrained during optimization. To constrain the cross-sectional area to be equal to the baseline thickness, equal and opposite perturbations are applied to the pressure and suction sides of the blade.

3.4.2 UTRC Fan Exit Guide Vane

3.4.2.1 Single-Point Optimization

The design point is placed at the design intent inflow angle of $\beta_1^{des} = 43.2°$. Sequential optimizations of the geometry and tolerances were performed using both the deterministic and robust geometry design approaches. A simultaneous optimization of the geometry and tolerances was also performed. The optimizations were terminated when the mean loss converged within an absolute tolerance of 10^{-5}. $N = 500$ Monte Carlo samples were used to approximate the mean loss and mean turning, and the total variability was constrained to be 98% of the baseline value. The standard deviation was constrained to be less than the baseline value $\sigma_b/c = 8.0 \times 10^{-4}$ everywhere on

the blade. Table 3.1 summarizes the number of SQP iterations, objective evaluations, and MISES flow calculations required to perform each optimization. The number of MISES flow calculations indicates that the robust geometry design approach is orders of magnitude more computationally expensive than the deterministic geometry design approach. The convergence histories of the optimizations are compared in Figure 3-6.

	Det. Geometry	Det. Tolerance	Robust Geometry	Robust Tolerance	Simultaneous
N	-	500	500	500	500
# SQP iter	14	35	10	24	41
# Obj. evals	18	45	16	39	86
# MISES runs	18	22,500	8,000	19,500	43,000

Table 3.1: Number of Monte Carlo samples, SQP iterations, objective/constraint evaluations, and MISES flow calculations for the single-point optimizations of the UTRC blade.

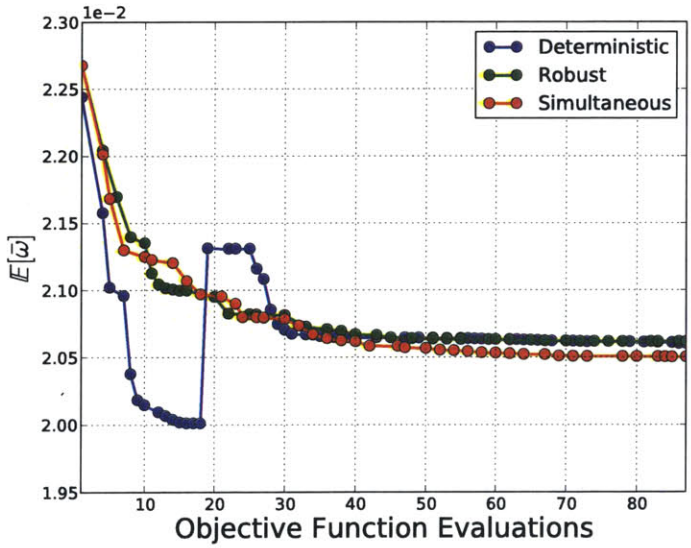

Figure 3-6: Convergence history for the single-point optimizations of the UTRC blade. The dots indicate SQP iterations.

Table 3.2 summarizes the performance of the single-point optimized designs. The second row gives the mean loss calculated using uniform manufacturing variability ($\sigma_b/c = 8.0 \times 10^{-4}$), and the last row gives the mean loss calculated using optimized

tolerances. In the absence of variability, the deterministic optimum has the lowest loss coefficient, 11% lower than the loss of the baseline design. The robust geometry optimization reduces the mean loss by 8%, and has the lowest mean loss at the baseline level of manufacturing variability. The simultaneous optimization has lower mean loss than the other designs with optimized tolerances, and reduces the mean loss by 11% relative to the baseline geometry with uniform tolerances.

	Baseline	Deterministic	Robust	Simultaneous
$\bar{\omega}$	2.24×10^{-2}	2.00×10^{-2}	2.06×10^{-2}	2.03×10^{-2}
$\mathbb{E}[\bar{\omega}(\boldsymbol{\sigma}_b)]$	2.27×10^{-2}	2.14×10^{-2}	2.09×10^{-2}	2.10×10^{-2}
$\mathbb{E}[\bar{\omega}(\boldsymbol{\sigma}^*)]$	2.25×10^{-2}	2.06×10^{-2}	2.06×10^{-2}	2.05×10^{-2}

Table 3.2: Performance comparison of the baseline UTRC, single-point deterministic optimal, single-point robust optimal, and single-point simultaneous optimal designs.

The optimal blade geometries are compared in Figure 3-7. In the lower plot, all blades are rotated to the same stagger angle to facilitate comparison of the blade camber. Figure 3-8 compares the pressure coefficient profiles for the three blades in the absence of geometric variability. The deterministic optimization eliminates the shock by reducing the camber of the front 75% of the chord. The elimination of the suction side shock eliminates the shock losses and reduces the shape factor of the resulting boundary layer, as illustrated in the left plot of Figure 3-9. The right plot of Figure 3-9 shows that the dissipation coefficient $C_{\mathcal{D}}$ is an increasing function of shape factor $\bar{H}$ for the range of shape factors observed. A reduction in dissipation reduces the suction side entropy generation for all redesigned blades, as shown in Figure 3-10. The deterministic blade also reduces the pressure side entropy generation, giving it the lowest loss in the absence of manufacturing variability.

The pressure profiles for the robust and simultaneous optimal blades are similar, with a shock forming on the suction side for both nominal geometries. The peak Mach number on the suction side of the robust and simultaneous optimal blades are 1.15 and 1.14, respectively, compared to 1.32 for the deterministic optimal blade and 1.26 for the baseline blade. The reduction in shock strength reduces the shape factor

downstream of the shock relative to the baseline geometry, resulting in lower boundary layer losses.

The loss bucket for the deterministic optimal blade is shown in Figures 3-11. At the nominal incidence, a 7% increase in the mean loss is observed when manufacturing variations are introduced. The deterministic optimization eliminates the suction side shock, but also increases the peak suction side Mach number. Introducing manufacturing variations results in a switch in the dominant loss mechanism: shock induced separation occurs for 10% of the manufactured blades. The top right plot of Figure 3-10 illustrates the mean shift in entropy generation due to shock induced flow separation. The appearance of a suction side shock is also responsible for increasing the loss at positive incidence, and this shock is stronger than the shock observed on the baseline blade at each incidence. Less than 98% of the MISES runs converged above an incidence of $\alpha = 3.3°$, so the mean performance is not plotted in this region.

The robust design avoids the switch in flow mechanisms by reducing the peak suction side Mach number. Introducing manufacturing variations results in shock induced flow separation on 5% of the blades, resulting in a 2% increase in mean loss. Reducing the peak Mach number also improves the performance of the robust design at positive incidence by delaying the onset of shock induced separation, which is reflected in the loss bucket shown in Figure 3-12. Simultaneous optimization also avoids the switch in flow mechanisms by changing the geometry and reducing the manufacturing variability, and the flow remains attached for all manufactured blades. The loss bucket of the simultaneous optimal, plotted in Figure 3-13, has lower mean shift and variability than the loss bucket of the robust design.

The optimized tolerances are plotted in Figure 3-14. The reduction in variability on the deterministic optimal blade extends further down the suction side of the blade than for the other geometries. This reduces the percentage of blades with suction side flow separation to 3%. The optimal tolerances for the robust optimal blade are distributed according to a "double bow-tie" pattern, but the reduction in variability on the pressure side is small relative to that on the suction side. The pressure side

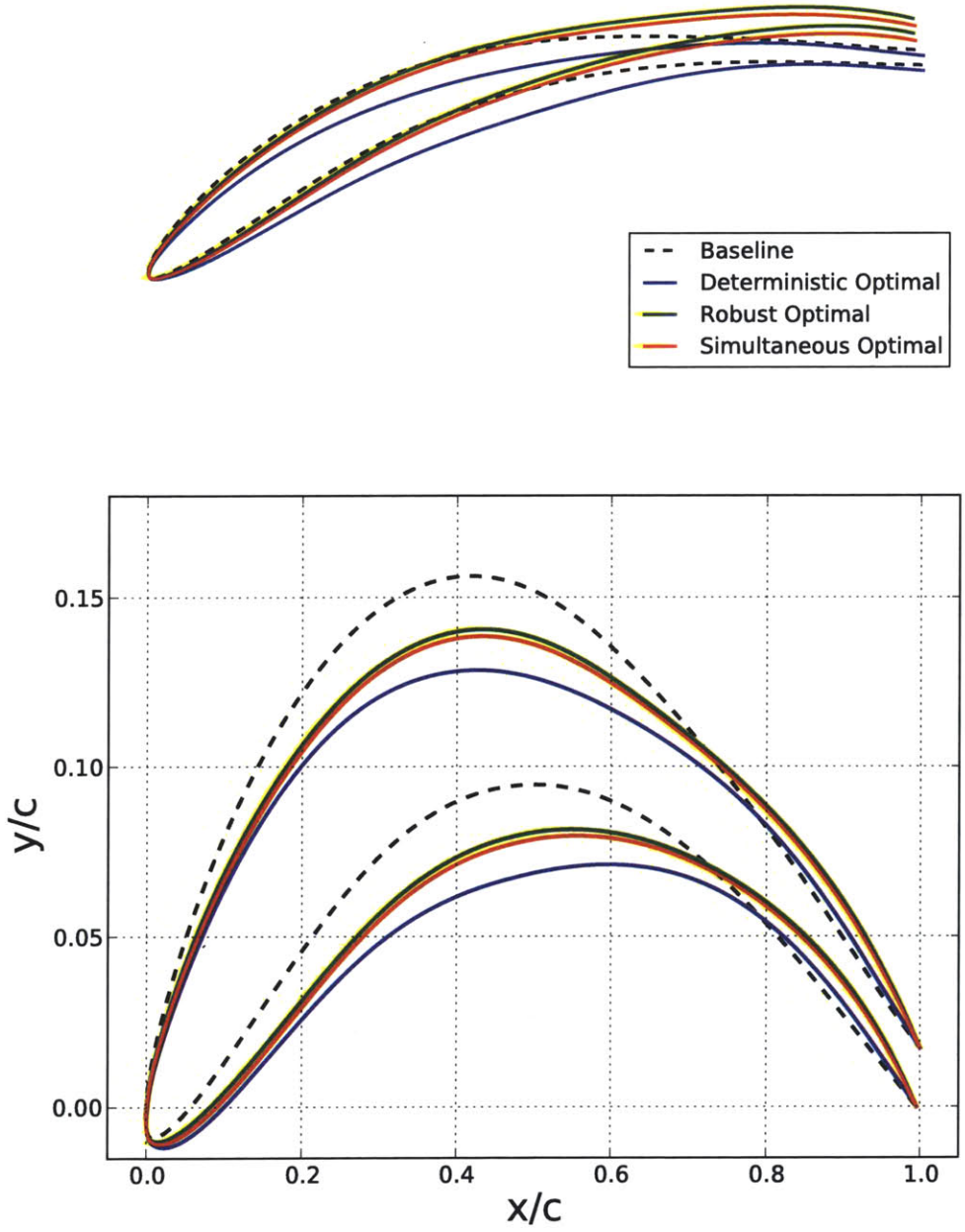

Figure 3-7: Single-point optimal redesigned UTRC blades.

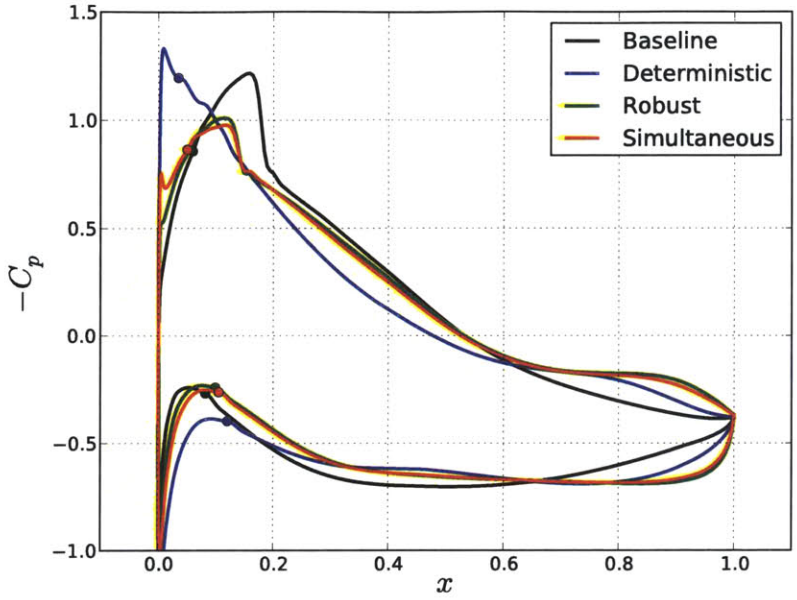

Figure 3-8: Pressure coefficient profiles for the baseline and single-point optimized UTRC blades. The dots denote the location of transition.

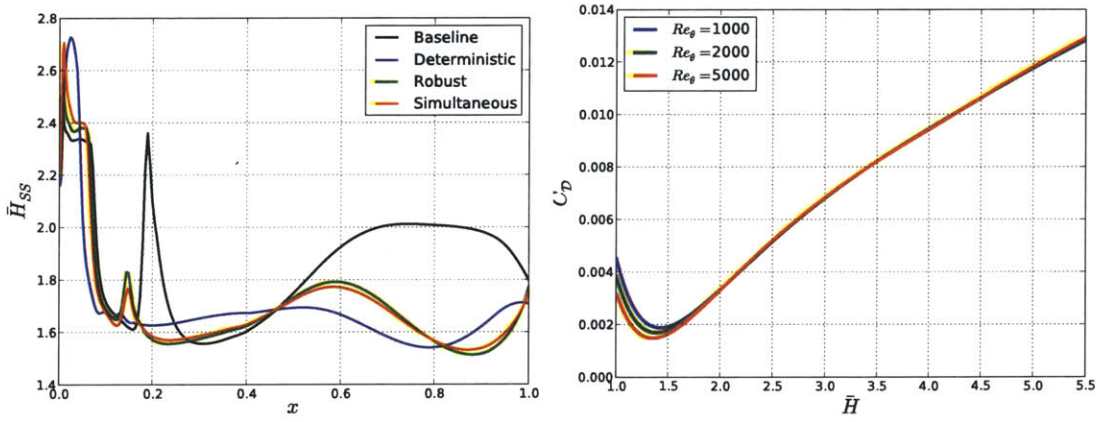

Figure 3-9: Left: suction surface shape parameter profiles for the baseline and single-point optimized UTRC blades. Right: dependence of dissipation coefficient on shape factor.

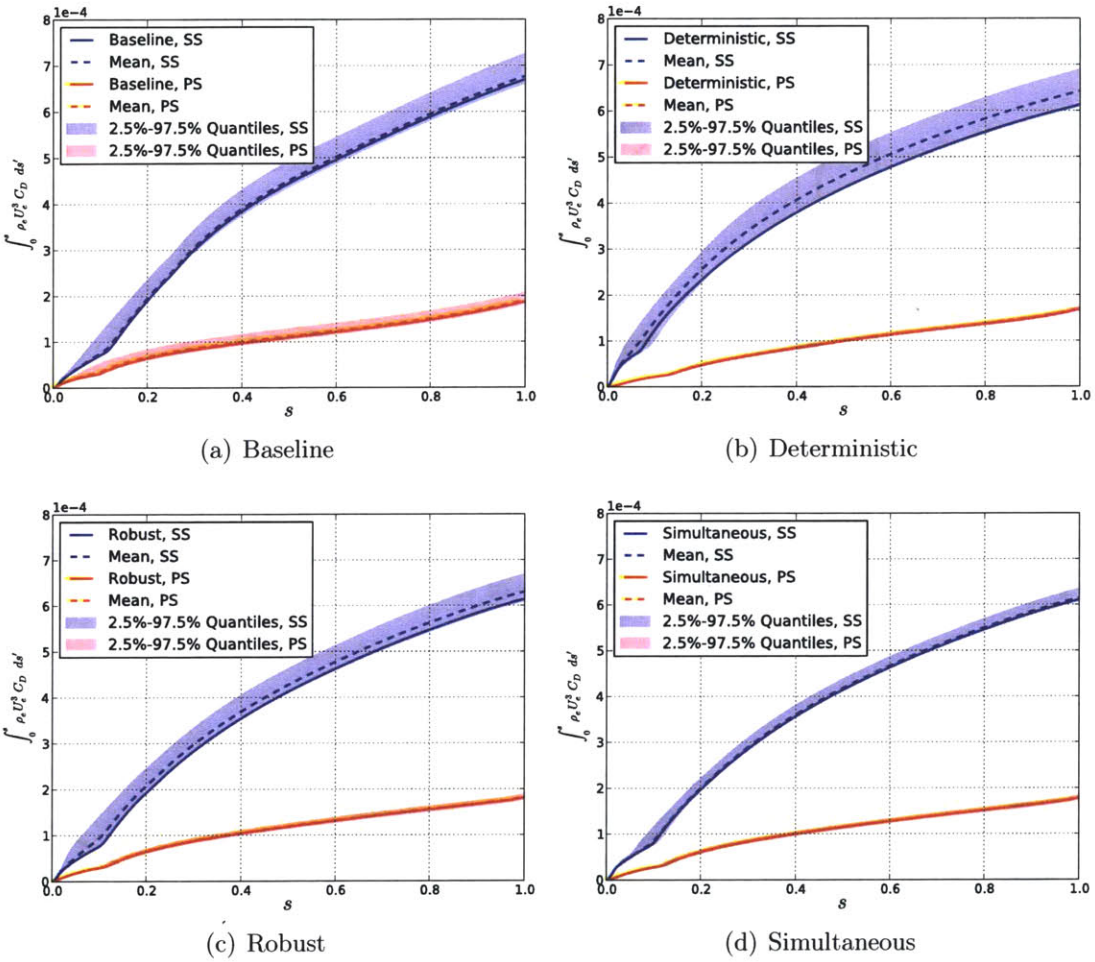

(a) Baseline

(b) Deterministic

(c) Robust

(d) Simultaneous

Figure 3-10: Boundary layer entropy generation for the baseline and single-point optimized UTRC blades. Solid lines indicate the nominal, dashed lines indicate the mean. The pressure side (PS) is plotted in red and the suction side (SS) is plotted in blue.

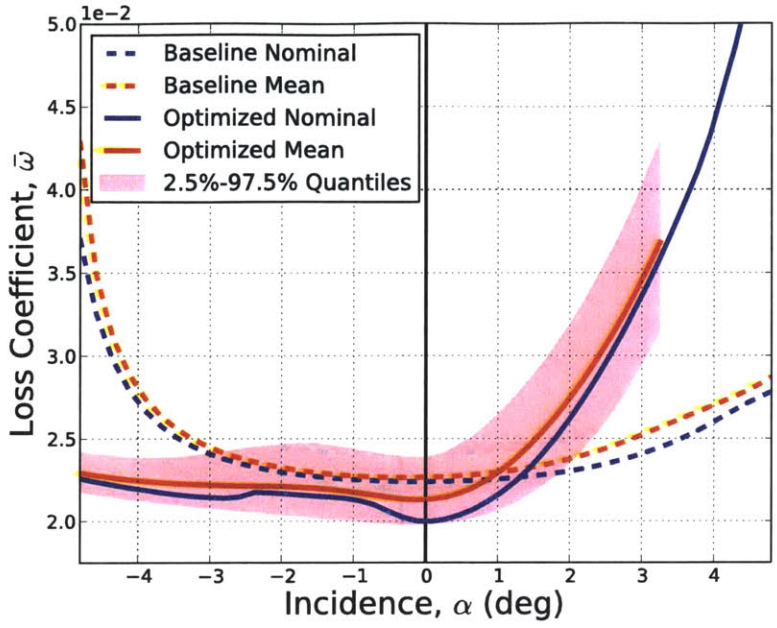

Figure 3-11: Loss coefficient versus incidence angle for the single-point deterministic optimal redesigned UTRC blade. The quantiles are plotted for the optimized blade.

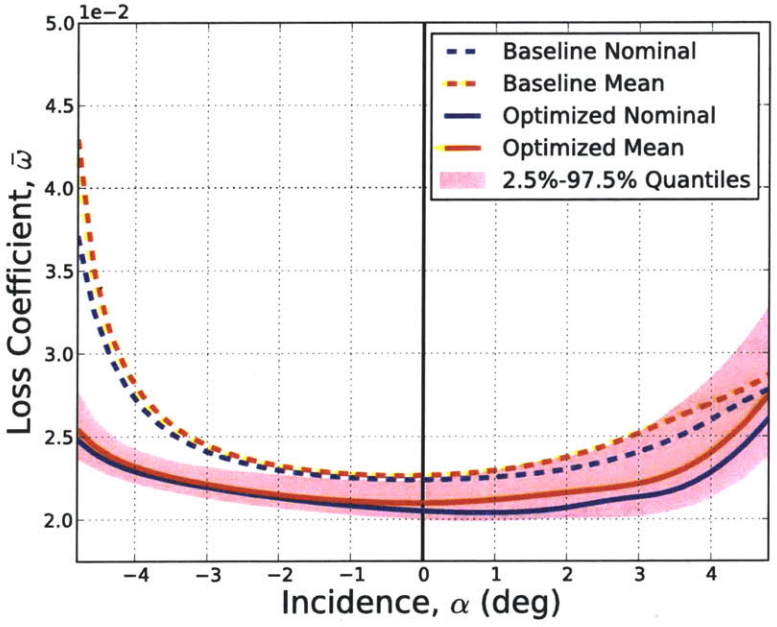

Figure 3-12: Loss coefficient versus incidence angle for the single-point robust optimal redesigned UTRC blade. The quantiles are plotted for the optimized blade.

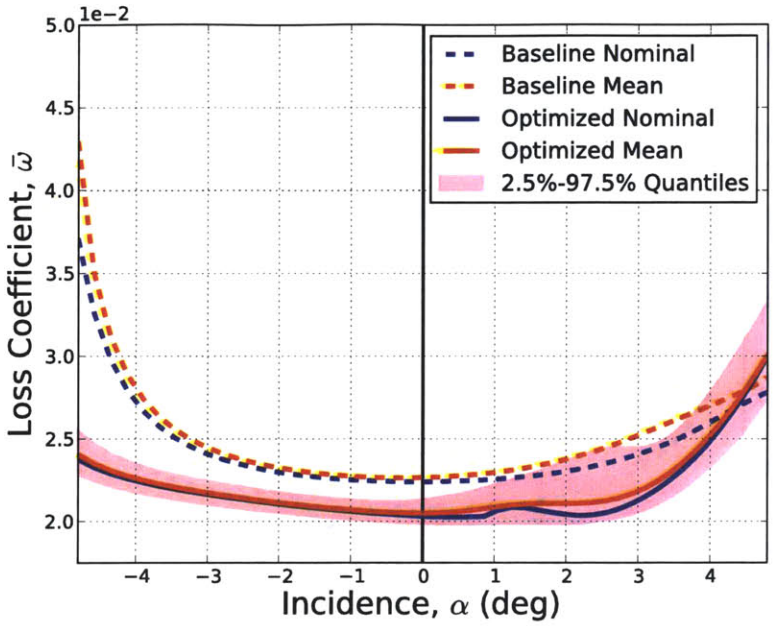

Figure 3-13: Loss coefficient versus incidence angle for the single-point simultaneous optimal redesigned UTRC blade. The quantiles are plotted for the optimized blade.

tolerances ensure flow separation does not occur on any manufactured blades. To quantify the error between two tolerance schemes $\sigma_i(s)$ and $\sigma_j(s)$, we compute the integrated error:

$$e_{i,j} = \frac{\int_S \left| [\sigma_{max} - \sigma_i(s)] - [\sigma_{max} - \sigma_j(s)] \right| \, ds}{\int_S [\sigma_{max} - \sigma_i(s)] + [\sigma_{max} - \sigma_j(s)] \, ds}.$$

The largest error between the three optimal tolerance schemes is 37%, illustrating that the optimal tolerance scheme is geometry dependent.

3.4.2.2 Multi-Point Optimization

To perform multi-point optimization, we use $N_p = 3$ design points at $\beta_1 = 38.7°$, 43.2°, and 47.7° and a weight vector $\mathbf{w} = \{1/4,\ 1/2,\ 1/4\}$. Comparing Tables 3.3 and 3.1 illustrates that the multi-point optimizations are roughly three times as computa-

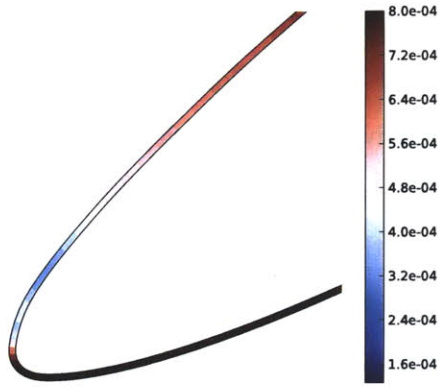

(a) Deterministic Optimal Tolerances

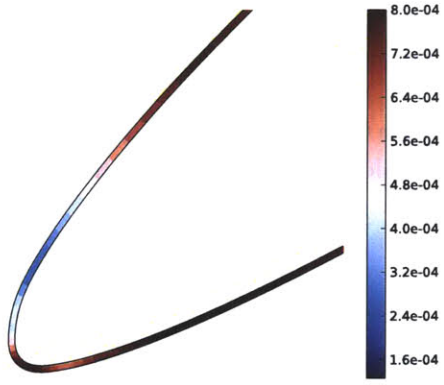

(b) Robust Optimal Tolerances

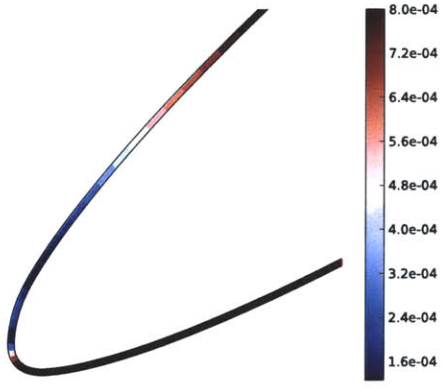

(c) Simultaneous Optimal Tolerances

Figure 3-14: Optimal standard deviation $\sigma(s)/c$ for the single-point optimized UTRC blades. The lower surface is the pressure side, and the upper surface is the suction side.

tionally expensive as the equivalent single-point optimizations. The number of SQP iterations and objective/constraint evaluations remains nearly unchanged between the single-point and multi-point optimizations, but each objective/constraint evaluation is three times more expensive since three design points are used in the multi-point approach. The convergence histories for the multi-point optimizations, plotted in Figure 3-15, indicate that all three designs attain the same weighted mean loss. The performance of the multi-point optimal designs is summarized in Table 3.4.

	Det. Geometry	Det. Tolerance	Robust Geometry	Robust Tolerance	Simultaneous
N	-	500	500	500	500
# SQP iter	12	32	13	26	53
# Obj. evals	14	42	16	36	110
# MISES runs	42	63,000	24,000	54,000	165,000

Table 3.3: Number of Monte Carlo samples, SQP iterations, objective/constraint evaluations, and MISES flow calculations for the multi-point optimizations of the UTRC blade.

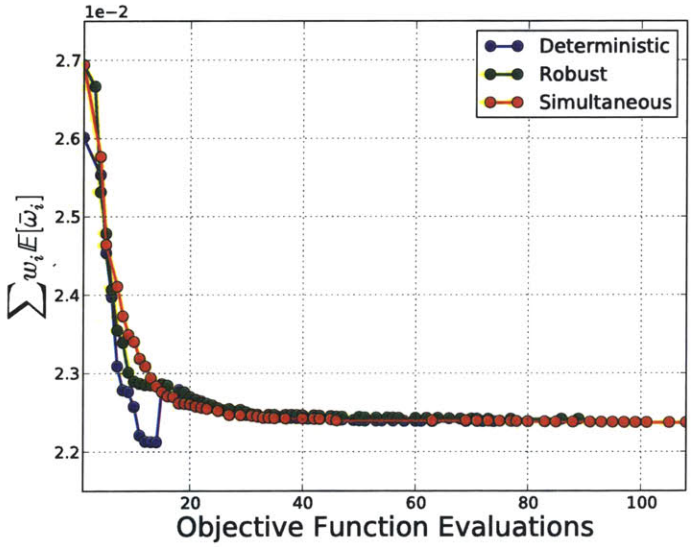

Figure 3-15: Convergence history for the multi-point optimizations of the UTRC blade. The dots indicate SQP iterations.

	Baseline	Deterministic	Robust	Simultaneous
$\sum w_i \bar{\omega}_i$	2.60×10^{-2}	2.22×10^{-2}	2.22×10^{-2}	2.22×10^{-2}
$\sum w_i \mathbb{E}[\bar{\omega}_i(\boldsymbol{\sigma}_b)]$	2.68×10^{-2}	2.29×10^{-2}	2.29×10^{-2}	2.29×10^{-2}
$\sum w_i \mathbb{E}[\bar{\omega}_i(\boldsymbol{\sigma}^*)]$	2.64×10^{-2}	2.23×10^{-2}	2.23×10^{-2}	2.23×10^{-2}

Table 3.4: Performance comparison of the baseline UTRC, multi-point deterministic optimal, multi-point robust optimal, and multi-point simultaneous optimal geometries.

The multi-point optimal geometries are shown in Figure 3-16. The surfaces of the optimized geometries are within 0.5% of the chord length. We therefore analyze the multi-point deterministic optimal geometry, since the same conclusions hold for the robust and simultaneous optimal geometries. The multi-point optimal geometries are similar to the single-point robust geometry: the optimizer reduces the camber of the blade, and decreases the blade stagger.

The pressure coefficient profiles for the baseline and multi-point deterministic optimal geometries are compared in Figure 3-17, showing that the optimizer shifts the loading toward the trailing edge which reduces the strength of the suction side shock. The effect of reducing the suction side shock strength on the entropy generation is shown in Figure 3-18, which compares the baseline and optimized blades with uniform manufacturing tolerances. At negative incidence ($\beta_1 = 38.7°$), reducing the shock strength reduces the nominal entropy generation and the mean shift in entropy generation, since the flow separates on the suction surface for only 5% of the manufactured blades, whereas suction side flow separation occurs on 35% of the manufactured baseline blades.

On the pressure side of the blade, the design changes have the largest impact at negative incidence. Decreasing the blade stagger reduces the number of blades with pressure side flow separation from 50% down to 14%. As a result, the mean shift in the pressure side entropy generation is 40% lower for the optimized blade.

Figure 3-19 shows that the multi-point optimal designs reduce the nominal and mean loss over the entire incidence range considered. The "kink" in the loss bucket of the nominal blade near $\alpha = 2.3°$ is a result of the suction side transition location

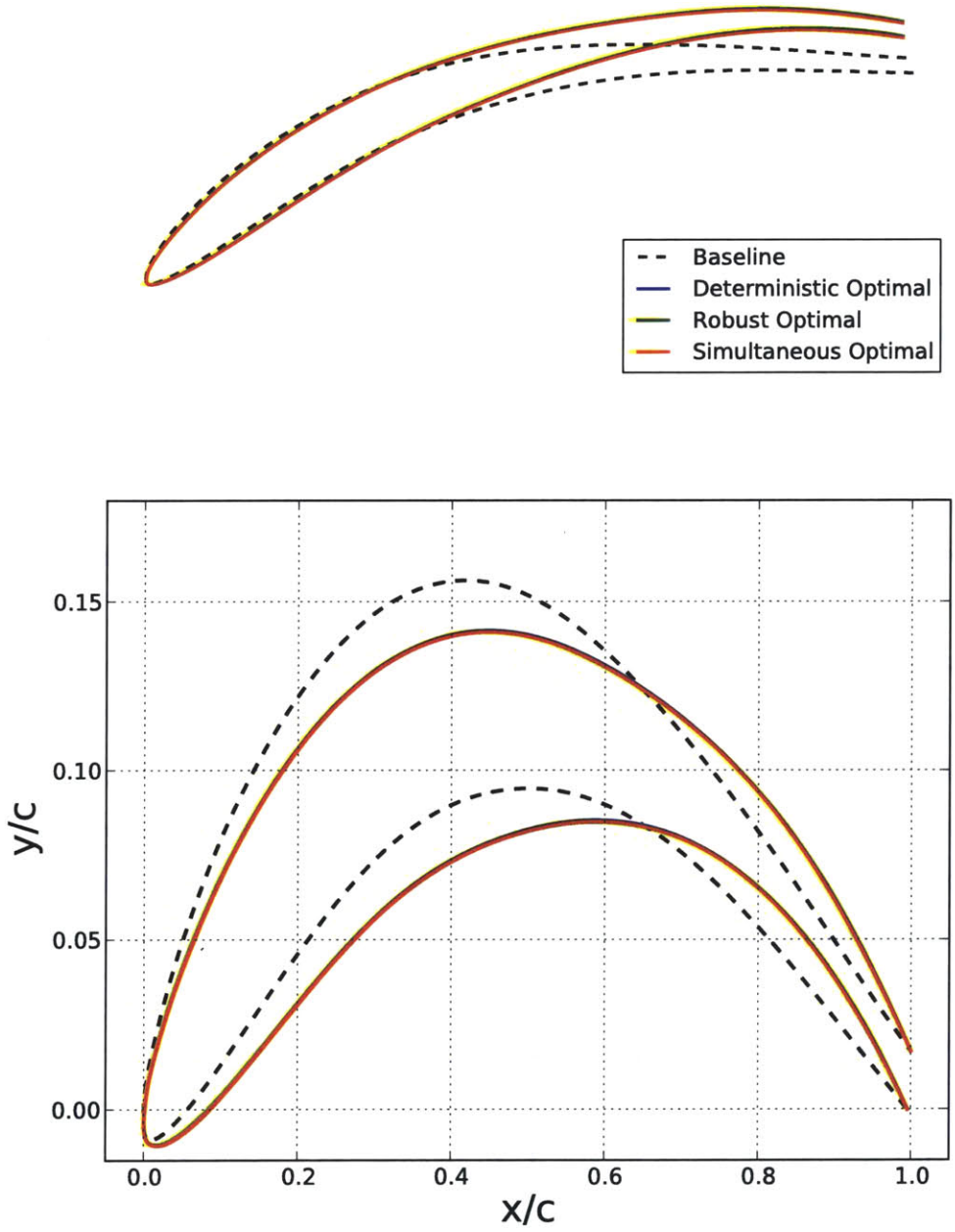

Figure 3-16: Multi-point optimal redesigned UTRC blades.

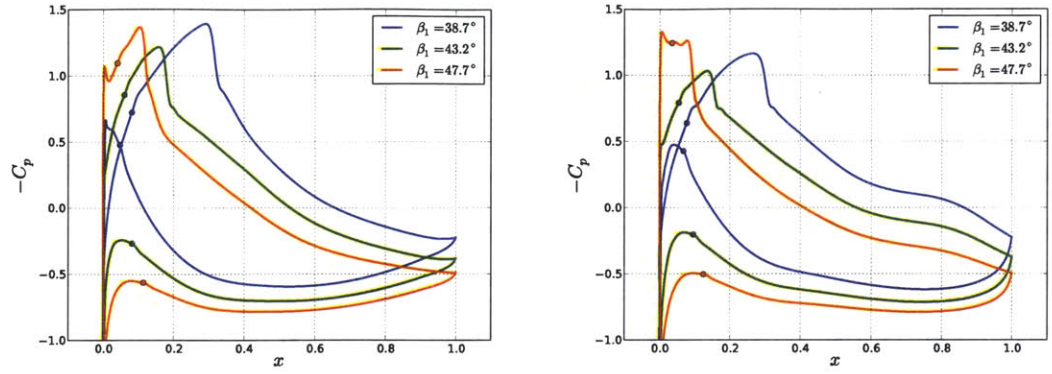

(a) Baseline

(b) Multi-point Deterministic Optimal

Figure 3-17: Comparison between the baseline (left) and multi-point deterministic optimal (right) pressure coefficient profiles for the UTRC blade. The transition locations are indicated by dots.

shifting towards the trailing edge as the leading edge pressure spike disappears with increasing incidence. The multi-point optimal geometry reduces the nominal and mean loss by an average of 10% over the incidence range considered. Optimizing the geometry and tolerances reduces the mean loss by an average of 13%.

The single-point deterministic optimal design eliminated the shock at the nominal incidence, but increased the shock strength at positive incidence relative to the baseline design. The multi-point deterministic optimal does not eliminate the suction side shock at any of the design points. Including variations in incidence has a similar effect as including manufacturing variations: the multi-point optimal design avoids regions of the design space where a switch in the dominant loss mechanism occurs. For the multi-point optimization, robustness to flow incidence implies robustness to manufacturing variations, since changes in incidence have a larger effect on the mean performance than manufacturing variability.

Multi-point deterministic and robust designs are not always found to be similar. Goodhand et al. demonstrated that for design changes on the same length scale as the manufacturing variations, deterministic and robust multi-point design approaches result in different optimal designs [33]. The similarity between the multi-point opti-

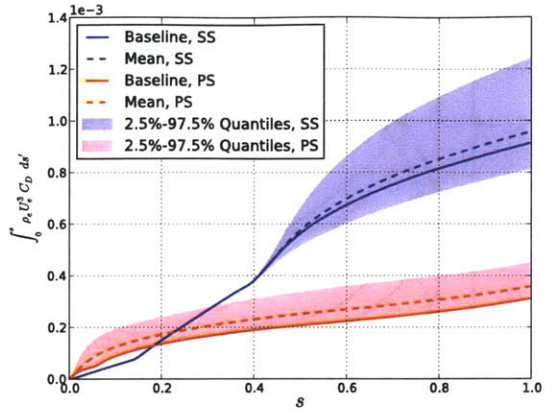

(a) $\beta_1 = 38.7°$, Baseline

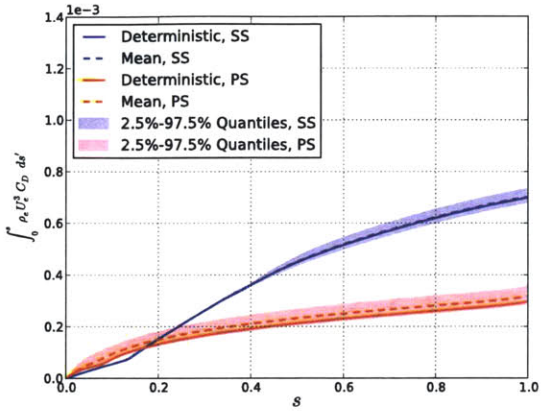

(b) $\beta_1 = 38.7°$, Deterministic Optimal

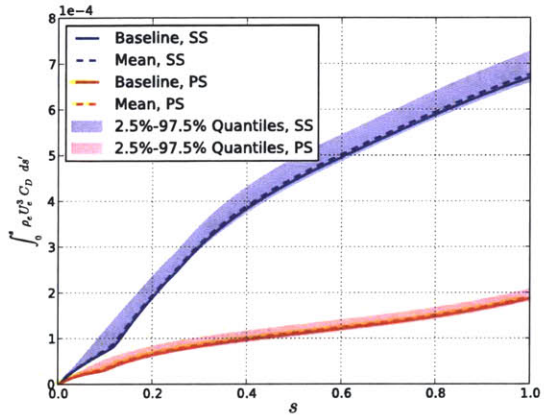

(c) $\beta_1 = 43.2°$, Baseline

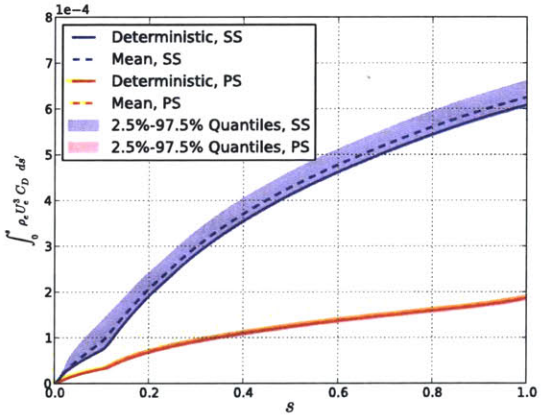

(d) $\beta_1 = 43.2°$, Deterministic Optimal

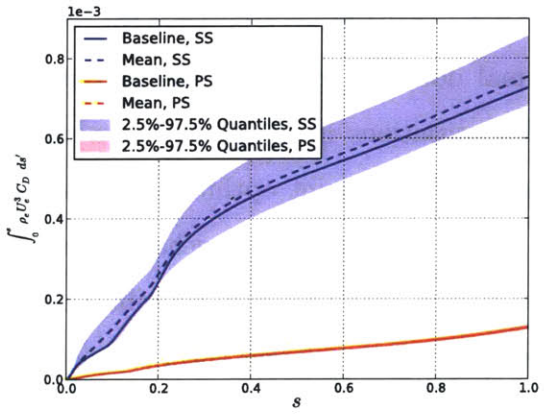

(e) $\beta_1 = 47.7°$, Baseline

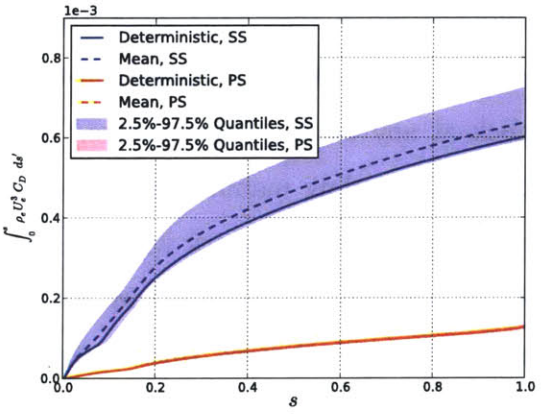

(f) $\beta_1 = 47.7°$, Deterministic Optimal

Figure 3-18: Comparison of the boundary layer entropy generation rate for the baseline and multi-point deterministic optimal UTRC blades. Solid lines indicate the nominal, dashed lines indicate the mean. The pressure side (PS) is plotted in red and the suction side (SS) is plotted in blue.

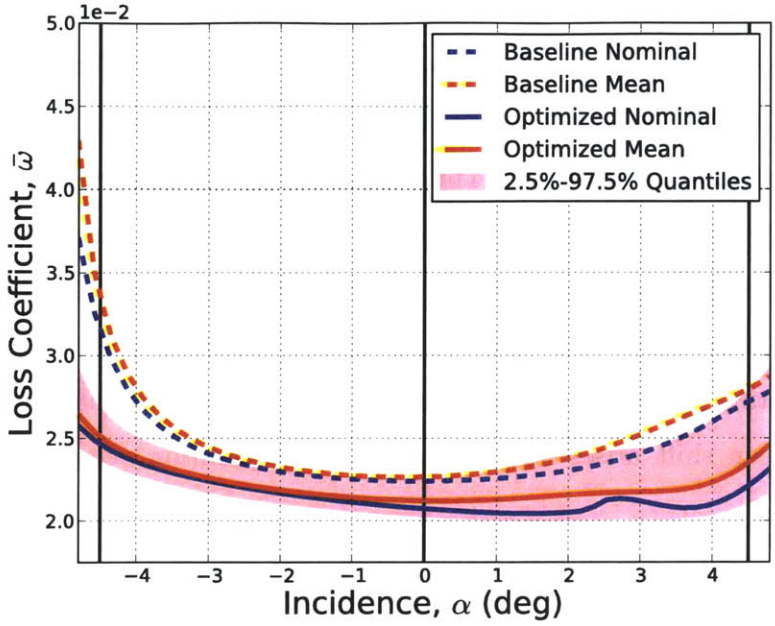

Figure 3-19: Loss coefficient versus incidence angle for the multi-point deterministic optimal redesigned UTRC blade. The quantiles are plotted for the optimized blade.

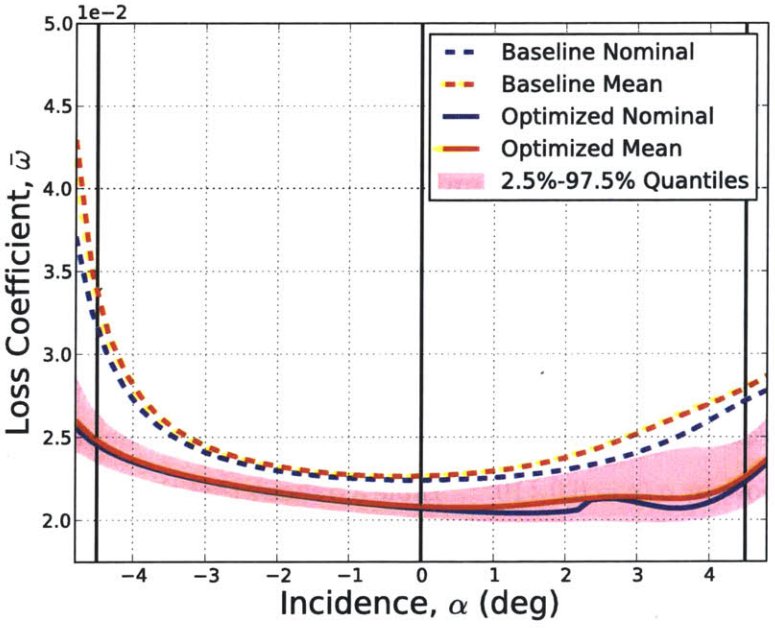

Figure 3-20: Loss coefficient versus incidence angle for the multi-point simultaneous optimal redesigned UTRC blade. The quantiles are plotted for the optimized blade.

mized geometries found in this thesis is a result of using design variables that alter the geometry on length scales larger than the manufacturing variations.

The insensitivity of the optimal multi-point geometry to manufacturing variations implies that sequential tolerance design should give similar results to tolerances produced by the simultaneous approach. The largest error between the optimal tolerances, plotted in Figure 3-21 is 8%, four times smaller than the maximum error between the single-point optimal tolerances. The multi-point optimal tolerances decrease the standard deviation near the leading edge of the blade, resulting in a "double bow-tie" tolerance pattern. The greatest decrease is on the suction side of the blade, since most of the mean shift arises due to suction side separation occurring at positive incidence.

Figure 3-22 compares the entropy generation between the baseline UTRC blade with optimized tolerances presented in Chapter 2 and the multi-point simultaneous optimal design. The mean shift and variability in entropy generation is lower at each incidence for the simultaneous optimal design, illustrating the benefits of optimizing both geometry and tolerances.

3.4.3 SC10 Rotor

3.4.3.1 Single-Point Optimization

For the SC10 blade, the single-point optimizations minimize the loss at the nominal inflow angle of $\beta_1^{des} = 53.5°$, and constrain the turning to be equal to the turning of the baseline blade at the design incidence. To optimize the tolerances, the total variability was constrained to be 98% of the baseline value, and the standard deviation was bounded above by $\sigma/c = 6.0\times10^{-4}$. Table 3.5 shows that the computational cost of these optimizations is roughly the same as the single-point UTRC optimizations. Table 3.6 compares the performance of the baseline and optimized blades. The deterministic optimal blade has 9% lower loss than the baseline blade, and the robust optimal blade reduces the mean loss by 9% relative to the baseline blade.

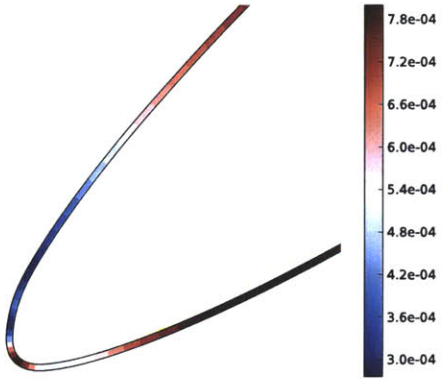

(a) Deterministic Optimal Tolerances

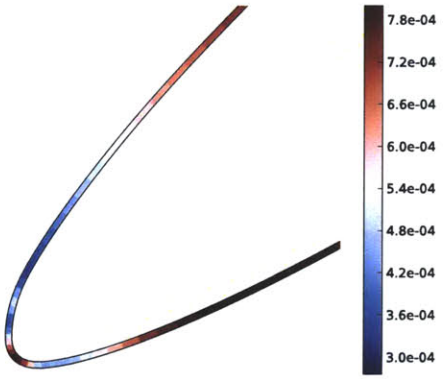

(b) Robust Optimal Tolerances

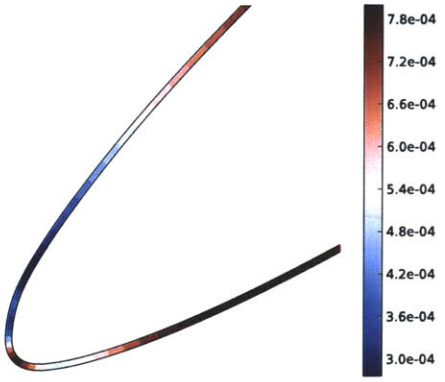

(c) Simultaneous Optimal Tolerances

Figure 3-21: Optimal standard deviation $\sigma(s)/c$ for the multi-point optimized UTRC blades. The lower surface is the pressure side, and the upper surface is the suction side.

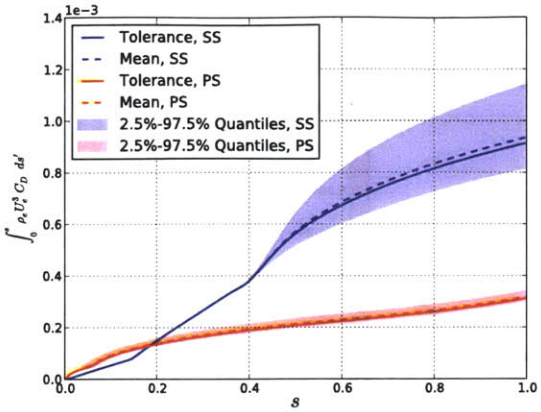

(a) $\beta_1 = 38.7°$, Optimized Tolerances

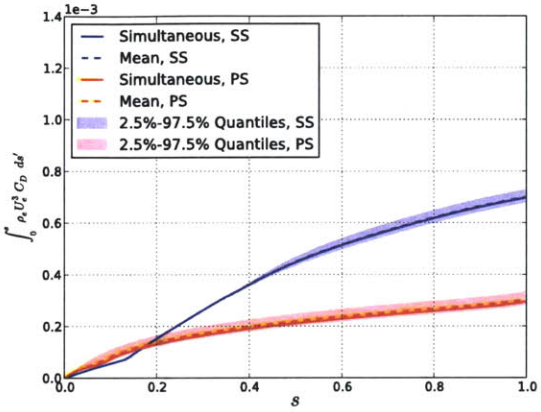

(b) $\beta_1 = 38.7°$, Simultaneous Optimal

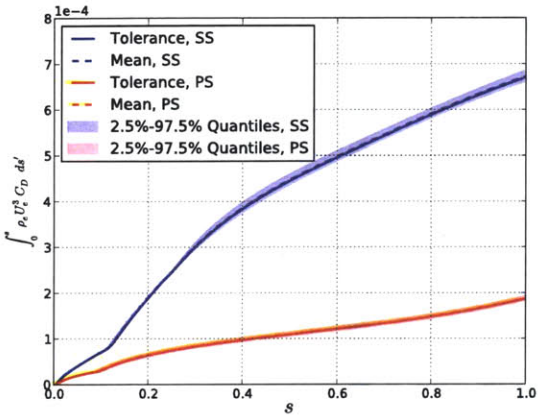

(c) $\beta_1 = 43.2°$, Optimized Tolerances

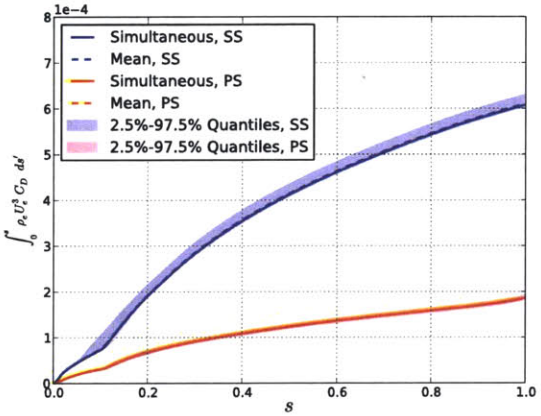

(d) $\beta_1 = 43.2°$, Simultaneous Optimal

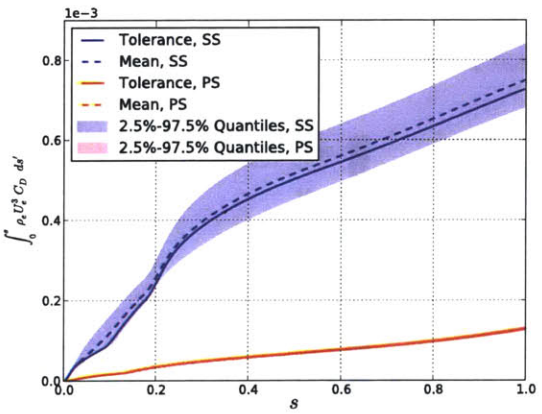

(e) $\beta_1 = 47.7°$, Optimized Tolerances

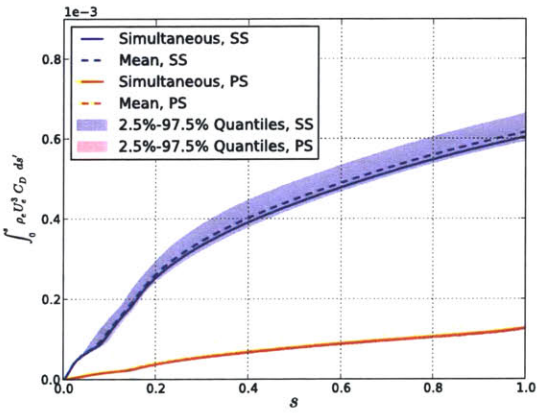

(f) $\beta_1 = 47.7°$, Simultaneous Optimal

Figure 3-22: Comparison of the boundary layer entropy generation rate for the baseline UTRC blade with optimized tolerances and the multi-point simultaneous optimized blade. Solid lines indicate the nominal, dashed lines indicate the mean. The pressure side (PS) is plotted in red and the suction side (SS) is plotted in blue.

	Det. Geometry	Det. Tolerance	Robust Geometry	Robust Tolerance	Simultaneous
N	-	500	500	500	500
# SQP iter	9	43	11	36	45
# Obj. evals	15	83	21	65	98
# MISES runs	15	41,500	10,500	32,500	49,000

Table 3.5: Number of Monte Carlo samples, SQP iterations, objective/constraint evaluations, and MISES flow calculations for the single-point optimizations of the SC10 blade.

	Baseline	Deterministic	Robust	Simultaneous
$\bar{\omega}$	1.52×10^{-2}	1.39×10^{-2}	1.39×10^{-2}	1.39×10^{-2}
$\mathbb{E}[\bar{\omega}(\boldsymbol{\sigma}_b)]$	1.53×10^{-2}	1.42×10^{-2}	1.40×10^{-2}	1.41×10^{-2}
$\mathbb{E}[\bar{\omega}(\boldsymbol{\sigma}^*)]$	1.52×10^{-2}	1.39×10^{-2}	1.39×10^{-2}	1.39×10^{-2}

Table 3.6: Performance comparison of the baseline SC10, single-point deterministic optimal, single-point robust optimal, and single-point simultaneous optimal designs.

The single-point optimized blades are plotted together in Figure 3-23. The stagger angles of the optimized blades are between 1.8° and 2.1° lower than the baseline blade. The camber of the trailing 80% of the optimal blades is reduced, resulting in blades with flat pressure surfaces. The deterministic optimal blade is the flattest and has the lowest stagger.

The pressure distributions of the baseline and optimized blades are compared in Figure 3-24. The pressure profiles of the optimized blades are typical of controlled diffusion airfoils [13]. The flow on the suction surface is accelerated to the transition location, with a peak Mach number of 1.11, and then decelerated to the trailing edge without the formation of a shock. The pressure profile on the pressure side remains flat. Comparing the suction side entropy generation, plotted in Figure 3-25, shows that more entropy is generated over the first half of the optimized blades. The entropy generation rate slows over the rear of the blade, so that the nominal and mean suction side boundary layer losses are within 1% for the baseline and optimized blades.

The reduction in loss achieved by the optimized blades is primarily a result of lower pressure side boundary layer losses. The flatter pressure side pressure profile

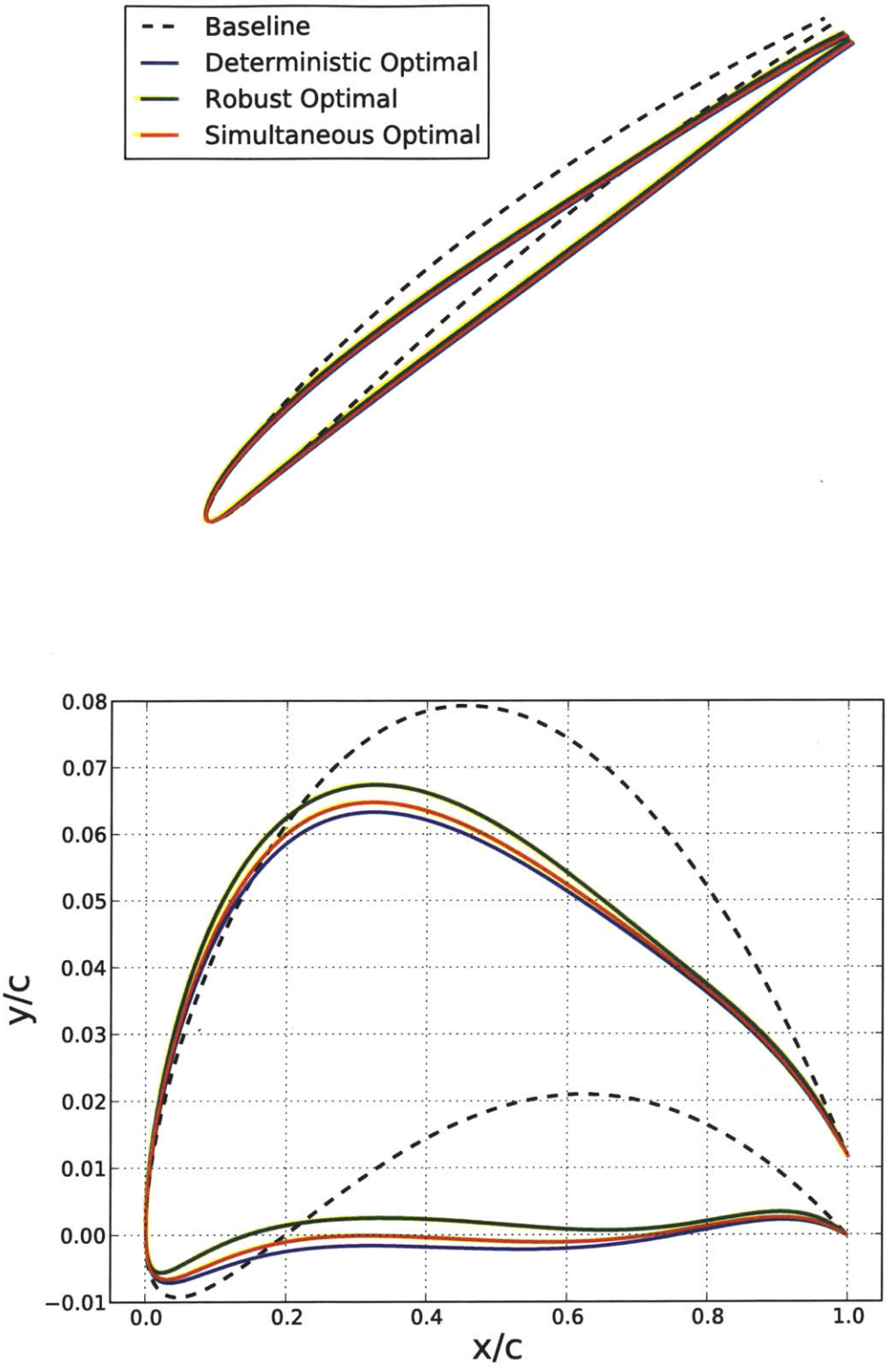

Figure 3-23: Single-point optimal redesigned SC10 blades.

delays transition, resulting in a 3% reduction in the pressure side boundary layer entropy generation for the deterministic optimal blade relative to the baseline blade. A 3% reduction in the mean pressure side entropy generation is achieved by the robust optimal blade.

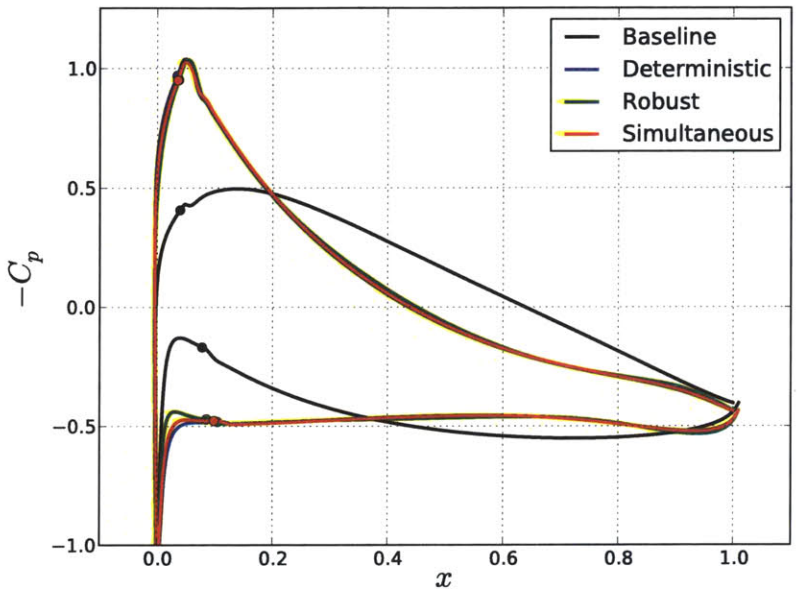

Figure 3-24: Pressure coefficient profiles for the baseline and single-point optimized SC10 blades at $\beta_1 = 53.5°$. The dots denote the location of transition.

The loss buckets for the optimized blades, shown in Figures 3-26 to 3-28, are shifted relative to the loss bucket of the baseline geometry, with higher loss at positive incidence. This is a result of shock-induced flow separation on the suction side of the blade that occurs at positive incidence.

To understand why the deterministic and robust optimal SC10 blades differ, we compare the change in entropy generation for the nominal geometries and the change in the mean entropy generation for the manufactured blades in Figure 3-29. Suction side flow separation occurs on 6% of the manufactured deterministic optimal blades, resulting in a 2% increase in the mean suction side entropy generation. The entropy generation is three times higher on the suction side of the blade than on the pressure

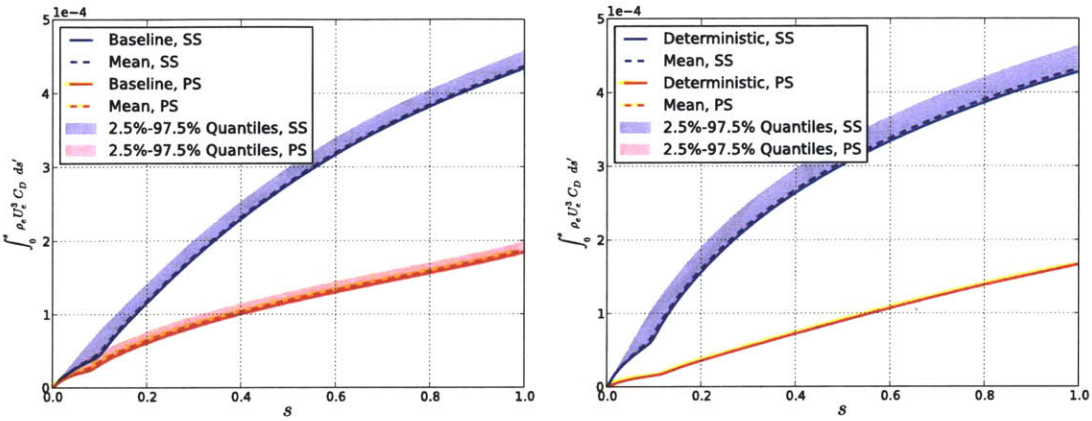

(a) Baseline

(b) Deterministic

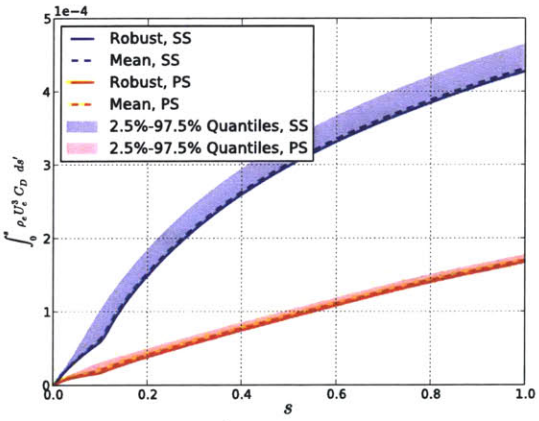

(c) Robust

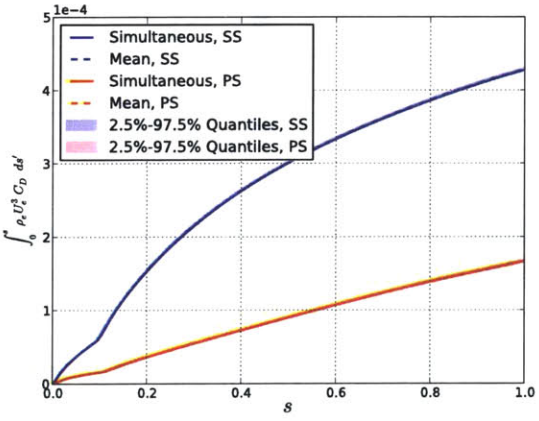

(d) Simultaneous

Figure 3-25: Boundary layer entropy generation for the baseline and single-point optimized SC10 blades. Solid lines indicate the nominal, dashed lines indicate the mean. The pressure side (PS) is plotted in red and the suction side (SS) is plotted in blue.

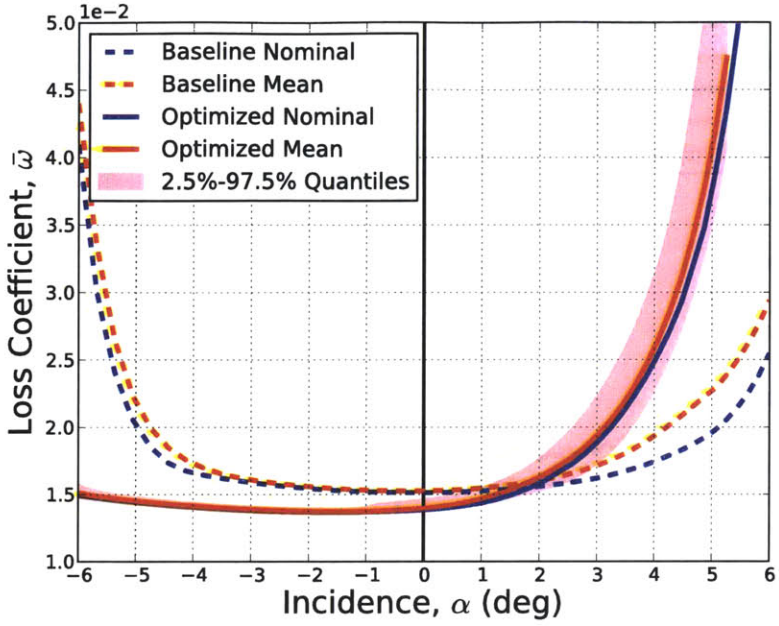

Figure 3-26: Loss coefficient versus incidence angle for the single-point deterministic optimal redesigned SC10 blade. The quantiles are plotted for the optimized blade.

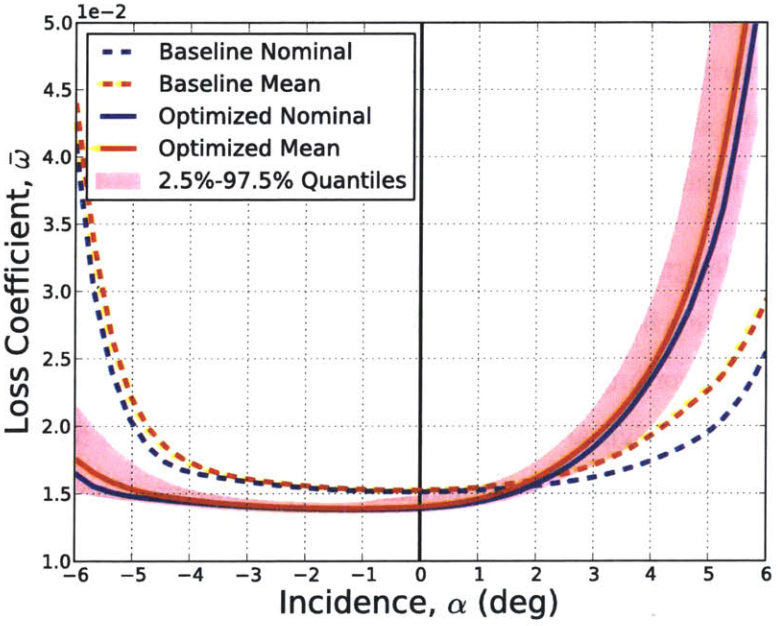

Figure 3-27: Loss coefficient versus incidence angle for the single-point robust optimal redesigned SC10 blade. The quantiles are plotted for the optimized blade.

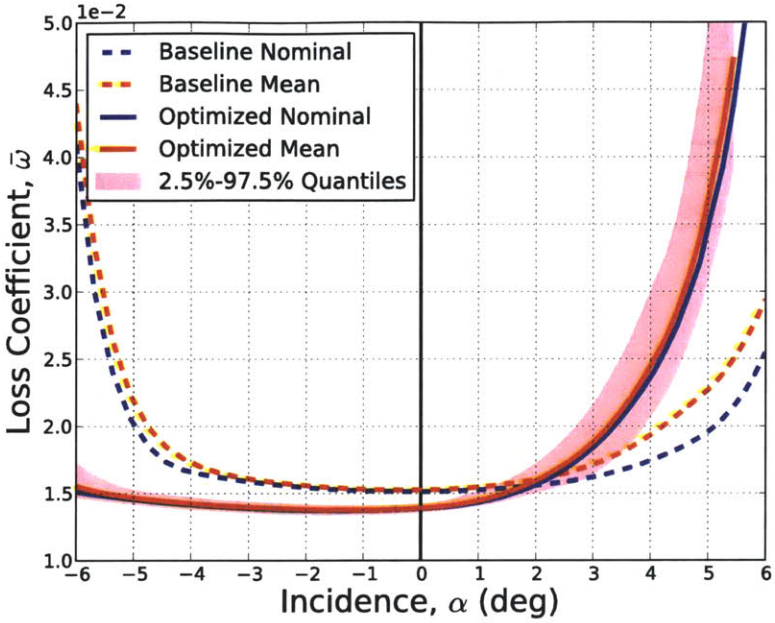

Figure 3-28: Loss coefficient versus incidence angle for the single-point simultaneous optimal redesigned SC10 blade. The quantiles are plotted for the optimized blade.

side, so the suction side losses are the dominant design driver in the presence of manufacturing variability. The robust design reduces the acceleration around the leading edge of the suction side of the blade, which shifts the mean transition location 2% closer to the trailing edge.

The switch in design drivers from pressure side loss to suction side loss is reflected in the optimal tolerance schemes, shown in Figure 3-30. The optimized tolerance schemes are all distributed according to the "double bow-tie" pattern. The optimal tolerances for the deterministic design are reduced more on the suction side to delay the mean transition location in the presence of manufacturing variations. The tolerances on the robust design are reduced more on the pressure side, where most of the mean shift in loss occurs for this design. The integrated error between the deterministic and robust optimal tolerances is 66%, reflecting a strong dependence of the optimal tolerances on the geometry.

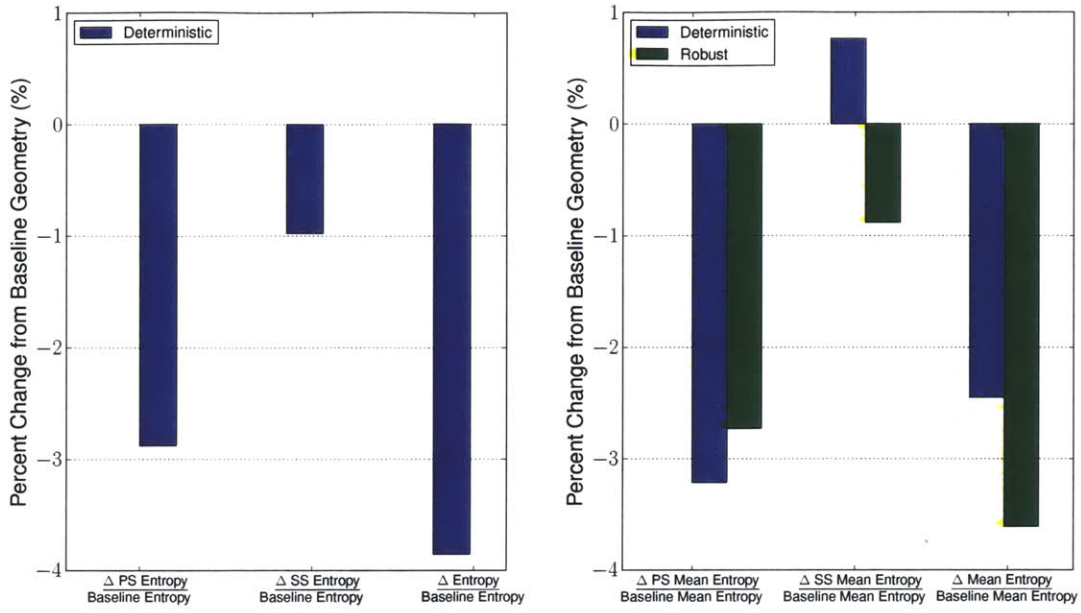

(a) Nominal Geometry

(b) Manufactured Geometries

Figure 3-29: Percent change in the nominal (left) and mean (right) entropy generation for the single-point deterministic and robust optimal SC10 blades relative to the baseline SC10 blade.

3.4.3.2 Multi-Point Optimization

To improve the off-design performance of the SC10 blade, multi-point optimizations were performed using $N_p = 3$ design points at $\beta_1 = 48.5°,\ 53.5°$, and $58.5°$. We use the same weight vector $\mathbf{w} = \{1/4,\ 1/2,\ 1/4\}$ used to perform the multi-point optimizations of the UTRC blade. The total variability V_b was constrained to 98% of the baseline value, and the standard deviation was constrained to be less than $\sigma/c = 6.0 \times 10^{-4}$ in the tolerance optimizations. The computational cost of the multi-point optimizations are compared in Table 3.7. The convergence histories are plotted in Figure 3-31, and the performance of the optimized blades is summarized in Table 3.8.

The multi-point optimized SC10 geometries are plotted in Figure 3-32. The distance between the optimized blade surfaces is less than 0.4% of the blade chord, and the optimal blades are similar to the single-point optimized SC10 blades, with a re-

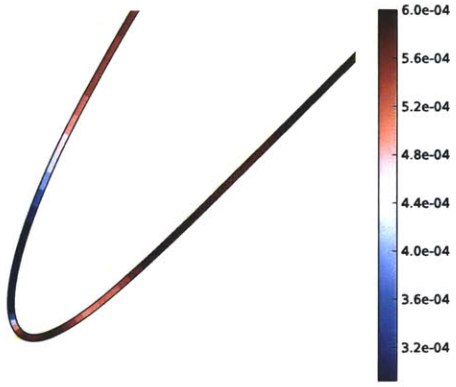

(a) Deterministic Optimal Tolerances

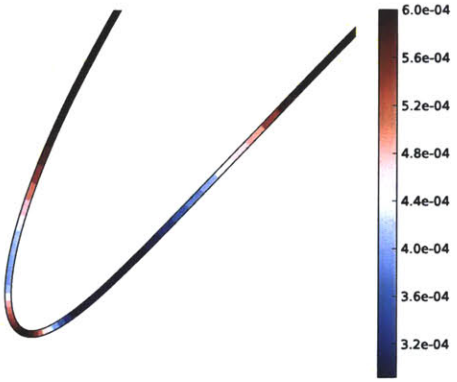

(b) Robust Optimal Tolerances

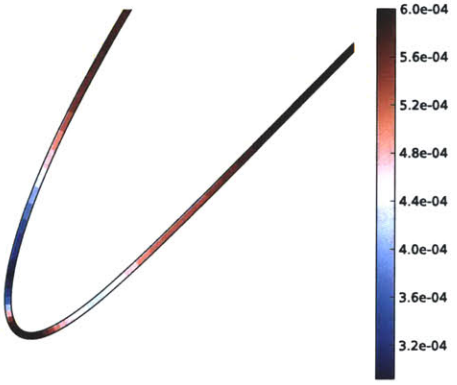

(c) Simultaneous Optimal Tolerances

Figure 3-30: Optimal standard deviation $\sigma(s)/c$ for the single-point optimized SC10 blades. The lower surface is the pressure side, and the upper surface is the suction side.

	Det. Geometry	Det. Tolerance	Robust Geometry	Robust Tolerance	Simultaneous
N	-	500	500	500	500
# SQP iter	12	24	11	27	46
# Obj. evals	16	64	15	71	95
# MISES runs	48	96,000	22,500	106,500	142,500

Table 3.7: Number of Monte Carlo samples, SQP iterations, objective/constraint evaluations, and MISES flow calculations for the multi-point optimizations of the SC10 blade.

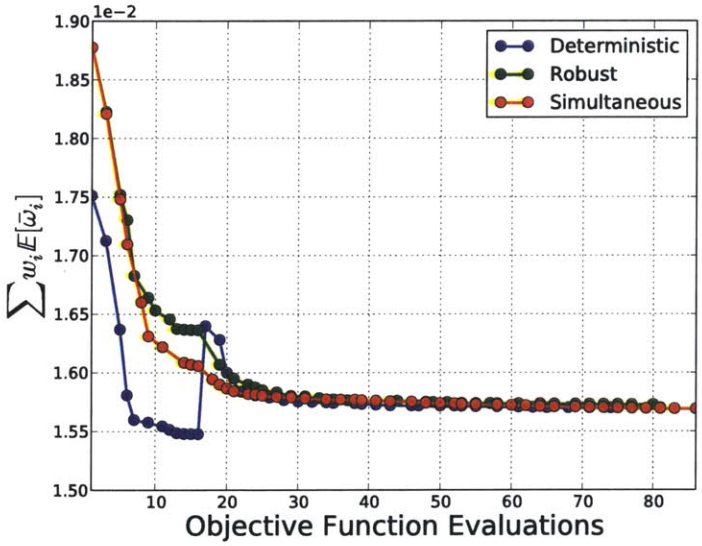

Figure 3-31: Convergence history for the multi-point optimizations of the SC10 blade. The dots indicate SQP iterations.

	Baseline	Deterministic	Robust	Simultaneous
$\sum w_i \bar{\omega}_i$	1.75×10^{-2}	1.55×10^{-2}	1.55×10^{-2}	1.55×10^{-2}
$\sum w_i \mathbb{E}[\bar{\omega}_i(\boldsymbol{\sigma}_b)]$	1.88×10^{-2}	1.64×10^{-2}	1.64×10^{-2}	1.64×10^{-2}
$\sum w_i \mathbb{E}[\bar{\omega}_i(\boldsymbol{\sigma}^*)]$	1.78×10^{-2}	1.57×10^{-2}	1.57×10^{-2}	1.57×10^{-2}

Table 3.8: Performance comparison of the baseline SC10, multi-point deterministic optimal, multi-point robust optimal, and multi-point simultaneous optimal geometries.

duction in the blade stagger angle and decreased camber over the aft 80% of the blade. The stagger angle of the optimized blades is 1.0° lower than the baseline blade, half of the average change in stagger made by the single-point optimization.

At the negative incidence design point ($\beta_1 = 48.5°$), the majority of the performance improvement is a result of lower losses generated on the pressure side of the blade, which reduces the loss coefficient by 23%. Comparing the baseline and optimized pressure coefficient profiles plotted in Figure 3-33 shows that the pressure gradient over the first 20% of the pressure surface is less adverse for the optimized blades at all three design points. This reduces the extent of flow separation at negative incidence. Flow separation occurs for 72% of the optimized manufactured blades, compared to 93% of the baseline manufactured blades. Comparing the entropy generation at negative incidence, shown at the top of Figure 3-34, the optimized blades have lower nominal and pressure side loss. At the nominal incidence ($\beta_1 = 53.5°$), the optimized blade has lower pressure side losses, reducing the loss by 8%. At the positive incidence design point ($\beta_1 = 58.5°$), the optimized blade reduces the loss by 7%. The plots at the bottom of 3-34 show that the optimized blade has higher boundary layer losses, indicating the improvement in performance is a result of lower mixing losses in the wake. The same behavior is observed in the mean entropy generation, where the mean suction side entropy is higher for the optimized blades, but the mean loss is 6% lower. Trailing edge flow separation occurs for 60% fewer of the optimized manufactured blades compared to the baseline geometry, which lowers the mean mixing losses in the wake.

The loss buckets of the deterministic and simultaneous optimal designs are shown in Figures 3-35 and 3-36, respectively. The multi-point optimal geometry reduces the nominal and mean loss by an average of 11% over the incidence range considered. Optimizing the geometry and tolerances reduces the mean loss by an average of 13%.

The differences between the single-point optimized SC10 blades were a result of changes in the transition location that result in small changes in loss compared to the changes resulting from varying the incidence angle. Both the deterministic and

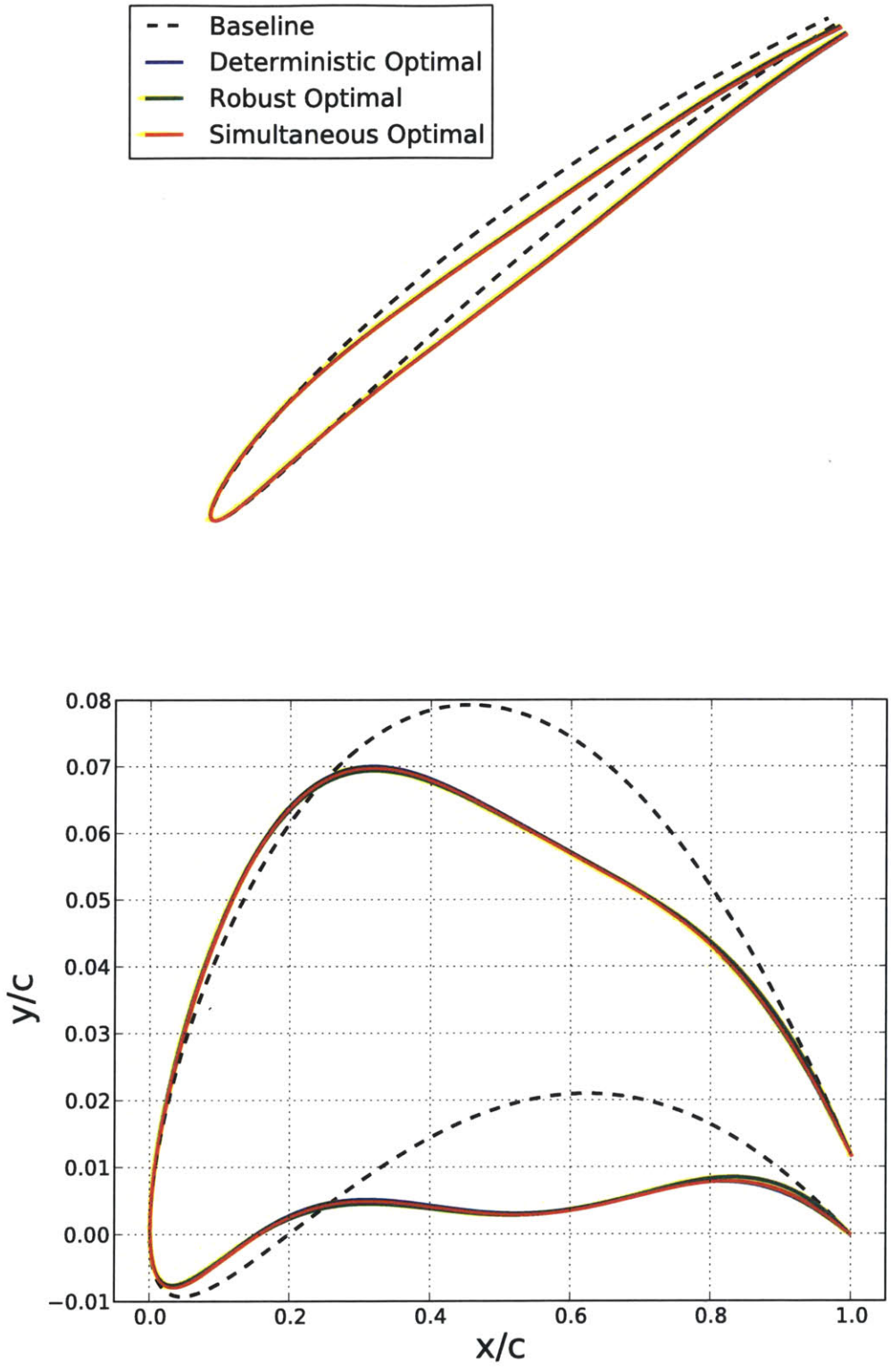

Figure 3-32: Multi-point optimal redesigned SC10 blades.

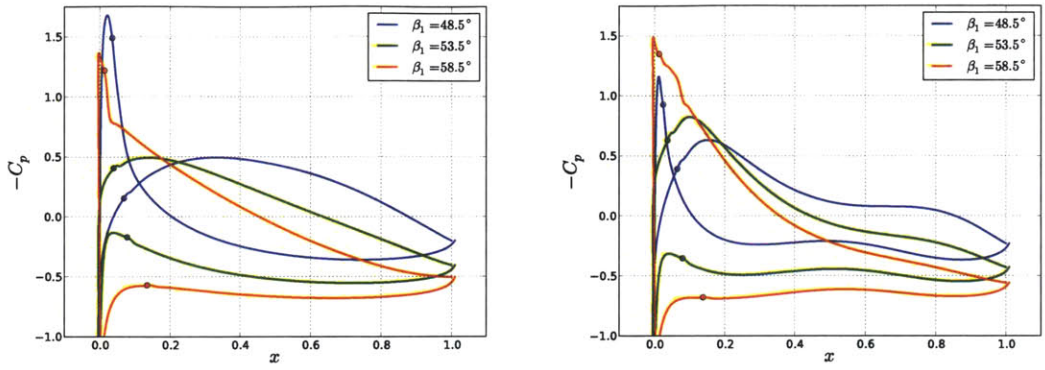

(a) Baseline

(b) Multi-point Deterministic Optimal

Figure 3-33: Comparison between the baseline (left) and multi-point deterministic optimal (right) pressure coefficient profiles for the SC10 blade. The transition locations are indicated by dots.

robust multi-point approaches optimize the performance at negative incidence, where the pressure side losses dominate, and at positive incidence, where the suction side losses dominate. This prevents a switch in the design driver from occurring between deterministic and robust design optimization, so the same optimal design is obtained using either approach.

The sequential and simultaneous optimal tolerances are plotted in Figure 3-37. The maximum error between the optimal tolerances is 4%, which is unsurprising given the similarity of the multi-point optimal geometries. The greatest reduction in variability is specified on the suction side of the blade near the leading edge, which reduces the mean loss at the positive incidence design point by 75%. The optimizer focuses on reducing the mean shift at the positive incidence design point since it is six times larger than the mean shift at the negative incidence design point.

3.5 Chapter Summary

This chapter extended the framework presented in Chapter 2 to perform probabilistic optimization of compressor blade geometry and manufacturing tolerances. This

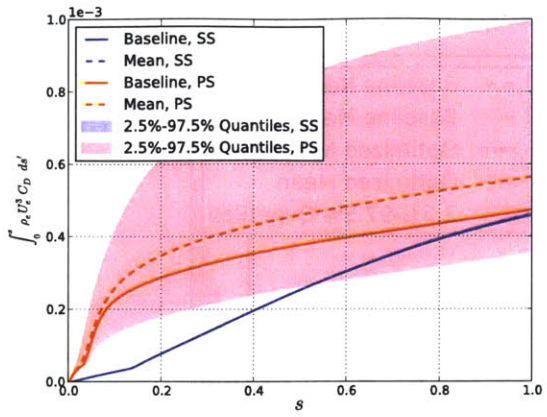

(a) $\beta_1 = 48.5°$, Baseline

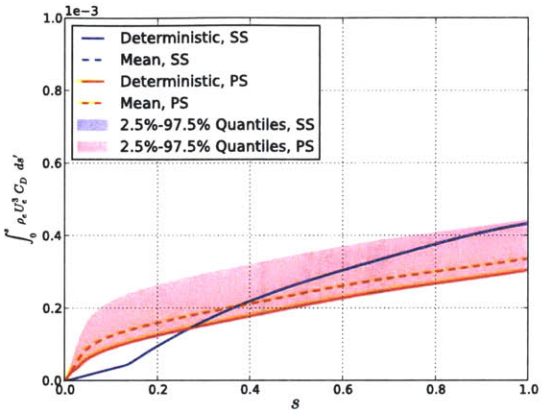

(b) $\beta_1 = 48.5°$, Deterministic Optimal

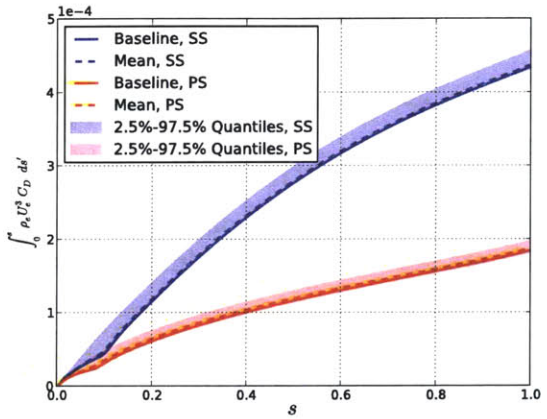

(c) $\beta_1 = 53.5°$, Baseline

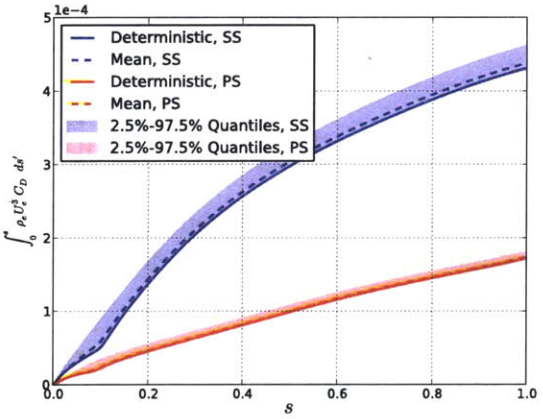

(d) $\beta_1 = 53.5°$, Deterministic Optimal

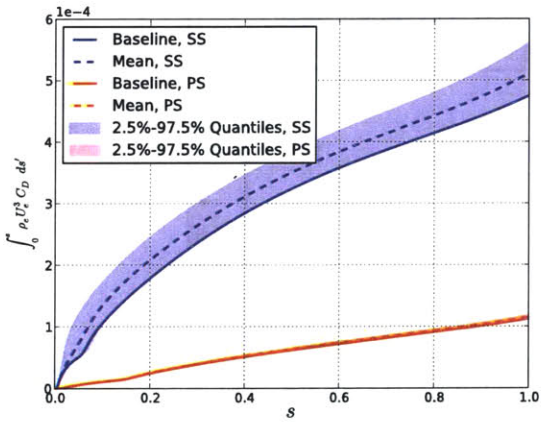

(e) $\beta_1 = 58.5°$, Baseline

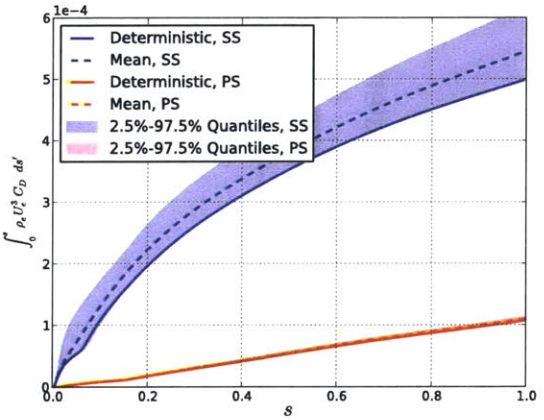

(f) $\beta_1 = 58.5°$, Deterministic Optimal

Figure 3-34: Comparison of the boundary layer entropy generation rate for the baseline and multi-point deterministic optimal SC10 blade. Solid lines indicate the nominal, dashed lines indicate the mean. The pressure side (PS) is plotted in red and the suction side (SS) is plotted in blue.

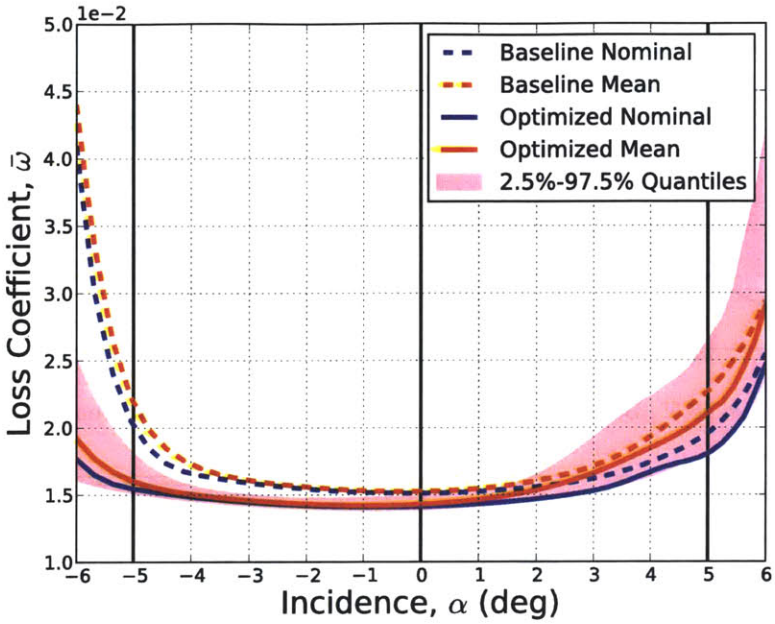

Figure 3-35: Loss coefficient versus incidence angle for the multi-point deterministic optimal redesigned SC10 blade. The quantiles are plotted for the optimized blade.

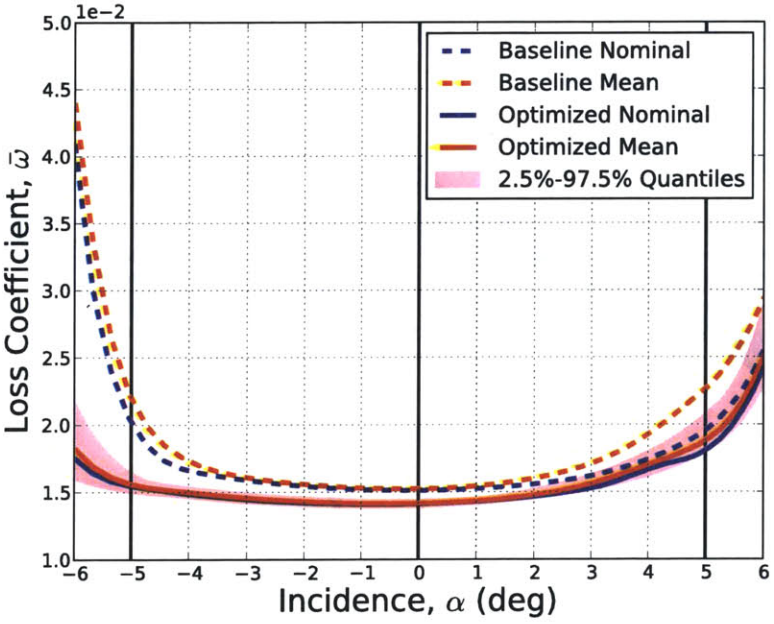

Figure 3-36: Loss coefficient versus incidence angle for the single-point robust optimal redesigned SC10 blade. The quantiles are plotted for the optimized blade.

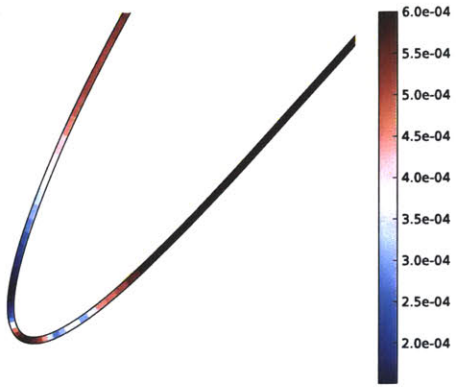

(a) Deterministic Optimal Tolerances

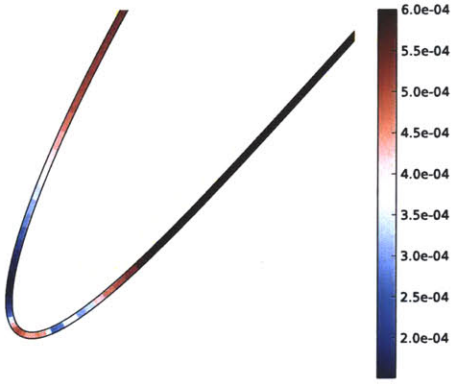

(b) Robust Optimal Tolerances

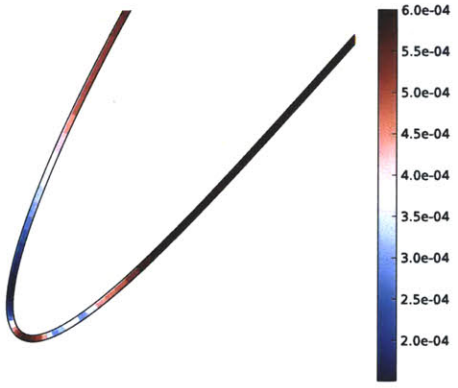

(c) Simultaneous Optimal Tolerances

Figure 3-37: Optimal standard deviation $\sigma(s)/c$ for the multi-point optimized SC10 blades. The lower surface is the pressure side, and the upper surface is the suction side.

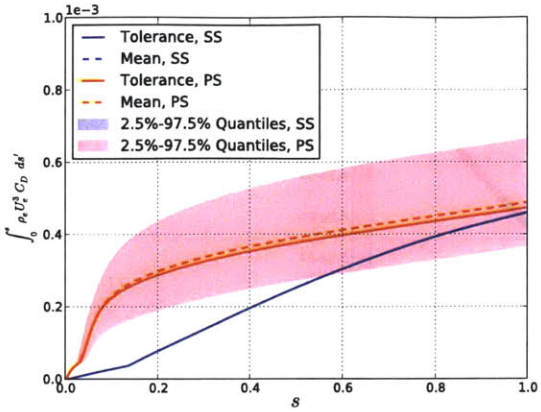

(a) $\beta_1 = 38.7°$, Optimized Tolerances

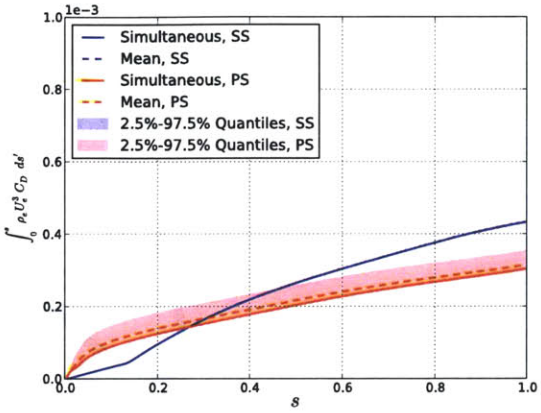

(b) $\beta_1 = 38.7°$, Simultaneous Optimal

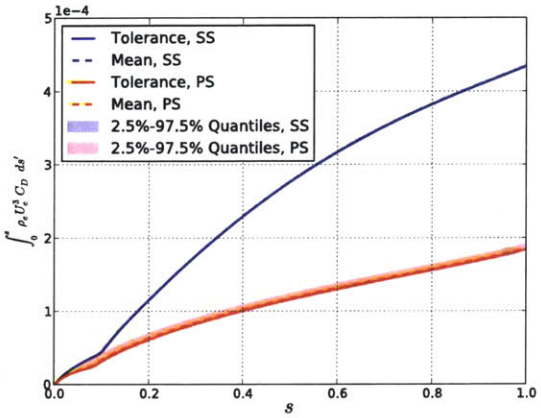

(c) $\beta_1 = 43.2°$, Optimized Tolerances

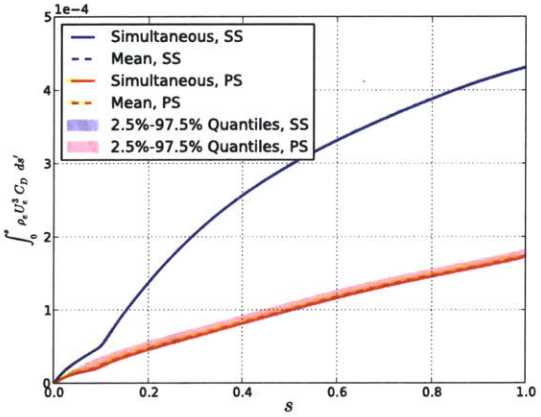

(d) $\beta_1 = 43.2°$, Simultaneous Optimal

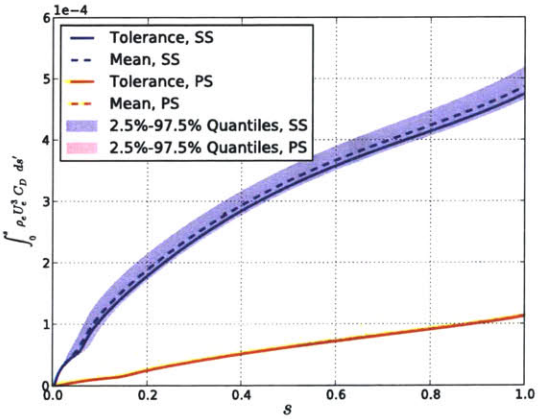

(e) $\beta_1 = 47.7°$, Optimized Tolerances

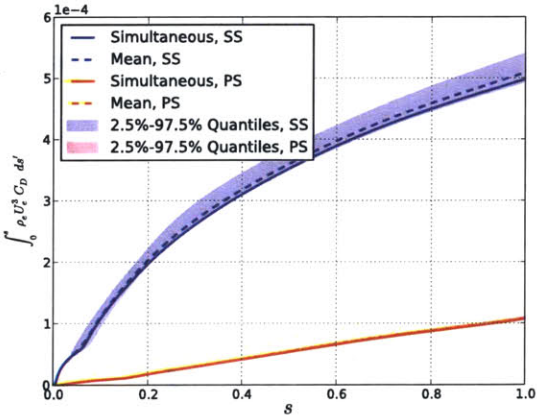

(f) $\beta_1 = 47.7°$, Simultaneous Optimal

Figure 3-38: Comparison of the boundary layer entropy generation rate for the multi-point simultaneous optimal SC10 blade. Solid lines indicate the nominal, dashed lines indicate the mean. The pressure side (PS) is plotted in red and the suction side (SS) is plotted in blue.

framework was used to design blades that were robust to variations in geometry and flow incidence.

For the two geometries considered, the single-point optimal geometry was found to be sensitive to the level of manufacturing variability. This sensitivity was a result of a switch in the dominant loss mechanism that occurred on some manufactured blades, resulting in an asymmetric loss function: perturbing the geometry in a particular direction produced larger loss than perturbing in the opposite direction. For the UTRC exit guide vane, shock induced separation caused by manufacturing variations increased the mean loss of the deterministic optimal design by 7%. For the SC10 rotor blade, deterministic optimization reduced the pressure side loss relative to the baseline design. Introducing manufacturing variations led to flow separation on the suction side of the blade, and robust optimization changed the design to reduce the mean suction side loss. The single-point optimal tolerances were found to depend on the optimal geometry for both cases.

For the fan exit guide vane, multi-point geometry optimization reduced the suction side shock strength by reducing the blade camber and stagger angle, reducing the nominal entropy generation downstream of the shock. For the manufactured blades, this design change decreased both the variability and mean shift in the suction side losses. The optimized rotor blade is flatter than the baseline design over the aft 75% of the blade, which reduced the pressure side entropy generation at negative incidence. Optimizing the nominal geometry reduced the number of manufactured blades with flow separation at negative incidence by 21%, which decreased the variability and mean shift in the loss. Geometry optimization reduced the nominal and mean loss by an average of 10% for the exit guide vane and 11% for the rotor blade. The optimal tolerances for the multi-point optimal geometries followed the "double bow-tie" pattern, resulting in a 13% reduction in the average mean loss for both cases.

Multi-point geometry optimization was found to be effective at reducing loss over a range of incidence angles for an exit guide vane and rotor blade. Deterministic multi-point optimization resulted in blades that were robust to both variations in incidence

and geometry. In these optimizations, the dominant loss mechanism was determined by the flow incidence, blade camber, and blade stagger. Since the multi-point optimal geometries do not depend on the level of geometric variability, a deterministic design approach is recommended, followed by tolerance optimization.

Chapter 4

Summary and Recommendations

This chapter presents a summary of the findings of this thesis, and suggests directions for future work. In Chapter 2, a Gaussian random field model of manufacturing variability was developed that incorporates the non-stationary correlation structure observed in manufactured compressor blades. This model was applied to an exit guide vane and rotor blade with subsonic inlet Mach numbers. At the design incidence angle, manufacturing variations move the average transition location towards the leading edge, increasing the mean turbulent wetted area and increasing the mean loss. Away from the design incidence, manufacturing variations result in the formation of separation bubbles that increase the mean boundary layer mixing losses. These separation bubbles form in regions of strong adverse pressure gradients resulting from shocks and leading edge pressure spikes. For the two geometries considered, flow separation led to an increase in the mean loss of up to 16% relative to the nominal loss. The changes in the mean turning were found to be less than 2% for all incidence angles considered.

Chapter 2 illustrated that tolerance optimization can improve the mean performance by reducing variability in the regions where manufacturing variations have the largest impact on the mean loss. For both geometries considered, a "double bow-tie" tolerance scheme that tightens manufacturing tolerances on either side of the leading edge was found to be optimal. This tolerance scheme reduces the extent of flow separation at positive and negative incidence, and shifts the mean transition location

towards the trailing edge at the design incidence. Reductions in the average mean shift in loss of up to 78% were obtained by reducing the total variability by 2%.

Chapter 3 incorporated geometry optimization to the tolerance optimization framework. Single-point deterministic geometry optimization produced designs that where neither robust to manufacturing variations nor to variations in flow incidence. A switch in the dominant loss mechanism degrades the performance of the single-point deterministic optimal designs when manufacturing variations are introduced. Multi-point deterministic optimization produces optimal blade geometries that are robust with respect to flow incidence and manufacturing variations, provided the design variables modify the geometry on length scales larger than the length scales of the manufacturing variations. Such design variables include those that alter the camber and stagger of the blade. When modifying the geometry at smaller length scales, the design procedures recommended by Goodhand et al. in [33] should be adopted.

Recommendations for Future Work

As discussed in Chapter 2, more work is required to connect the tolerance optimization framework presented in this thesis to blade manufacturing practice. Future work should recommend the appropriate manufacturing processes to use given the optimal process spread $\sigma(s)$, which requires detailed knowledge of the process spread produced by different manufacturing processes. A method for constructing tolerance bands from the optimal process spread would also be of great use to blade manufacturers. The differences in the mean performance due to truncating the distribution of manufacturing variations versus scaling the distribution of manufacturing variations, as was done in this thesis, should be quantified as part of this work.

The multi-point robust optimal compressor blades are robust to geometric variability introduced by the manufacturing process and to incidence variations. Future work should investigate the impact of variability in the inflow Mach number on the robust optimal design. Variability in the inflow Mach number can be incorporated to

the design framework using Monte Carlo to sample from a distribution of Mach numbers as was done to incorporate variations in the geometry, or using quadrature as was done to incorporate variations in the flow incidence. Results presented in Chapter 3 for the single-point optimized exit guide vane showed that the formation of shocks can cause a switch in the dominant loss mechanism of manufactured blades, and the same switch could be triggered by variations in the inflow Mach number. Future work should address this possibility and recommend design practices in such cases.

A natural extension of the work presented in this thesis is to consider optimizing the geometry and tolerances of 3D blades subject to manufacturing variability. This would require modeling the correlation between manufacturing variations in the spanwise direction of compressor blades, which has been studied to some extent in [27] and [47]. Geometric variations in the hub and shroud profiles, as well as in rotor tip clearance could also be included.

In this thesis, the blading was assumed to be axisymmetric with identical manufacturing variations applied to each blade. Recently, Lange et al. examined the effects of geometric variability on non-axisymmetric blading by simulating eight rotor blade geometries in tandem [50]. They found that assuming axisymmetric blading overpredicts the mean shift in the loss coefficient. Incorporating the effects of non-axisymmetric blading by simulating multiple blade passages in tandem would improve the accuracy of estimates of the performance impact of manufacturing variability, and would elucidate the interaction effects between manufacturing variations on neighboring blades.

Future work on geometry and tolerance optimization should incorporate the adjoint method to reduce the computational cost of computing shape sensitivities. The adjoint method, which computes sensitivities by solving a set of adjoint equations derived from the linearized governing equations, has been applied to optimize wings [22, 40, 65] and turbomachinery blades [10, 21, 56]. The computational cost of computing sensitivities with the adjoint method grows with the number of objectives and constraints, but is independent of the number of design variables. The adjoint method would therefore be beneficial in performing simultaneous design and tolerance optimization, especially in

3D, where the number of design variables is more than an order of magnitude greater than the number of objectives and constraints.

Finally, it would be useful to obtain data relating gas turbine component manufacturing costs to dimensional tolerances. If reducing tolerances in particular regions of a compressor blade incurs higher manufacturing costs than others, this information could be used to guide the tolerance specification by optimizing some combination of the manufacturing cost and blade performance statistics. The key challenge would be the development of accurate manufacturing cost models. The quality loss model introduced in Chapter 1 would be useful in developing an objective function that balances the competing objectives of improving performance and reducing production costs.

Appendix A

The Karhunen-Loève Expansion

The Karhunen-Loève expansion represents the random field $e(s, \theta)$ in terms of its mean $\bar{e}(s)$ and a basis constructed from its covariance function $C(s_1, s_2)$. The random field is assumed to be continuous in the mean square sense:

$$\lim_{s_1 \to s_2} \mathbb{E}[(e(s_1, \theta) - e(s_2, \theta))^2] = 0 \quad \forall s_2 \in S.$$

Then, the covariance function C is continuous and

$$\int_S \int_S C(s_1, s_2)\, ds_1\, ds_2 < \infty.$$

We can therefore define the covariance kernel K as

$$\langle Kv, w \rangle = \int_S \int_S C(s_1, s_2) v(s) w(s)\, ds_1\, ds_2,$$

which is a symmetric semi-positive definite operator equipped with inner product $\langle \cdot, \cdot \rangle$, and v, $w \in L_2(S)$. By Mercer's theorem [52], it follows that C has the spectral decomposition

$$C(s_1, s_2) = \sum_{i \geq 1} \lambda_i \phi_i(s_1) \phi_i(s_2),$$

where each pair of eigenvalues λ_i and eigenfunctions $\phi_i(s)$ are computed from the following Fredholm equation:

$$\int_S C(s_1, s_2)\phi_i(s_2)ds_2 = \lambda_i\phi_i(s_1). \tag{A.1}$$

Moreover, the eigenfunctions are chosen orthonormal such that $\langle\phi_i, \phi_j\rangle = \delta_{ij}$, and the eigenvalues are real, non-negative, and satisfy

$$\sum_{i\geq 1}\lambda_i^2 < \infty.$$

By the Karhunen-Loève theorem [52], the decomposition of the random field is given by:

$$e(s,\theta) = \bar{e}(s) + \sum_{i\geq 1}\sqrt{\lambda_i}\phi_i(s)\xi_i(\theta),$$

where the eigenvalues are arranged in descending order such that $\lambda_1 \geq \lambda_2 \geq \ldots \to 0$. The distribution of the random variables $\xi_i(\theta)$ are determined by taking the inner product of the random field with each of the eigenfunctions:

$$\xi_i(\theta) = \frac{1}{\sqrt{\lambda_i}}\langle e(s,\theta) - \bar{e}(s), \phi_i(s)\rangle.$$

The random variables $\xi_i(\theta)$ are mutually uncorrelated with zero mean and unit variance:

$$\mathbb{E}[\xi_i] = \mathbb{E}\left[\frac{1}{\sqrt{\lambda_i}}\langle e - \bar{e}, \phi_i(s)\rangle\right] = \frac{1}{\sqrt{\lambda_i}}\langle\mathbb{E}[e - \bar{e}], \phi_i(s)\rangle = 0,$$

$$
\begin{aligned}
\mathbb{E}[\xi_i \xi_j] &= \mathbb{E}\left[\frac{1}{\sqrt{\lambda_i \lambda_j}} \int_S \int_S (e(s_1,\theta) - \bar{e}(s_1))(e(s_2,\theta) - \bar{e}(s_2))\phi_i(s_1)\phi_j(s_2)\, ds_1 ds_2\right] \\
&= \frac{1}{\sqrt{\lambda_i \lambda_j}} \int_S \int_S \mathbb{E}\left[(e(s_1,\theta) - \bar{e}(s_1))(e(s_2,\theta) - \bar{e}(s_2))\right] \phi_i(s_1)\phi_j(s_2)\, ds_1 ds_2 \\
&= \frac{1}{\sqrt{\lambda_i \lambda_j}} \int_S \left[\int_S C(s_1,s_2)\phi_i(s_1)\, ds_1\right] \phi_j(s_2)\, ds_2 \\
&= \frac{\lambda_i}{\sqrt{\lambda_i \lambda_j}} \langle \phi_i, \phi_j \rangle \\
&= \delta_{ij}.
\end{aligned}
$$

For a Gaussian random field, the $\xi_i(\theta)$ are independent, identically distributed (i.i.d.) standard normal random variables [52].

To construct the K-L expansion numerically, the domain S is first discretized. For example, if $\dim S = 1$ and $S = [s_{min}, s_{max}]$, N_s nodes are chosen on the interval so that $s_1 = s_{min} < s_2 < ... < s_{N_s} = s_{max}$. The Nyström method is then used to solve (A.1) and determine both the eigenvalues and the value of the eigenvectors evaluated at the nodes $\{s_i\}_{1 \le i \le N_s}$ [58].

Appendix B

Interchanging Expectation and Differentiation

The pathwise sensitivity method interchanges differentiation and integration so that the gradient of the mean objective function $\mathbb{E}[F(\mathbf{p}, \boldsymbol{\xi}(\theta))]$ with respect to the parameter $\mathbf{p}$ is computed as the mean of the gradient of F:

$$\frac{\partial \mathbb{E}[F(\mathbf{p}, \boldsymbol{\xi}(\theta))]}{\partial \mathbf{p}} = \mathbb{E}\left[\frac{\partial F(\mathbf{p}, \boldsymbol{\xi}(\theta))}{\partial \mathbf{p}}\right].$$

The objective function F is a functional of the random field $e(s, \theta; \mathbf{p})$. We now provide conditions on the objective function and parameters that ensure that this interchange is justified. The first requirement is that the random vector $\boldsymbol{\xi}$ must be independent of the parameters $\mathbf{p}$. We assume that the parameters $\mathbf{p}$ only affect the eigenvalues and eigenvectors in the K-L expansion of $e(s, \theta; \mathbf{p})$, and do not affect the random vector $\boldsymbol{\xi}$.

The second requirement is on the regularity of the function $F(\theta, \mathbf{p})$. For simplicity, we only consider one parameter p. Interchanging differentiation and integration requires that the following interchange of limit and integration is justified:

$$\mathbb{E}\left[\lim_{h \to 0} \frac{F(\theta, p+h) - F(\theta, p)}{h}\right] = \lim_{h \to 0} \mathbb{E}\left[\frac{F(\theta, p+h) - F(\theta, p)}{h}\right]. \qquad \text{(B.1)}$$

A necessary and sufficient condition for this interchange to be valid is that the difference quotients $Q_h = h^{-1}[F(\theta, p+h) - F(\theta, p)]$ are uniformly integrable, i.e. that

$$\lim_{c\to\infty} \sup_h \mathbb{E}[|Q_h| 1\{|Q_h| > c\}] = 0,$$

where $1\{|Q_h| > c\}$ is the indicator function [31]. This condition is not readily verified for practical problems, since the analytical distribution of F is typically unknown. We instead provide a set of sufficient conditions that are more straightforward to verify in practice, following reference [31]. Denote the set of points in Θ where F is differentiable with respect to e by $D_F \subset \mathbb{R}^{|\Theta|}$. The following are sufficient conditions for the interchange of the limit and expectation in (B.1).

(B1) For every $p \in \mathcal{P}$ and $s \in S$, $\partial e(s, \theta; p)/\partial p$ exists with probability 1.

(B2) For every $p \in \mathcal{P}$, $\mathbb{P}[e(s, \theta; p) \in D_F] = 1$.

(B3) F is Lipschitz continuous, i.e. there exists a constant $k_F < \infty$ such that for all $u(s)$, $v(s)$,

$$|F(u) - F(v)| \leq k_F \|u - v\|.$$

(B4) For every $s \in S$, there exists a random variable k_e such that for all p_1, $p_2 \in \mathcal{P}$,

$$|e(s, \theta; p_2) - e(s, \theta; p_1)| \leq k_e |p_2 - p_1|,$$

and $\mathbb{E}[k_e] < \infty$.

Conditions (B3) and (B4) imply that F is Lipschitz continuous in p with probability one. Taking $\kappa_F = k_F \sup_s k_e$,

$$|F(\theta, p_2) - F(\theta, p_1)| \leq \kappa_F |p_2 - p_1|.$$

We can then bound the difference quotient:

$$\left|\frac{F(\theta, p+h) - F(\theta, p)}{h}\right| \leq \kappa_F,$$

and apply the dominated convergence theorem to interchange the expectation and limit in (B.1).

Conditions (B3) and (B4) together determine if F is almost surely Lipschitz continuous, and thus determine what type of input parameters and output quantities of interest can be treated with the pathwise sensitivity method. Output functionals that may change discontinuously when smooth perturbations are made to the random field are not Lipschitz continuous almost surely. Thus, condition (B3) excludes failure probabilities, e.g. $\mathbb{P}(F \geq c) = \mathbb{E}[\mathbf{1}\{F \geq c\}]$, since the indicator function $\mathbf{1}\{F \geq c\}$ is discontinuous when $F = c$. This difficulty can be remedied to some degree by using a smoothed version of the indicator function, but this introduces additional error to the sensitivity [25]. Conditions (B2) and (B3) do permit functions that fail to be differentiable at certain points, as long as the points at which differentiability fails occur with probability zero, and F is continuous at these points. In this case, the expectation operator smooths the function F, so that $\mathbb{E}[F]$ is differentiable.

Optimizing the nominal geometry and tolerances is equivalent to optimizing the mean and covariance of the manufacturing error $e(s, \theta)$, in which case $\mathbf{p} = \{\mathbf{d}, \boldsymbol{\sigma}\}$. Applying the pathwise sensitivity method requires that the output quantities of interest, e.g. the loss coefficient and flow turning, are continuous with respect to geometric perturbations. Even in the presence of shocks, these quantities are continuous (although possibly not everywhere differentiable) functions of the blade geometry, since they are computed from integrals of functions of the flow states downstream of the blade.

Bibliography

[1] P. Abrahamsen. A review of Gaussian random fields and correlation functions. Technical Report TR-917, Norwegian Computing Center, Oslo, Norway, 1997.

[2] R.J. Adler and J.E. Taylor. *Random Fields and Geometry*, chapter 1, pages 5–42. Springer, New York, 1st edition, 2007.

[3] B.B. Beachkofski and R.V. Grandhi. Probabilistic system reliability for a turbine engine airfoil. In *Proceedings of ASME Turbo Expo 2004*, 2004.

[4] D. Bestle and P. Flassig. Optimal aerodynamic compressor blade design considering manufacturing noise. In *Proceedings of the 8th ASMO UK/ISSMO Conference*, 2010.

[5] H.G. Beyer and B. Sendhoff. Robust optimization - a comprehensive survey. *Computational Methods in Applied Mechanics and Engineering*, 196:3190–3218, 2007.

[6] H.G. Bock, W. Egartner, W. Kappis, and V. Schulz. Practical shape optimization for turbine and compressor blades by the use of PRSQP methods. *Optimization and Engineering*, 3:395–414, 2002.

[7] A. Borzí, V. Schulz, C. Schillings, and G. von Winckel. On the treatment of distributed uncertainties in PDE-constrained optimization. *GAMMMitteilungen*, 33(2):230–246, 2010.

[8] C.G. Broyden. The convergence of a class of double-rank minimization algorithms. *IMA Journal of Applied Mathematics*, 6(1):76–90, 1970.

[9] T.R. Camp and H.W. Shin. Turbulence intensity and length scale measurements in multistage compressors. *Journal of Turbomachinery*, 117:38–46, 1995.

[10] M.S. Campobasso, M.C. Duta, and M.B. Giles. Adjoint calculation of sensitivities of turbomachinery objective functions. *Journal of Propulsion and Power*, 19(4):693–703, 2003.

[11] L.K. Chan and P.H. Xiao. Combined robust design. *Quality Engineering*, 8(1):47–56, 1995.

[12] H. Chen, Q. Wang, R. Hu, and P. Constantine. Conditional sampling and experiment design for quantifying manufacturing error of transonic airfoil. In *Proceedings of the 49th Aerospace Sciences Meeting*, 2011.

[13] N. Cumpsty. *Compressor Aerodynamics.* Longman Scientific and Technical, 1989.

[14] J.T. DeMasi-Marcin and D.K. Gupta. Protective coatings in the gas turbine engine. *Surface and Coatings Technology*, 68:1–9, 1994.

[15] J.D. Denton. Loss mechanisms in turbomachines. *Journal of Turbomachinery*, 115:621–656, 1993.

[16] M. Dodson and G.T. Parks. Robust aerodynamic design optimization using polynomial chaos. *Journal of Aircraft*, 46(2):635–646, 2009.

[17] M. Drela. *Frontiers of Computational Fluid Dynamics 1998*, chapter 19, Pros and cons of airfoil optimization, pages 363–380. World Scientific Publishing, 1998.

[18] M. Drela and M.B. Giles. Viscous-inviscid analysis of transonic and low Reynolds number airfoils. *AIAA Journal*, 25(10):1347–1355, 1986.

[19] M. Drela and H.H. Youngren. *A User's Guide to MISES 2.63.* MIT Aerospace Computational Design Laboratory, 70 Vassar St, Cambridge MA 02139, February 2008.

[20] J.D. Duffner. *The Effects of Manufacturing Variability on Turbine Vane Performance.* Master's dissertation, Massachusetts Institute of Technology, Department of Aeronautics and Astronautics, 2008.

[21] M.C. Duta, S. Shahpar, and M.B. Giles. Turbomachinery design optimization using automatic differentiated adjoint code. In *Proceedings of Turbo Expo 2007*, 2007.

[22] J. Elliot and J. Peraire. Practical 3D aerodynamic design and optimization using unstructured meshes. *AIAA Journal*, 35(9):1479–1485, 1997.

[23] G.A. Fenton and E.H. Vanmarcke. Simulation of random fields via local average subdivision. *Journal of Engineering Mechanics*, 116(8):1733–1749, 1990.

[24] A.V. Fiacco. Sensitivity analysis for nonlinear programming. *Mathematical Programming*, 10:287–311, 1976.

[25] J.P. Foque, G. Papanicolaou, and R. Sircar. Singular perturbations in option pricing. *SIAM Journal of Applied Mathematics*, 63(5):1648–1665, 2003.

[26] T.H. Fransson and J.M. Verdon. Standard configurations for unsteady flow through vibrating axial-flow turbomachine cascades. In *Unsteady Aerodynamics, Aeroacoustics and Aeroelasticity of Turbomachines and Propellers*, pages 859–889, New York, 1993. Springer-Verlag.

[27] V. E. Garzon. *Probabilistic Aerothermal Design of Compressor Airfoils.* PhD dissertation, Massachusetts Institute of Technology, Department of Aeronautics and Astronautics, 2003.

[28] V. E. Garzon and D. Darmofal. Impact of geometric variability on axial compressor performance. *Journal of Turbomachinery*, 125(4):692–703, 2003.

[29] V.E. Garzon and D.L. Darmofal. On the aerodynamic design of compressor airfoils for robustness under geometric uncertainty. In *Proceedings of ASME Turbo Expo 2004*, 2004.

[30] T. Ghisu, J.P. Jarrett, and G.T. Parks. Robust design optimization of airfoils with respect to ice accretion. *Journal of Aircraft*, 48(1):287–304, 2011.

[31] P. Glasserman. *Monte Carlo Methods in Financial Engineering*, chapter 7, Estimating Sensitivities, pages 386–401. Springer Verlag, New York, 2004.

[32] M.N. Goodhand, R.J. Miller, and H.W. Lung. The sensitivity of 2D compressor incidence range of in-service geometric variation. In *Proceedings of ASME Turbo Expo 2012*, 2012.

[33] M.N. Goodhand, R.J. Miller, and H.W. Lung. The impact of geometric variation on compressor 2d incidence range. *Journal of Turbomachinery*, 2014.

[34] C.R. Gumbert and P.A. Newman. High-fidelity computational optimization for 3-D flexible wings: Part II-effect of random geometric uncertainty on design. *Optimization and Engineering*, 6:139–156, 2005.

[35] J. Häcker. *Statistical Analysis of Manufacturing Deviations and Classification Methods for Probabilistic Aerothermal Design of Turbine Blades.* Diplomarbeit, University of Stuttgart, Institute of Flight Mechanics and Flight Control, 2000.

[36] K. Heinze, W.H. Friedl, K. Vogeler, and M. Voigt. Probabilistic HCF-investigation of compressor blades. In *Proceedings of ASME Turbo Expo 2009*, 2009.

[37] Y.S. Hong and T.C. Chang. A comprehensive review of tolerancing research. *International Journal of Production Research*, 40(11):2425–2459, 2010.

[38] M.F. Huang, Y.R. Zhong, and Z.G. Xu. Concurrent process tolerance design based on minimum product manufacturing cost and quality loss. *International Journal of Manufacturing Technology*, 25:714–722, 2005.

[39] L. Huyse, S.L. Padula, R.M. Lewis, and W. Li. Probabilistic approach to free-form airfoil shape optimization under uncertainty. *AIAA Journal*, 40(9):1764–1772, 2002.

[40] A. Jameson. Aerodynamic design via control theory. *Journal of Scientific Computing*, 3(3):233–260, 1988.

[41] A. Javed, R. Pecnik, M. Olivero, and J.P. van Buijtenen. Effects of manufacturing noise on microturbine centrifugal impeller performance. In *Proceedings of ASME Turbo Expo 2012*, 2012.

[42] S.G. Johnson. The NLopt nonlinear-optimization package, August 2013, URL: `http://ab-initio.mit.edu/nlopt`.

[43] I. T. Jolliffe. *Principal Component Analysis.* Springer-Verlag, New York, 1986.

[44] V.E. Kane. Probabilistic optimal design in the presence of random fields. *Journal of Quality Technology*, 18:41–52, 1986.

[45] U Köller, R. Möning, B. Küsters, and H.A. Schreiber. Development of advanced compressor airfoils for heavy-duty gas turbines - part I: Design and optimization. *Journal of Turbomachinery*, 122:397–405, 2000.

[46] A. Kumar, P.B. Nair, A.J. Keane, and S. Shahpar. Probabilistic performance analysis of eroded compressor blades. In *Proceedings of PWR2005*, 2005.

[47] C.M. Lamb. *Probabilistic Performance-Based Geometric Tolerancing of Compressor Blades.* Master's dissertation, Massachusetts Institute of Technology, Department of Aeronautics and Astronautics, 2005.

[48] A. Lange, M. Voigt, K. Vogeler, and E. Johann. Principal component analysis of 3D scanned compressor blades for probabilistic CFD simulation. In *Proceedings of the 53rd AIAA/ASME/ASCE/AHS/ASC Structures, Structural Dynamics and Materials Conference*, 2012.

[49] A. Lange, M. Voigt, K. Vogeler, H. Schrapp, E. Johann, and V. Gümmer. Probabilistic CFD simulation of a high-pressure compressor stage taking manufacturing variability into account. In *Proceedings of ASME Turbo Expo 2010*, 2010.

[50] A. Lange, M. Voigt, K. Vogeler, H. Schrapp, E. Johann, and V. Gümmer. Impact of manufacturing variability and non-axisymmetry on high-pressure compressor stage performance. In *Proceedings of ASME Turbo Expo 2011*, 2011.

[51] J. Lavainne. *Sensitivity of a Compressor Repeating-Stage to Geometry Variation.* Master's dissertation, Massachusetts Institute of Technology, Department of Aeronautics and Astronautics, 2003.

[52] O.P. Le Mâitre and O.M. Knio. *Spectral Methods for Uncertainty Quantification - With Applications to Computational Fluid Dynamics*, chapter 2, pages 17–44. Springer Verlag, New York, 1st edition, 2010.

[53] C.L. Lee and G.R. Tang. Tolerance design for products with correlated characteristics. *Mechanism and Machine Theory*, 35:1675–1687, 2000.

[54] M. Loève. Probability theory. *Graduate Texts in Mathematics*, 45, 1963.

[55] G.J.A. Loeven and H. Bijl. Airfoil analysis with uncertain geometry using the probabilistic collocation method. In *Proceedings of the 49th AIAA/ASME/ASCE/AHS/ASC Structures, Structural Dynamics and Materials Conference*, 2008.

[56] A.C. Marta, S. Shankaran, and A. Stein. Blade shape optimization using a rans discrete adjoint solver. In *2nd International Conference on Engineering Optimization*, 2010.

[57] S. Missoum. Probabilistic optimal design in the presence of random fields. *Structural Multidisciplinary Optimization*, 35:523–530, 2008.

[58] E.J. Nyström. On the practical solution of integral equations with applications to boundary value problems. *Acta Mathematica*, 54:185–204, 1930.

[59] M. Padulo, M.S. Campobasso, and M.D. Guenov. Novel uncertainty propagation method for robust aerodynamic design. *AIAA Journal*, 49(3):530–543, 2011.

[60] E. Parzen. On estimation of a probability density function and mode. *The Annals of Mathematical Statistics*, 33(3):1065–1076, 1962.

[61] P.J. Petrie-Repar, A. McGhee, and P.A. Jacobs. Three-dimensional viscous flutter analysis of standard configuration 10. In *Proceedings of ASME Turbo Expo 2007*, 2007.

[62] L. Piegl and W. Tiller. *The NURBS Book*, chapter 2. Springer-Verlag, Berlin, 2nd edition, 1997.

[63] M.J.D. Powell. A fast algorithm for nonlinearly constrained optimization calculations. *Lecture Notes in Mathematics*, 630:144–157, 1978.

[64] L. Reid and D.C. Urasek. Experimental evaluation of the effects of a blunt leading edge on the performance of a transonic rotor. *ASME Journal of Engineering for Power*, pages 199–204, 1973.

[65] J. Reuther, A. Jameson, J.J. Alonso, M.J. Rimlinger, and D. Sauders. Constrained multipoint aerodynamic shape optimization using an adjoint formulation and parallel computers. In *35th AIAA Aerospace Sciences Meeting*, 1997.

[66] C.P. Robert and G. Casella. *Monte Carlo Statistical Methods*, chapter 4. Springer-Verlag, New York, 2004.

[67] R.Y. Rubinstein and A. Shapiro. *Discrete event systems: Sensitivity analysis and stochastic optimization by the score function method*, volume 346. Wiley, New York, 1993.

[68] C. Schillings, S. Schmidt, and V. Schulz. Efficient shape optimization for certain and uncertain aerodynamic design. *Computers and Fluids*, 46:78–87, 2011.

[69] M. Shinozuka and G. Deodatis. Simulation of multi-dimensional gaussian stochastic fields by spectral representation. *Applied Mechanics Reviews*, 49(1):29–53, 1996.

[70] A. Sinha, B. Hall, B. Cassenti, and G. Hilbert. Vibratory parameters of blades from coordinate measurement machine data. *Journal of Turbomachinery*, 130, 2008.

[71] H. E. Stephens and D. E. Hobbs. Design and performance evaluation of supercritical airfoils for axial flow compressors. Technical Report PWA-FR-11455, Pratt and Whitney Government Products Division, 1979.

[72] K.L. Suder, R.V. Chima, A.J. Strazisar, and W.B. Roberts. The effect of adding roughness and thickness to a transonic axial compressor rotor. *ASME Journal of Turbomachinery*, 117:491–505, 1995.

[73] G. Taguchi, E. A. Elsayed, and T.C. Hsiang. *Quality Engieering in Production Systems.* McGraw-Hill College, 1989.

[74] N. Thakur, A. Keane, and P.B. Nair. Capture of manufacturing uncertainty in turbine blades through probabilistic techniques. In *7th ASMO-UK/ISSMO International Conference on Engineering Design Optimization*, 2008.

[75] X. Wang, C. Hirsch, Z. Liu, S. Kang, and C. Lacor. Uncertainty-based robust aerodynamic optimization of rotor blades. *International Journal for Numerical Methods in Engineering*, 94:111–127, 2012.

[76] C.C. Wu and G.R. Tang. Tolerance design for products with asymmetric quality losses. *International Journal of Production Research*, 36(9):2529–2541, 1998.

[77] C.Y. Wu. Arbitrary surface flank milling of fan, compressor, and impeller blades. *Journal of Engineering for Gas Turbines and Power*, 117:534–539, 1995.

[78] B.D. Youn and Xi Zhimin. An effective random field characterization for probability analysis and design. In *Proceedings of the 49th AIAA/ASME/ASCE/AHS/ASC Structures, Structural Dynamics and Materials Conference*, 2008.

[79] H.H. Youngren. *Analysis and design of transonic cascades with splitter vanes.* Master's dissertation, Massachusetts Institute of Technology, Department of Aeronautics and Astronautics, 1991.